

# **A Numerical and Experimental Investigation of Planar Inverted-F Antennas for Wireless Communication Applications**

Minh-Chau T. Huynh

Thesis submitted to the Faculty of the  
Virginia Polytechnic Institute and State University  
In partial fulfillment of the requirements for the degree of

Master of Science  
In  
Electrical Engineering

Dr. W.L. Stutzman, Chair

Dr. W.A. Davis

Dr. D.G. Sweeney

October 19, 2000  
Blacksburg, Virginia

**Key Words:** Antennas, Small Antennas, Planar Inverted-F, Microstrip, Wideband Antennas, Low-Profile.

Copyright 2000, Minh-Chau T. Huynh

# **A Numerical and Experimental Investigation of Planar Inverted-F Antennas for Wireless Communication Applications**

**Minh-Chau T. Huynh**

## **(Abstract)**

In recent years, the demand for compact handheld communication devices has grown significantly. Devices having internal antennas have appeared to fill this need. Antenna size is a major factor that limits device miniaturization. In the past few years, new designs based on the microstrip antennas (MSA) and planar inverted-F antennas have been used for handheld wireless devices because these antennas have low-profile geometry and can be embedded into the devices.

New wireless applications requiring operation in more than one frequency band are emerging. Dual-band and tri-band phones have gained popularity because of the multiple frequency bands used for wireless applications. One prominent application is to include bluetooth, operating band at 2.4 GHz, for short-range wireless use.

This thesis examines two antennas that are potential candidates for small and low-profile structures: microstrip antennas and planar inverted-F antennas. Two techniques for widening the antenna impedance bandwidth are examined by adding parasitic elements. Reducing antenna size generally degrades antenna performance. It is therefore important to also examine the fundamental limits and parameter tradeoffs involved in size reduction. In the handheld environment, antennas are mounted on a small ground plane. Ground plane size effects on antennas are investigated and the results from a thorough numerical study on the performance of a PIFA with various ground planes sizes and shapes is reported. Finally, a new wideband compact PIFA antenna (WC-PIFA) is proposed. Preliminary work is presented along with numerical and experimental results

for various environments such as free space, plastic casing, and the proximity of a hand. This new antenna covers frequencies from 1700 MHz to 2500 MHz, which basically include the following operating bands: DCS-1800m PCS-1900, IMT-2000, ISM, and Bluetooth.

## **Acknowledgements**

I would like to thank Dr. Warren Stutzman, my advisor, for encouragement, patience, generous amounts of time and effort, valuable discussion, countless edits, and the chance to be part of the Virginia Tech Antenna Group. I would also like to thank the members of my committee, Dr. William Davis, and Dr. Dennis Sweeney.

I am indebted to Dr. William Davis for discussions and suggestions on the analysis of the wideband compact PIFA. I am also grateful to Kochiro Takamizawa for sharing his depth in antenna knowledge and his priceless assistance on measuring the antennas.

# Table of Contents

<b>ABSTRACT .....</b>	<b>II</b>
<b>ACKNOWLEDGEMENTS.....</b>	<b>IV</b>
<b>TABLE OF CONTENTS.....</b>	<b>V</b>
<b>CHAPTER 1: INTRODUCTION .....</b>	<b>1</b>
1.1. OVERVIEW .....	1
1.2. ORGANIZATION OF THE THESIS .....	3
1.3. REFERENCES .....	4
<b>CHAPTER 2: OVERVIEW OF LOW-PROFILE ANTENNAS.....</b>	<b>5</b>
2.1. INTRODUCTION.....	5
2.2. THE MICROSTRIP ANTENNA .....	5
2.2.1. <i>Introduction</i> .....	5
2.2.2. <i>Transmission Line Model for Microstrip Antennas</i> .....	7
2.2.3. <i>Cavity Model for Microstrip Antennas</i> .....	12
2.2.4. <i>Design Procedure</i> .....	16
2.2.5. <i>Summary</i> .....	24
2.3. THE PLANAR INVERTED-F ANTENNA.....	25
2.3.1. <i>Introduction</i> .....	25
2.3.2. <i>Analysis Model</i> .....	26
2.3.3. <i>Field and Current Distribution</i> .....	29
2.3.4. <i>Resonant Frequency</i> .....	32
2.3.5. <i>Bandwidth</i> .....	36
2.3.6. <i>Design Procedure</i> .....	37
2.3.7. <i>Summary</i> .....	39
2.4. REFERENCES .....	39
<b>CHAPTER 3: TECHNIQUES FOR WIDENING THE BANDWIDTH OF MICROSTRIP ANTENNAS.....</b>	<b>41</b>
3.1. INTRODUCTION.....	41
3.2. NUMERICAL ANALYSIS .....	42
3.3. CONFIGURATIONS .....	46
3.3.1. <i>Edge-Coupling Structure Antennas</i> .....	46

3.3.2.	<i>Capacitively-Fed Structure Antennas</i> .....	48
3.4.	SUMMARY .....	55
3.5.	REFERENCES .....	55
<b>CHAPTER 4: FUNDAMENTAL LIMITS ON THE RADIATION <math>Q</math> OF SMALL ANTENNAS</b> .....		<b>57</b>
4.1.	INTRODUCTION.....	57
4.2.	OVERVIEW OF THEORETICAL INVESTIGATIONS ON THE FUNDAMENTAL LIMITS.	57
4.3.	COMPARISON OF SMALL ANTENNAS .....	62
4.4.	SUMMARY .....	64
4.5.	REFERENCES .....	65
<b>CHAPTER 5: GROUND PLANE EFFECTS ON THE PERFORMANCE OF THE PIFA</b> .....		<b>67</b>
5.1.	INTRODUCTION.....	67
5.2.	THEORETICAL MODELS .....	68
5.3.	FINITE GROUND PLANE SIZE EFFECTS ON THE CONVENTIONAL PIFA .....	72
5.3.1.	<i>Setup Description</i> .....	72
5.3.2.	<i>Numerical and Experimental Results</i> .....	73
5.3.3.	<i>Other Configurations</i> .....	84
5.4.	EFFECTS OF POSITION AND ORIENTATION OF A PIFA ON A FINITE GROUND PLANE	88
5.4.1.	<i>PIFA Geometries</i> .....	89
5.4.2.	<i>Numerical Results</i> .....	89
5.5.	SUMMARY .....	97
5.6.	REFERENCES .....	98
<b>CHAPTER 6: A WIDEBAND COMPACT PIFA</b> .....		<b>99</b>
6.1.	INTRODUCTION.....	99
6.2.	GEOMETRY OF THE WC-PIFA.....	99
6.3.	NUMERICAL AND EXPERIMENTAL RESULTS .....	102
6.4.	SUMMARY .....	113
6.5.	REFERENCES .....	114
<b>CHAPTER 7: CONCLUSIONS AND RECOMMENDATIONS</b> .....		<b>115</b>
7.1.	CONCLUSIONS .....	115
7.2.	RECOMMENDATIONS .....	115

# Chapter 1: Introduction

## 1.1. Overview

Mobile communications, wireless interconnects, wireless local area networks (WLANs), and cellular phone technologies compose one of the most rapidly growing industrial markets today. Naturally, these applications require antennas. This being the case, portable antenna technology has grown along with mobile and cellular technologies. It is important to have the proper antenna for a device. The proper antenna will improve transmission and reception, reduce power consumption, last longer and improve marketability of the communication device.

Antennas used for early portable wireless handheld devices were the so-called whip antennas. The quarter-wavelength whip antenna was very popular, mostly because it is simple and convenient [1]. It has an omni-directional pattern in the plane of the earth when held upright and a gain satisfying the device's specifications. New antenna designs have appeared on radios with lower profile than the whip antenna and without significantly reducing performance. These include the quarter-wavelength helical antenna and the "stubby" helical antenna, which is the shortest antenna available.

In recent years, the demand for compact handheld communication devices has grown significantly. Devices smaller than palm size have appeared in the market. Antenna size is a major factor that limits device miniaturization. In the past few years, new designs based on the Planar Inverted-F Antenna (PIFA) and Microstrip Antennas (MSA) have been popular for handheld wireless devices because these antennas have a low profile geometry instead of protruding as most antennas do on handheld radios. Conventional PIFAs and MSAs are compact, with a length that is approximately a quarter to a half of the wavelength. These antennas can be further optimized by adding new

parameters in the design, such as strategically shaping the conductive plate, or judiciously locating loads.

The major limitation of many low-profile antennas is narrow bandwidth. Bandwidth in these antennas is almost always limited by impedance matching. The common criterion is a 2:1 VSWR into a 50- $\Omega$  load. Typical conventional PIFA's have a 5% bandwidth, but advanced designs offer wider bandwidth. A variety of techniques for broadening bandwidth have been reported, including the addition of a parasitic structure whose resonant frequency is near that of the driving antenna structure. One example described in the literature is a stacked microstrip patch antenna [1].

In addition to solving the problem of broadening the antenna bandwidth to the required specifications of the system, one has to worry about developing new structures for devices that require more than one frequency band of operation. Dual-band wireless phones have become popular recently because they permit people to use the same phone in two networks that have different frequencies. Tri-band phones have also gained popularity. Still, there exist more than three frequency bands used for wireless applications. **Table 1-1** lists a few useful wireless applications and their operating frequencies. Systems that require multi-band operation require antennas that resonate at the specified frequencies. This only adds complexity to the antenna design problem.

**Table 1-1**  
Frequency Bands for a Few Wireless Applications

Wireless Applications	Frequency Band (MHz)	Bandwidth (MHz)
Cellular Telephone	824-894	70 (8.1%)
GSM-900	890-960	70 (7.6%)
DCS-1800	1710-1880	170 (10.6%)
PCS-1900	1850-1990	140 (7.3%)
IMT-2000	1885-2200	315 (15.5%)
ISM (including WLAN)	2400-2483	83 (3.4%)
Bluetooth	2400-2500	100 (4.1%)

New applications are arising that will be included in mobile phones. One prominent example is Bluetooth. A potential use for Bluetooth is the ability to walk into an office and set the mobile phone to synchronize with diary and email information on the desktop PC. Therefore, designing an antenna that has multiple frequency bands of interest with one of them in the Bluetooth operating band is a useful structure in today's handheld wireless applications.

## **1.2. Organization of the Thesis**

This thesis reports some preliminary work on a new wideband compact antenna for handheld wireless devices. In addition, a number of issues on electrically small and low-profile antennas in handheld environments are reviewed and studied.

The first design issue is to choose antennas that are suitable for the handheld environment. The candidates should be small and low-profile. Two potential candidates for such an environment are MicroStrip Antennas (MSA) and Planar Inverted-F Antennas (PIFA). These antennas are analyzed in detail in Chapter 2 with various theoretical models. Design issues are described as well.

Small antennas generally have narrow impedance bandwidth, which often limits their widespread use. Chapter 3 treats techniques that can broaden antenna bandwidth. The technique described uses parasitic elements. The analysis of such a structure is performed by computing the capacitance between the parasitic and the driven elements. Two widely used techniques are the edge-coupling structure and the capacitively-fed structure techniques.

Reducing antenna size generally degrades antenna performance. It is therefore important to examine the fundamental limits and parametric tradeoffs involved in size reduction. Chapter 4 reviews the work that has been done over the past five decades on the fundamental limits on the radiation  $Q$  of small antennas. This work is based on Chu

and Harrington's theory. It was expanded using a time-domain formulation introduced by Caswell [2].

In a handheld environment, antennas are mounted on a small ground plane. Therefore, models of antennas on a ground plane with infinite extent are not useful. Chapter 5 investigates ground plane effects on antennas. Results from a thorough numerical study on the performance of a PIFA with various ground plane sizes and shapes is reported. The commercially available method of moments software package called IE3D is used to compute the numerical results. Measurements are also reported for comparison.

Finally, a new wideband compact PIFA antenna (WC-PIFA) is proposed. Preliminary work is shown in Chapter 6. Experimental results were obtained for various environments such as free space, a plastic casing, and in the proximity of a hand. The results show a wide bandwidth that covers frequencies ranging from 1700 MHz to 2500 MHz. This basically covers DCS-1800, PCS-1900, IMT-2000, ISM, and Bluetooth.

Chapter 7 gives a summary of conclusions and suggestions for future work.

### **1.3. References**

- [1] L. Setian, *Practical Communication Antennas with Wireless Applications*, Prentice Hall PTR, New Jersey: 1998.
- [2] E.D. Caswell, W.A. Davis, and W.L. Stutzman, "Fundamental Limits on Antenna Size," Submitted to *IEEE Trans. Ant. Prop.*, April 2000.

# Chapter 2: Overview of Low-Profile Antennas

## 2.1. Introduction

Microstrip antennas and planar inverted-F antennas are increasing in popularity for personal wireless applications. The advantage of these two types of antennas is their low-profile structure. Therefore they are good candidates for embedded antennas in hand-held wireless devices. This chapter describes the two antennas and examines various models of analysis performed in the past as well as the antenna characteristics. A design procedure is also illustrated for each antenna type.

## 2.2. The Microstrip Antenna

### 2.2.1. Introduction

A class of antennas that has gained considerable popularity in recent years is the *microstrip antenna*. A typical microstrip element is illustrated in Fig. 2-1. There are many different types of microstrip antennas, but their common feature is that they consist of four parts:

- a very thin flat metallic region often called the *patch*;
- a *dielectric substrate*;
- a *ground plane*, which is usually much larger than the patch; and
- a *feed*, which supplies the element RF power.

Microstrip elements are often constructed by etching the patch (and sometimes the feeding circuitry) from a single printed-circuit board clad with conductor on both of its sides.

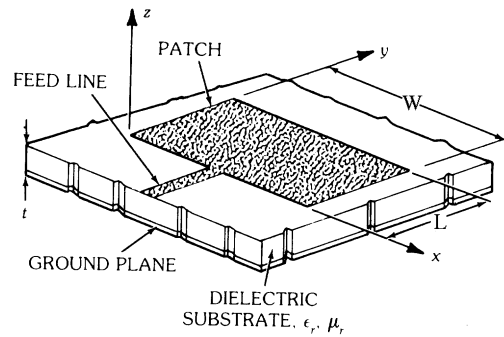


**Figure 2-1.** Geometry for a typical rectangular microstrip element [2].

The length of the patch ( $L$ ) is typically about a third to a half of a free-space wavelength ( $\lambda_0$ ), while the dielectric thickness is in the range of  $0.003\lambda_0$  to  $0.5\lambda_0$ . A commonly used dielectric for such antennas is polytetrafluoral ethylene (PTFE), which has a relative dielectric constant of about 2.5. Sometimes a low-density cellular “honeycomb” material is used to support the patch. This material has a relative dielectric constant near unity and usually results in an element with better efficiency and larger bandwidth [2] but at the expense of an increase in element size. Substrate materials with high dielectric constants can also be used. Such substrates result in elements that are electrically small in terms of free-space wavelengths and consequently have relatively small bandwidth [2] and low efficiency [3].

The reasons microstrip antennas have become so popular include the following:

1. They are low-profile antennas.
2. They are easily conformable to nonplanar surfaces. Along with their low profile this makes them well suited for use on high-performance airframes.
3. They are easy and inexpensive to manufacture in large quantities using modern printed-circuit techniques.
4. When mounted to a rigid surface they are mechanically robust.
5. They are versatile elements in the sense that they can be designed to produce a wide variety of patterns and polarizations, depending on the mode excited and the particular shape of patch used.

6. Adaptive elements can be made by simply adding an appropriately placed pin between the patch and the ground plane. Using such loaded elements, the antenna characteristics can be controlled.

These advantages must be weighed against the disadvantages which can be most succinctly stated in terms of antenna quality factor,  $Q$ . Microstrip antennas are high- $Q$  devices with  $Q$  values sometimes exceeding 100 for thinner elements. High- $Q$  elements have small bandwidths. Increasing the thickness of the dielectric substrate will reduce the  $Q$  of the microstrip element and thereby increase its bandwidth. There are limits, however. As the thickness increases, an increasing fraction of the total power delivered by the source goes into a surface wave. This surface-wave contribution can also be counted as an unwanted power loss since it is ultimately scattered at dielectric bends and discontinuities. Such scattered fields are difficult to control and may have a deleterious effect on the pattern of the element [2]. One also needs to be aware that microstrip elements are modal devices. If the band of the element is so large that it encompasses the resonant frequencies of two or more resonant modes, the pattern is likely not to be stable throughout the band even though the VSWR at the input could be acceptably low.

There are several theories for microstrip antennas that have varying degrees of accuracy and complexity. Among these, two give the best physical insight: the transmission-line model [7] and the Cavity model [5]. More rigorous and complex methods for analyzing the behavior of microstrip elements are the method of moments and finite-difference time domain. Of these, the simplest is the transmission-line model. The cavity model, though somewhat more complex, gives a deeper insight into the operation of microstrip antennas.

### **2.2.2. Transmission Line Model for Microstrip Antennas**

The transmission-line model leads to results that are adequate for most engineering purposes and entail less computation. Although this method has its shortcomings, particularly in that it is applicable only to rectangular or square patch

geometries, the model offers a reasonable interpretation by giving simple expressions of the antenna's characteristics.

The basic concept of a simple transmission-line model is shown in Fig. 2-2. This model is for a rectangular patch fed at an arbitrary point on the  $y$ -axis. The patch is characterized as a microstrip transmission-line with a length  $L$ , width  $W$ , and thickness  $t$ . The radiating edges are along the width dimension of the patch and of length  $W$ . They are modeled as narrow slots radiating into a half-space. The width of the slot is, for the sake of convenience, assumed to be equal to the substrate thickness  $t$ .

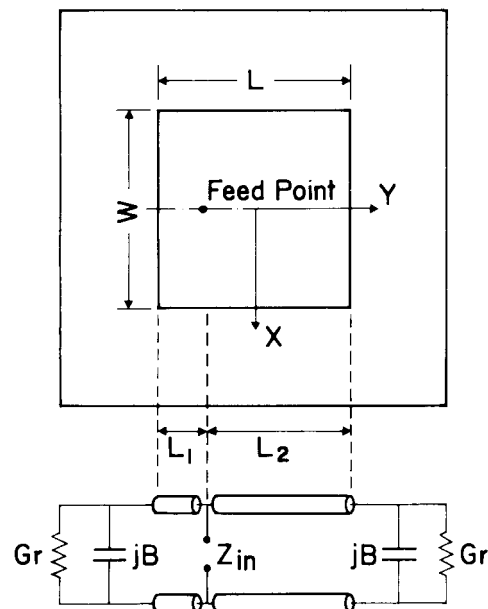


**Figure 2-2.** Rectangular patch antenna fed at arbitrary point on the  $y$ -axis and its equivalent circuit [8].

As a result, the rectangular patch antenna can be represented by two admittances connected by an equivalent microstrip transmission line, as shown on the lower half of Fig. 2-2, where the characteristic impedance  $Z_o$  and the propagation  $\beta_g$  constant for the fundamental mode in the microstrip transmission line are approximated by [8]

$$Z_0 = \frac{1}{Y_0} \approx \frac{\eta_0}{\sqrt{\epsilon_e}} \frac{t}{W} \quad (2.1)$$

and

$$\beta_g \approx k_0 \sqrt{\epsilon_e} \quad (2.2)$$

where  $\eta_0$  and  $k_0$  are the wave impedance and propagation constant in free space, respectively;  $\epsilon_e$  denotes the corresponding effective dielectric constant, and is related to the intrinsic dielectric constant  $\epsilon_r$  of the substrate as follows [8]:

$$\epsilon_e = \frac{\epsilon_r + 1}{2} \frac{\epsilon_r - 1}{2} \left( 1 + 12 \frac{t}{W} \right)^{-\frac{1}{2}} \quad (2.3)$$

The capacitive component,  $B$ , and the conductive component,  $G_r$ , which form each admittance, are related to the fringing field and the radiation loss, and are respectively approximated by [1]

$$B \approx \frac{k_0 \Delta l}{Z_0} \sqrt{\epsilon_e} \quad (2.4)$$

$$G_r \approx \begin{cases} \frac{W^2}{90\lambda_0^2}, & W < 0.35\lambda_0 \\ \frac{W}{120\lambda_0} - \frac{1}{60\pi^2}, & 0.35\lambda_0 \leq W \leq 2\lambda_0 \\ \frac{W}{120\lambda_0}, & 2\lambda_0 < W \end{cases} \quad (2.5)$$

where  $\Delta l$  signifies the line extension due to the fringing effect. This value can be approximated by using the following equation:

$$\Delta l \approx 0.412t \frac{(\epsilon_e + 0.3)(W/t + 0.264)}{(\epsilon_e - 0.258)(W/t + 0.8)} \quad (2.6)$$

From the equivalent circuit in Fig. 2-2, the input admittance of this patch antenna can be shown to be the following [8], if it is regarded as two slot antennas connected by a transmission line having characteristic admittance and propagation constant of  $Y_0$  and  $\beta_g$  approximated by (2.1) and (2.2):

$$Y_{in} = Y_0 \frac{(G_r + jB) + jY_0 \tan(\beta_g L_1)}{Y_0 + j(G_r + jB) \tan(\beta_g L_1)} + Y_0 \frac{(G_r + jB) + jY_0 \tan(\beta_g L_2)}{Y_0 + j(G_r + jB) \tan(\beta_g L_2)} \quad (2.7)$$

where  $L_1$  and  $L_2$  are the respective distances from each patch edge to the feed point. In this case, the resonant condition is given by

$$\text{Im}\{Y_{in}\} = 0 \quad (2.8)$$

where  $\text{Im}\{Y_{in}\}$  represents the imaginary part of  $Y_{in}$ . From (2.8), the following condition can be derived:

$$\tan(\beta_g L) = \frac{2Y_0 B}{G_r^2 + B^2 - Y_0^2} \quad (2.9)$$

The condition above is used to determine the resonant frequency when the patch length  $L$  is given, or, conversely, to determine the resonant length  $L$  when the desired operating frequency is given. Considering this resonant condition, (2.7) is reduced by substituting (2.9) into it as follows [6]:

$$Y_{in} = 2G_r \left[ \cos^2(\beta_g L_1) + \frac{G_r^2 + B^2}{Y_0^2} \sin^2(\beta_g L_1) - \frac{B}{Y_0} \sin(2\beta_g L_1) \right]^{-1} \quad (2.10)$$

The accuracy of the transmission-line model strongly depends on the accuracy of the approximations for the circuit parameters,  $G_r$ ,  $B$ ,  $G_m$ , and  $B_m$ , where

$$Y_m = G_m + jB_m \quad (2.11)$$

A more accurate transmission-line model can be used, namely the three-port transmission-line model. This model can include the mutual coupling between the two slots that has been neglected. That results in a more accurate approximation of the circuit parameters [8].

As mentioned previously, the rectangular patch antenna is represented by two slots separated by a distance  $L$ . In this case, each slot can be thought of as radiating the same field as a magnetic dipole with a magnetic current of

$$\mathbf{M} = 2E\hat{\mathbf{z}} = \frac{2V_0}{t}\hat{\mathbf{z}} \quad (2.12)$$

where the factor 2 arises due to the positive image of magnetic current, in the near by ground plane, and  $V_0$  is the voltage across the slot. The total radiation field is obtained by multiplying the field due to a single slot by an array factor representing the arrangement of the two-slot array. When the coordinate system shown in Fig. 2-2 is employed, the final result is [8]

$$E(\theta) = -4V_0Wk_0 \frac{e^{-jk_0R}}{4\pi R} \frac{\sin\left(\frac{k_0t \sin\theta}{2}\right)}{\left(\frac{k_0t \sin\theta}{2}\right)} \cos\left(\frac{k_0L}{2} \sin\theta\right) \quad (2.13)$$

in the E-plane and

$$E(\theta) = -4V_0Wk_0 \frac{e^{-jk_0R}}{4\pi R} \frac{\sin\left(\frac{k_0W \sin\theta}{2}\right)}{\left(\frac{k_0W \sin\theta}{2}\right)} \cos\theta \quad (2.14)$$

in the H-plane.

### 2.2.3. Cavity Model for Microstrip Antennas

Although the transmission-line model discussed in the previous section is easy to use, it has some inherent disadvantages. Specifically, it is only useful for patches of rectangular design and it ignores field variations along the radiating edges. These disadvantages can be overcome by employing the cavity model.

The cavity model treats the region between two parallel conductor planes, consisting of a patch radiator and a ground plane, as a cavity bounded by the electric walls and a magnetic wall along the periphery of the patch. Once the field distribution is known, Huygens' principle can be applied to the magnetic wall of the cavity. Radiation field can then be evaluated. This method is most suitable for analyzing patch antennas having geometries for which the corresponding wave equation can be solved by the method of separation of variables. However, this method is applicable for any arbitrary shaped patch antennas in general.

The geometry of the analytical model is illustrated in Fig. 2-3. In this figure, an arbitrarily shaped patch is located on the surface of the grounded dielectric substrate of thickness  $t$  and dielectric constant  $\epsilon_r$ , where  $C$  denotes the boundary line of the patch radiator,  $S$  is the area surrounded by the boundary line  $C$ , an  $\hat{n}$  is the unit vector, outer normal to the boundary. The magnetic cavity model works best for a thin substrate. In this case, the TM modes are superior in the cavity. The cavity model makes the following assumptions:

1. The electric field is  $z$ -directed, and the magnetic field has only a transverse component in the cavity.
2. Since the substrate is assumed thin, the fields in the cavity do not vary with  $z$ .
3. The tangential component of the magnetic field is negligible at the edge of the patch.
4. The existence of a fringing field can be accounted for by slightly extending the edges of the patches.

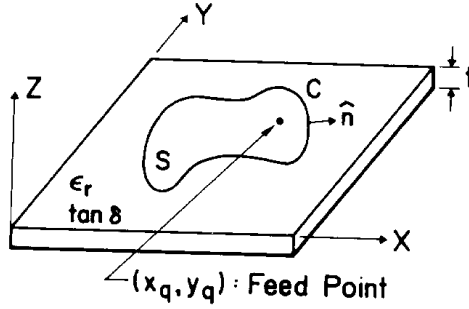


**Figure 2-3.** Arbitrarily shaped patch antenna and coordinate system [8].

If an  $e^{j\omega t}$  time variation is assumed, the fields from a z-directed current source at the point  $(x_q, y_q)$  satisfy the following Maxwell's relations:

$$(\nabla_T^2 + k^2)E_z = -j\omega\mu_o \mathbf{J}_z(x_q, y_q) \quad (2.15)$$

$$\mathbf{H} = \frac{j}{\omega\mu_o} \nabla_T \times (\hat{\mathbf{z}}E_z) \quad (2.16)$$

where  $\nabla_T$  is the transverse component with respect to the z-axis of the del operator,  $\hat{\mathbf{z}}$  is the unit vector in the z-direction, and k is  $k_o\sqrt{\epsilon_r}$ . The relations above satisfy the electric wall condition because  $\mathbf{E} = E_z\hat{\mathbf{z}}$ . The magnetic wall condition on the sides of the cavity can be satisfied by the following Neumann boundary conditions:

$$\frac{\partial E}{\partial n} = 0 \quad (2.17)$$

The expression in (2.15) is an inhomogeneous wave equation that can be solved by finding eigenfunctions,  $\varphi^{(l)}$ , that satisfy the following homogeneous wave equation

$$(\nabla_T^2 + (k^{(l)})^2)\varphi^{(l)} = 0 \quad (2.18)$$

for the boundary condition in (2.17). In this homogeneous wave equation,  $k^{(l)}$  is the eigenvalue that corresponds to the eigenvector  $\varphi^{(l)}$ . Therefore, if N modes exist in the cavity and N eigenvectors are derived, the solution to (2.18) is given by

$$E_z(x, y) = \sum_{l=1}^N A^{(l)} \varphi^{(l)}(x, y) \quad (2.19)$$

For an antenna with one input terminal, the values of the coefficients are expressed as

$$A^{(l)} = \frac{\sqrt{2S_e}}{t} \frac{M^{(l)*}}{j\omega C + \frac{1}{j\omega L^{(l)}} + g^{(l)}} I_q \quad (2.20)$$

where

$$\begin{aligned} M^{(l)} &= \sqrt{2S_e} \varphi^{(l)}(x, y) \\ C &= \epsilon_r \epsilon_o \frac{S_e}{t} \\ L^{(l)} &= \frac{1}{(\omega^{(l)})^2 C} \\ \omega^{(l)} &= \frac{k^{(l)}}{\sqrt{\epsilon_r \epsilon_o \mu_o}} \end{aligned} \quad (2.21)$$

In (2.20),  $S_e$  is the effective area of the cavity including the extension due to the fringing fields, and  $g^{(l)}$  is the factor that accounts for conductor, dielectric and radiation loss given by [8]

$$g^{(l)} = g_c^{(l)} + g_d^{(l)} + g_r^{(l)} \quad (2.22)$$

where

$$\begin{aligned}
g_c^{(l)} &= \frac{2R_s}{t\mu_o} \left( \frac{\omega^{(l)}}{\omega} \right)^2 C \\
g_d^{(l)} &= \omega C \tan(\delta) \\
g_r^{(l)} &= \frac{2S_e}{t^2} P_{r0}^{(l)}
\end{aligned} \tag{2.23}$$

and  $R_s$  is the real part of the surface impedance of the conductor walls, and  $P_{r0}^{(l)}$  is written as

$$P_{r0}^{(l)} = \frac{1}{2} \text{Re} \left\{ \iint (\mathbf{E}_o^{(l)} \times \mathbf{H}_o^{(l)}) \cdot \hat{\mathbf{R}} \sin \theta d\theta d\phi \right\} \tag{2.24}$$

where

$$\mathbf{E}_o^{(l)} = \eta \mathbf{H}_o^{(l)} \times \hat{\mathbf{R}} \quad \left( 0 \leq \theta \leq \frac{\pi}{2} \right) \tag{2.25}$$

$$\mathbf{H}_o^{(l)} = \frac{-j\omega\epsilon_o}{4\pi} t \left[ 2 \cos \left( \frac{k_o t}{2} \cos \theta \right) \right] \oint_c (\hat{\mathbf{n}} \times \hat{\mathbf{z}}) \varphi^{(l)}(r) e^{jk_o \vec{\mathbf{r}} \cdot \hat{\mathbf{R}}} dl \tag{2.26}$$

and  $\hat{\mathbf{R}}$  is the spherical coordinate unit vector in the  $r$  direction. In (2.25) and (2.26),  $\vec{\mathbf{r}}$  is a vector from the coordinate origin to a reference point on the periphery of the patch antenna,  $\varphi^{(l)}(r)$  is the value of the eigenfunctions at the end of  $\vec{\mathbf{r}}$ ,  $\eta_o$  is the impedance of free space, and  $k_o$  is the free space wave number. The conductor and dielectric losses,  $g_c^{(l)}$  and  $g_d^{(l)}$  are due to the power dissipated in the copper walls and dielectric substrate, respectively, from the fields interior to the cavity [14].

The input impedance of a microstrip patch antenna is given by [8]

$$Z_{in} = \sum_{l=1}^N \frac{|M^{(l)}|^2}{j\omega C + \frac{1}{j\omega L^{(l)}} + g^{(l)}} \tag{2.27}$$

Substituting (2.20) into (2.19) determines the field of the MSA. The expressions (2.25) and (2.26) give the contribution of each mode in the cavity to the radiating fields. The total radiated field is the sum of the contributions from each resonant mode in the cavity, given by

$$E_{\theta} = \sum_{n=1}^l A^{(l)} \mathbf{E}_0^{(l)} \cdot \hat{\boldsymbol{\theta}} \quad (2.28)$$

$$E_{\phi} = \sum_{n=1}^l A^{(l)} \mathbf{E}_0^{(l)} \cdot \hat{\boldsymbol{\phi}} \quad (2.29)$$

where  $\hat{\boldsymbol{\theta}}$  and  $\hat{\boldsymbol{\phi}}$  are unit vector in the  $\theta$  and  $\phi$  directions in polar coordinates, respectively.

This section has presented the magnetic cavity model as a method of analysis applicable to planar microstrip antennas. In the next section, a design procedure is described for microstrip patch antennas.

#### 2.2.4. Design Procedure

The main design goal for a microstrip patch antenna is to determine the substrate properties and patch dimensions necessary to satisfy the specific performance characteristics over the required frequency band. The usual design procedure, however, only takes resonant frequency into account, and does not consider the required bandwidth. The designer is forced to obtain the required bandwidth with a step-by-step, or trial-and-error, design technique. Before completing the design procedure, however, one needs to find a way to determine the location of the feed point to match to the characteristic impedance of the MSA. The feed can be easily located by using another design chart obtained by numerical calculation or experiment [8].

In the typical procedure, the thickness and the dielectric constant of the substrate are known. Then, a patch antenna that operates at the required resonant frequency can be designed by following the flow chart shown in Fig. 2-4 [8], where (a) is for rectangular MSA and (b) is for a circular one. In the rectangular case, as shown in Fig. 2-2, we know that the greater the width  $W$ , the higher radiation efficiency becomes. However, excessive width is not desirable because the influence of higher order modes becomes significant and the original characteristics may suffer some degradation as a result. This implies that there exists an optimum value for the width. The ideal width for practical use can be determined from the design flow chart in Fig. 2-4, although the value may not be optimum.

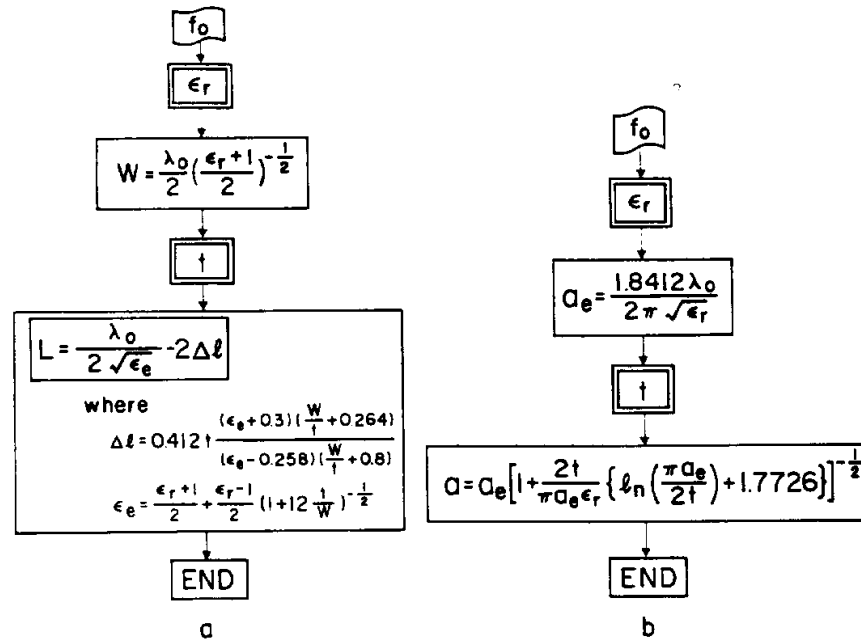


**Figure 2-4.** Flow chart based on usual design procedure [8] (a) for a rectangular patch antenna and (b) for a circular patch antenna.

To introduce the bandwidth parameter into the procedure, consider the equivalent circuit of any patch antenna shown in Fig. 2-5. In this parallel resonant circuit, the following expressions (2.30) and (2.31) describe the relationships for a VSWR less than  $\rho$  between the unloaded quality factor  $Q$  of the circuit and the relative bandwidth  $B_r$ ,

defined as  $\frac{f_u - f_l}{f_c}$  where  $f_u$  and  $f_l$  are the upper and the lower frequency points of the band, respectively, where the VSWR is equal to  $\rho$ , and  $f_c$  is the center frequency of the band [4]:

$$Q_0 B_r = \sqrt{(\beta\rho - 1)\left(1 - \frac{\beta}{\rho}\right)} \quad (2.30)$$

where  $Q_0$  is the unload  $Q$  and  $\beta$  is the coupling coefficient, defined by

$$\beta = \frac{G_0}{G'} \quad (2.31)$$

$G_0$  is the conductance of the transmission line and  $G'$  is the conductance of the patch antenna. Note that (2.30) gives the maximum value for the product of bandwidth and  $Q$  factor. The maximum value can be obtain by [4]

$$Q_0 B_r = \frac{\rho^2 - 1}{2\rho} \quad (2.32)$$

when the following condition is satisfied for the coupling coefficient:

$$\beta = \beta_0 = \frac{\rho^2 + 1}{2\rho} \quad (2.33)$$

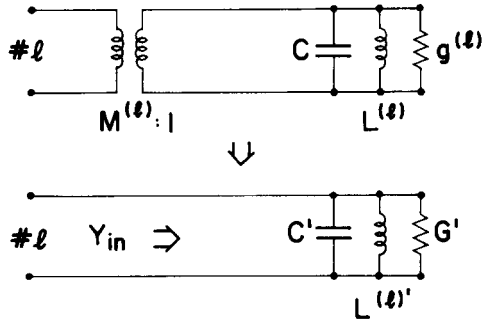


**Figure 2-5.** Equivalent circuit with single port terminal when mode #1 is dominant [4].

These relationships are illustrated in Fig. 2-6. Figure. 2-6 (a), representing (2.32), shows that one can obtain the unloaded  $Q$  required for the antenna when the desired bandwidth and VSWR are specified. In Fig. 2-6 (b), representing (2.33), the position of the feed point can be determined when its characteristic impedance is given, or the characteristic impedance necessary for the feed line when the position of the feed point is given.

However, experiments and simulations reported in [4] give the following relationship for patch antennas, when  $S$  is the physical area of the patch radiator:

$$Q_0 \approx F_1 \left( \frac{\sqrt{S}}{t}, \epsilon_r \right) \quad (2.34)$$

$$\sqrt{S} f_0 \approx F_2 \left( \frac{\sqrt{S}}{t}, \epsilon_r \right) \quad (2.35)$$

These relations imply that both the unloaded  $Q$  and the product of the resonant frequency  $f_0$  and the square root of the physical patch area can be expressed as a function of  $\frac{\sqrt{S}}{t}$  and  $\epsilon_r$ . These characteristics can be arranged in the form of design charts for every patch shape. For example, Figs. 2-7 and 2-8 depicts (2.34) and (2.35) in such a form for a square patch.

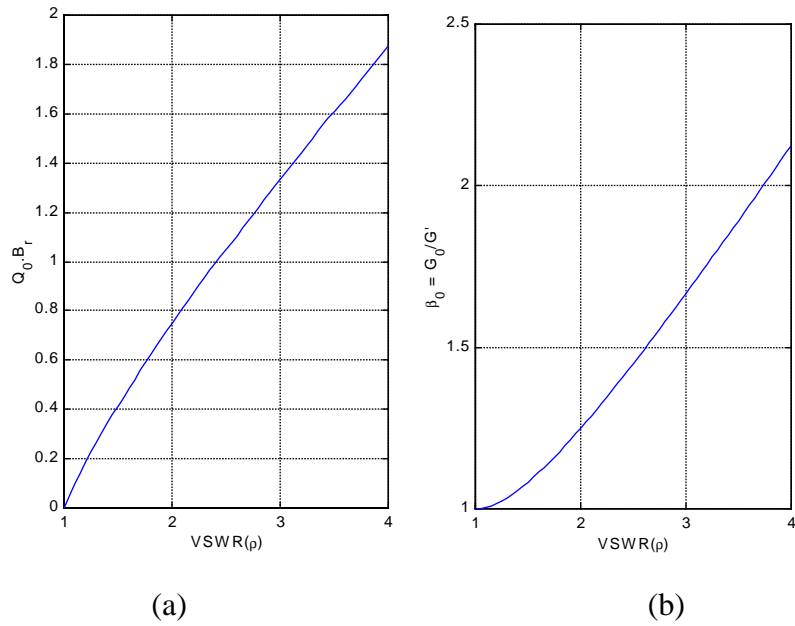


**Figure 2-6.** Design chart to determine maximum value of (a)  $Q_0 B_r$  and (b) coupling coefficient

$\beta_0 = \frac{G_0}{G'}$  versus desired VSWR ( $\rho$ ) [4].

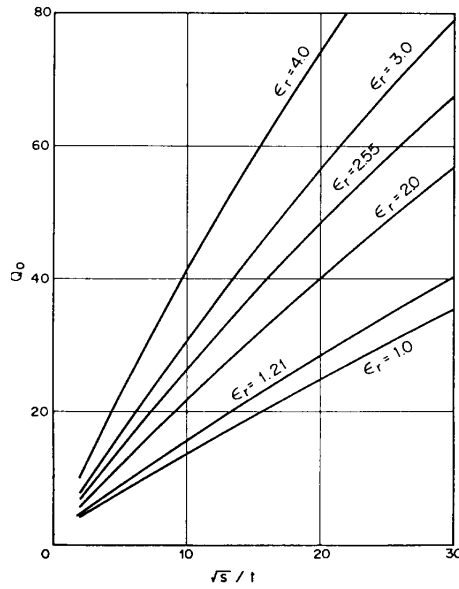


**Figure 2-7.** Design chart to determine unloaded Q value versus  $\frac{\sqrt{S}}{t}$  with  $\epsilon_r$  as a parameter for square patch antenna [4].

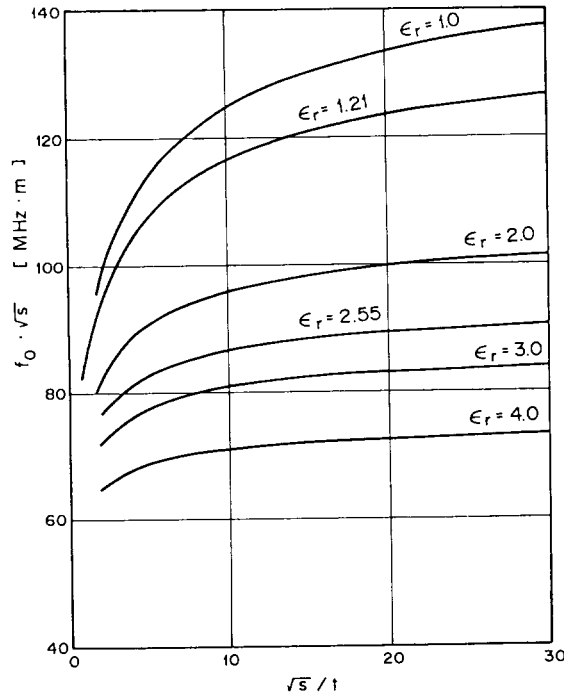


**Figure 2-8.** Design chart to determine unloaded Q value versus  $\frac{\sqrt{S}}{t}$  with  $\epsilon_r$  as a parameter for square patch antenna [4].

By using these four design plots, a square patch ( $L=W$ ) antenna for a specified bandwidth can be designed. That is, the unloaded Q value necessary for the antenna to satisfy the desired VSWR over the specified bandwidth is found from Fig. 2.6 (a) or from (2.32). Next the parameter  $\frac{\sqrt{S}}{t}$  is determined from Fig. 2-7 according to the selected dielectric constant  $\epsilon_r$ . Then, the product  $f_0\sqrt{S}$  is obtained from Fig. 2-8 because  $\frac{\sqrt{S}}{t}$  and  $\epsilon_r$  have already been determined. The patch area S can be computed for the specified resonant frequency  $f_0$ . Finally, the substrate thickness t can be determined from the value  $\frac{\sqrt{S}}{t}$ .

Before concluding the design process of patch antennas, the location of the feed point has to be determined. Suzuki [9] reported the simple dependence of the input impedance of the patch antenna on the location of its probe feed point. Numerical computation and experimental results of this input impedance and probe feed location

relation are illustrated in Fig. 2-9 for both square and circular patch antennas at the resonant frequency of the lowest-order mode. In this figure, the solid line represents the relative impedance variation for a square patch as the feed point is moved along the y-axis at  $x=0$  and the broken line is for a circular patch as it is moved along the radial axis at  $\phi = \phi_0$ . Note that the curves are slightly different. This relationship can also be approximated by the following expression [8]:

$$\frac{R_{in}(0, y)}{R_{in}(0, Y_e)} \approx \frac{R_{in}(y)}{R_{in}^{(e)}(Y_e)} \approx \cos^2 \left[ \frac{\pi}{2} \left( \frac{2y}{L} - 1 \right) \right] \quad (\text{Square patch}) \quad (2.36)$$

$$\frac{R_{in}(r, \phi_0)}{R_{in}(a_e, \phi_0)} \approx \frac{R_{in}(r)}{R_{in}(a)} \approx \left[ \frac{J_1 \left( 1.841 \frac{r}{a} \right)}{J_1(1.841)} \right]^2 \quad (\text{Circular patch}) \quad (2.37)$$

where  $Y_e$  and  $a_e$  are the y and r coordinates of the effective patch edge previously discussed, respectively.  $R_{in}^{(e)}$  and  $R_{in}(a)$  represent the input impedances at the physical edge, such as  $(0, L/2)$  for the square patch and  $(a, \phi_0)$  for the circular one.

In the case of a square patch antenna, it is useful to know the input impedance as a function of feed location x along the edge of the patch, as shown in Fig. 2-10. Numerical simulations of this variation calculated using the method of moments are depicted in Fig. 2-10. The feed point is moved along the x-axis at  $y = L_e / 2 \approx L / 2$  with the antenna operating resonant frequency of the  $TM_{010}$  mode. This impedance variation can also be approximated by

$$\frac{R_{in}(x, Y_e)}{R_{in}(0, Y_e)} \approx \frac{R_{in}'(x)}{R_{in}^{(e)'}} \approx 1 + \cos^2 \left[ \frac{\pi}{2} \left( \frac{2x}{W} - 1 \right) \right] \quad (2.38)$$

The dots in Fig. 2-10 denote values obtained from (2.38), which, in this case, agree with the numerical simulation values.

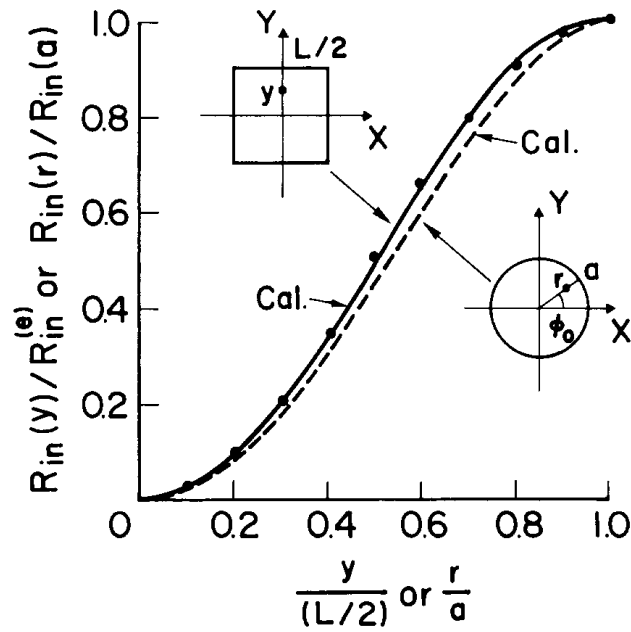


Figure 2-9. Input impedance variations calculated using the method of moments for square and circular patch antennas, when the feed point is moved along the y-axis [9].

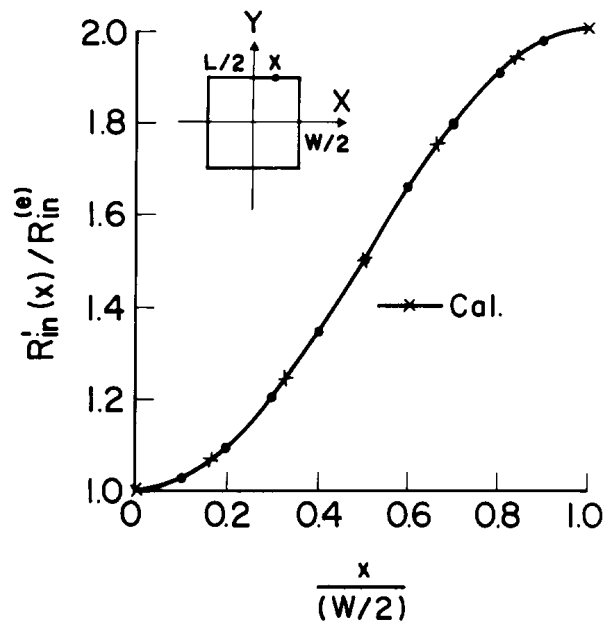
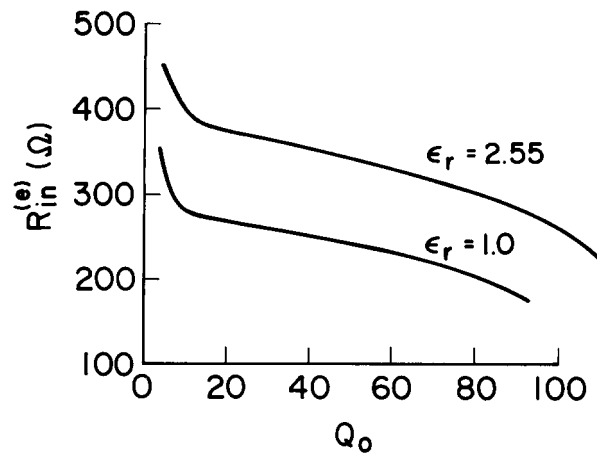


Figure 2-10. Input impedance variations calculated using the method of moments for square antennas, when the feed point is moved along edge [9].

By using the results in Figs. 2-9 and 2-10, the feed location can be determined to match the impedance condition if the input impedance at the patch edge,  $R_{in}^{(e)}$  for the square patch or  $R_{in}(a)$  for the circular patch, is known. An expression of this impedance is found in [9] as a function of the dielectric constant  $\epsilon_r$  of the substrate used and the unloaded  $Q$  factor:

$$R_{in}^{(e)} \text{ or } R_{in}(a) \approx F_3(Q_0, \epsilon_r) \quad (2.39)$$

Figure 2-11 shows some numerical simulation results of (2.39) for the square and circular patch antennas [9] as a function of unloaded  $Q$  with  $\epsilon_r$  as a parameter.



**Figure 2-11.** Relationship between input impedance at edge, dielectric constant, and unloaded  $Q$  for (a) square patch and (b) circular patch [10].

### 2.2.5. Summary

This chapter introduced two basic methods of analyzing microstrip patch antennas based on the transmission line model and the cavity model. These models are easier to understand than the numerical analysis methods, such as the method of moments or the finite-difference time domain, and give more insight on the behavior and characteristics of the antennas. A design procedure that takes the bandwidth and feed location into

account were presented as well. The design charts were generated using data from simulations results and experiments.

## **2.3. The Planar Inverted-F Antenna**

### **2.3.1. Introduction**

The Planar inverted-F antenna (PIFA), as shown in Fig. 2-11(a), is currently in use as an embedded antenna in some radiotelephone handsets, especially in Japan. It is one of the most promising antenna types because it is small and has a low profile, making it suitable for mounting on portable equipment. The PIFA typically consists of a rectangular planar element, ground plane, and short-circuit plate of narrower width than that of the shortened side the planar element. The PIFA can be thought of as a combination of the inverted-F (IFA) and the short-circuit rectangular microstrip antennas (SC-MSA), as shown in Fig. 2-11. Both the IFA and SC-MSA have small bandwidths, but the PIFA has sufficient bandwidth to cover popular communication bands (about 8%). The PIFA is an IFA with the wire radiator element replaced by a plate to increase the bandwidth. The IFA is known as a “shunt-driven” inverted-L antenna-transmission line with an open end [10]. The PIFA also can be viewed as a short-circuit microstrip antenna resonated with the  $TM_{100}$  dominant mode. The length of the rectangular element is halved by placing a short-circuit plate between the radiator element and ground plane at the position where the electric field of the  $TM_{100}$  mode is zero [2]. When the width of the short-circuit plate is narrower than that of the planar element, the effective inductance of the antenna element increases, and the resonant frequency becomes lower than that of a conventional short-circuit MSA having the same sized planar element [2]. As a result, the size of the short-circuit MSA can be further reduced. With the width of the short-circuit plate reduced, the final structure resembles a PIFA.

Studies on the conventional PIFA have been performed in recent years. However, no simple model providing a clear understanding of its behavior and characteristics exists

at the present time. Numerical analysis is the primary method for evaluating PIFA performance. This chapter presents the analytical characteristics of a PIFA when the width of the short-circuit plate and size ratio of the planar element are varied. The analysis assumes that the size of the ground plane is infinite or large enough to be considered as infinite. Finite ground plane effects are discussed in Chapter 5.

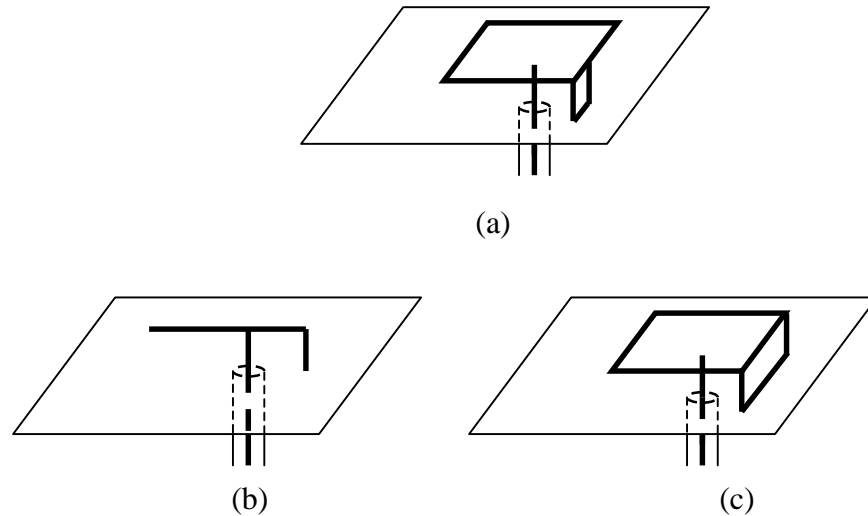


**Figure 2-11.** The PIFA antenna in (a) combines elements of the IFA antenna in (b) and MSA antenna in (c).

### 2.3.2. Analysis Model

Figure 2-12 shows the structure of the PIFA, which is formed by a rectangular element placed parallel to and above a ground plane and a short-circuit plate. The excellent work on the analysis of the PIFA by [8] uses spatial network method (SNM) to generate numerical results. The SNM, which is a three-dimensional time-domain numerical analysis method, is discussed in detail in [11]. The antenna is broken up into three-dimensional cubical grid whose size length is  $\Delta d$ . The size of the analysis volume is set large enough so that the numerical results converge because the extent of the gridding affects the results of the analysis. This assumes also that the ground plane is large enough so that it can be considered as infinite in extent.

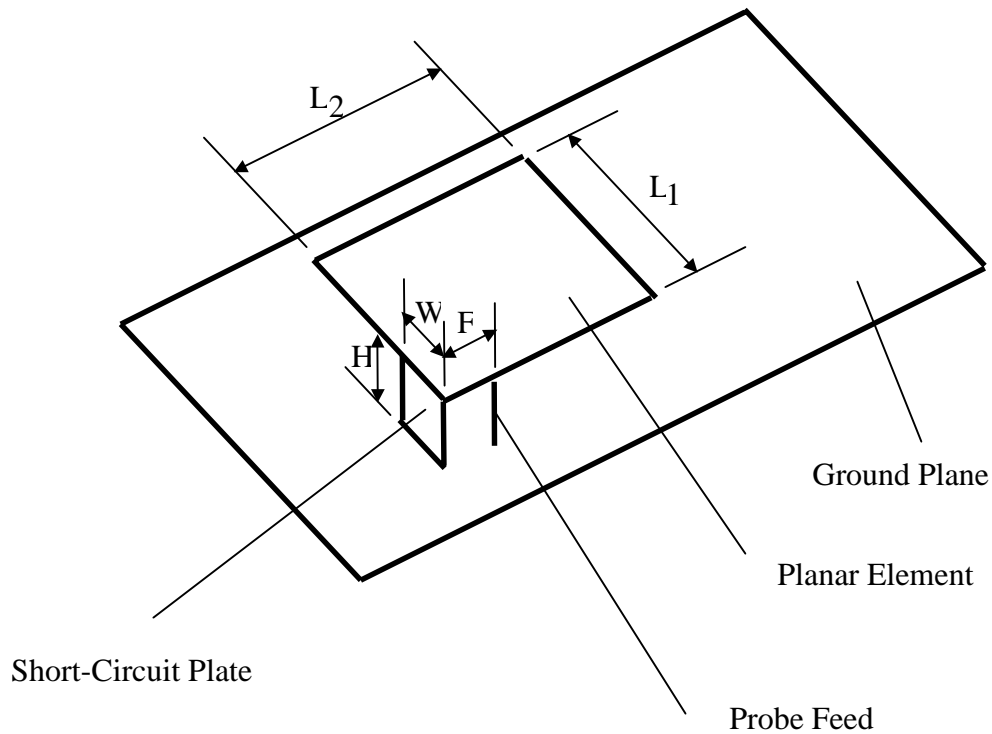


**Figure 2-12.** Structure of the planar inverted-F antenna.

The spatial network method, proposed by N. Yoshida, *et al.* [12] in the late 1970s, presents a model of a wave propagation mechanism based on the difference form of Maxwell's equations. In considering these equations in a three-dimensional space, at each discrete point, each field variable is assigned to satisfy the mutual relationship between the variables derived from the equations. The resultant arrangement of the variables is the same as in the FD-TD and TLM methods, as is the correspondence of each component equation in Maxwell's equations to each of the respective points, which are identified in Fig. 2-13 as A, B, C, D, E, and F. In the spatial network method, an equivalent circuit is constructed on the following three principles. First, it is assumed that the interval between the discrete points is a one-dimensional line. Second, every point is treated as a node where the continuity law for electric or magnetic currents holds. Finally, the medium conditions are expressed as lumped elements. To realize the network on these principles, all electromagnetic variables correspond to circuit variables at each node. This correspondence is shown in Table 2.1 [12]. By using these equivalent circuit variables, each component in Maxwell's equation assigned at each node is transformed into two-

dimensional transmission equation. This equation expresses the transmission of the plane wave perpendicular to the direction of the equivalent voltage defined at each node. The Bergeron method [12] is then used to solve for three-dimensional electromagnetic fields in the time domain using the equivalent circuits of the fields.

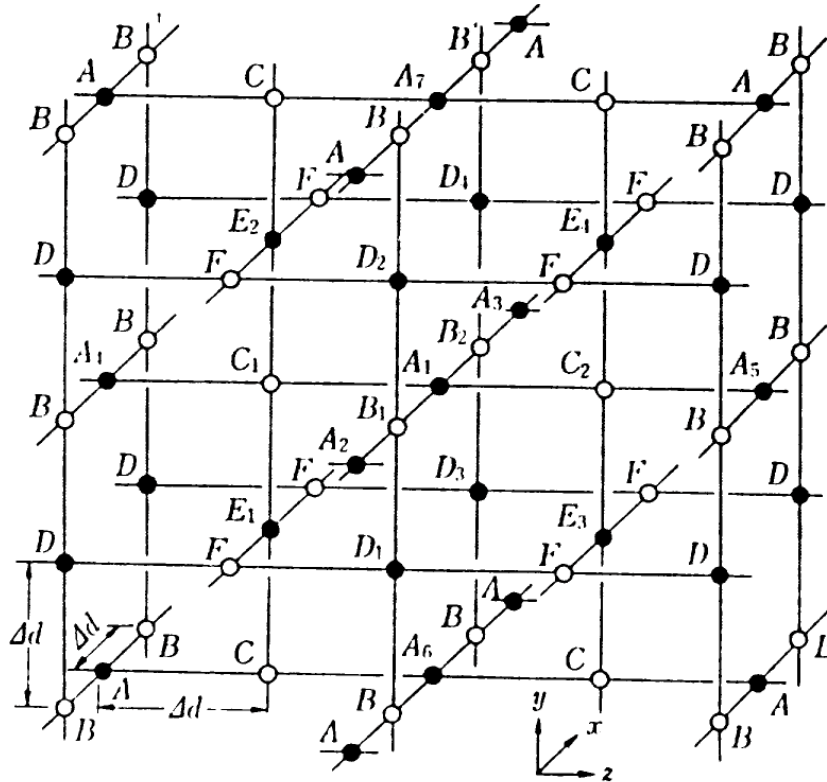


**Figure 2-3.** Three-dimensional cubic lattice network ( $\Delta d$ : the interval of spatial discretization [12]).

**Table 2.1**

Correspondence between the field variables and Medium constants and the circuit variables and constants at each node in the equivalent circuit [12].

	Electric Node			Magnetic Node	
	Maxwell's equs.	Variables		Maxwell's equs.	Variables
$A_n$	$\frac{\partial H_x}{\partial z} - \frac{\partial H_z}{\partial x} = \epsilon_0 \frac{\partial E_y}{\partial t}$ $-\frac{\partial E_y}{\partial z} = -\mu_0 \frac{\partial H_x}{\partial t}$ $\frac{\partial E_y}{\partial x} = -\mu_0 \frac{\partial H_z}{\partial t}$	$V_y \equiv E_y$ $I_x \equiv -H_x$ $I_x \equiv H_x$	$F_n$	$\frac{\partial E_x}{\partial z} - \frac{\partial E_z}{\partial x} = -\mu_0 \frac{\partial H_y}{\partial t}$ $-\frac{\partial H_y}{\partial z} = \epsilon_0 \frac{\partial E_x}{\partial t}$ $\frac{\partial H_y}{\partial x} = \epsilon_0 \frac{\partial E_z}{\partial t}$	$V_y^* \equiv H_y$ $I_x^* \equiv E_x$ $I_x^* \equiv -E_x$
$D_n$	$\frac{\partial H_x}{\partial y} - \frac{\partial H_y}{\partial z} = \epsilon_0 \frac{\partial E_x}{\partial t}$ $\frac{\partial E_x}{\partial z} = -\mu_0 \frac{\partial H_y}{\partial t}$ $-\frac{\partial E_x}{\partial y} = -\mu_0 \frac{\partial H_z}{\partial t}$	$V_x \equiv E_x$ $I_x \equiv H_y$ $I_y \equiv -H_x$	$B_n$	$\frac{\partial E_y}{\partial x} - \frac{\partial E_x}{\partial y} = -\mu_0 \frac{\partial H_z}{\partial t}$ $\frac{\partial H_x}{\partial y} = \epsilon_0 \frac{\partial E_x}{\partial t}$ $-\frac{\partial H_x}{\partial x} = \epsilon_0 \frac{\partial E_y}{\partial t}$	$V_x^* \equiv H_x$ $I_y^* \equiv -E_x$ $I_x^* \equiv E_y$
$E_n$	$\frac{\partial H_y}{\partial x} - \frac{\partial H_x}{\partial y} = \epsilon_0 \frac{\partial E_z}{\partial t}$ $\frac{\partial E_x}{\partial y} = -\mu_0 \frac{\partial H_x}{\partial t}$ $-\frac{\partial E_x}{\partial x} = -\mu_0 \frac{\partial H_y}{\partial t}$	$V_x \equiv -E_x$ $I_y \equiv -H_x$ $I_x \equiv H_y$	$C_n$	$\frac{\partial E_x}{\partial y} - \frac{\partial E_y}{\partial z} = -\mu_0 \frac{\partial H_x}{\partial t}$ $\frac{\partial H_x}{\partial z} = \epsilon_0 \frac{\partial E_y}{\partial t}$ $-\frac{\partial H_x}{\partial y} = \epsilon_0 \frac{\partial E_x}{\partial t}$	$V_x^* \equiv -H_x$ $I_x^* \equiv E_y$ $I_y^* \equiv -E_x$
<b>Permittivity</b>		$C_0 = \epsilon_0/2$	<b>Permittivity</b>		$L_0^* = \epsilon_0/2$
<b>Permeability</b>		$L_0 = \mu_0/2$	<b>Permeability</b>		$C_0^* = \mu_0/2$
<b>Polarization</b>		$\Delta C = \epsilon_0 \chi_e / 2 \cdot \Delta d$	<b>Magnetization</b>		$\Delta C^* = \mu_0 \chi_m / 2 \cdot \Delta d$
<b>Conductivity</b>		$G = \sigma / 2 \cdot \Delta d$	<b>Magnetic Conductivity</b>		$G^* = \sigma^* / 2 \cdot \Delta d$

### 2.3.3. Field and Current Distribution

Fig 2-14 illustrates the distribution of the electric field  $E_x$ ,  $E_y$ , and  $E_z$  computed using the spatial network method [11] for different cases where the width of the short-circuit plate is changed as  $2\Delta d$ ,  $4\Delta d$ ,  $8\Delta d$ , and  $12\Delta d$ , respectively, when the planar element has the size of  $L_1=L_2=16\Delta d$  and  $H=4\Delta d$ . The result shows clearly that the dominant electric field  $E_z$  is zero at the short-circuit plate and is considerably large at the opposite edge of the short-circuit plate. The peaked parts of the electric field distributions  $E_x$  and  $E_y$  are located at the feed point. Also, the electric fields are generated at all open-

circuited edges of the planar element. These fringing fields are the radiating sources in PIFAs.

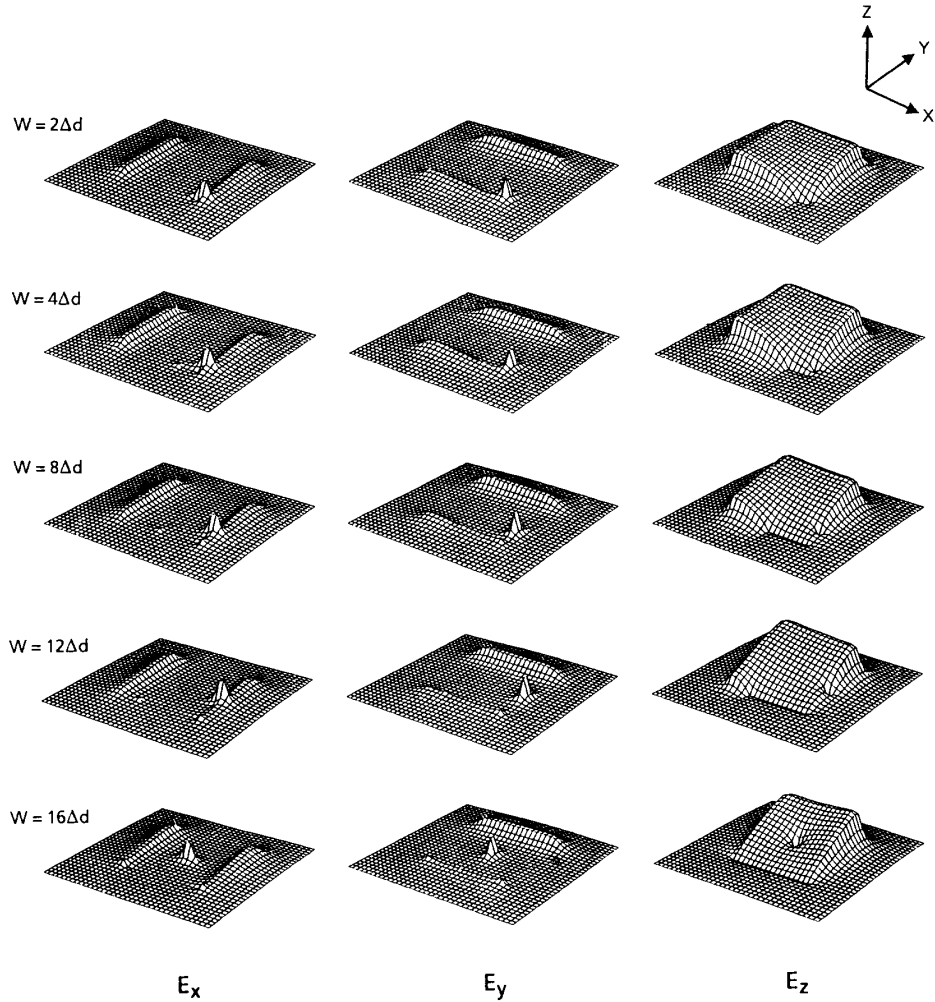


**Figure 2-14.** Distribution of the electric fields  $E_x$ ,  $E_y$ ,  $E_z$  at the  $x$ - $y$  plane, where observed plane is at the height of  $2.5 \Delta d$  from the ground plane for  $E_z$  field and  $2 \Delta d$  for  $E_x$  and  $E_y$  fields computed using SNM [8].

The surface current distributions at resonance were computed using SNM and reported in [8] for various widths of the short-circuit plate. Fig. 2-15 shows the current distribution intensity and direction: the upper, middle, and lower distributions show the surface current on the upper surface, the underneath surface of the planar element, and

the ground plane, respectively. The black dot shows the probe feeding point. The arrows show the direction of the current and its intensity is proportional to the arrow length. Fig. 2-15 points out two important results related to the intensity of the surface current and the effective length of the current flow. Very large current flows underneath the planar element and on the ground plane. These currents contribute to the interior electric and magnetic fields, between the planar element and the ground plane. The intensity of the current on the upper surface of the planar element is relatively small. When the width of the short-circuit plate is narrowed, the current distribution changes and the effective length of the current flow on the short-circuit plate and planar element becomes longer. Consequently, the resonant frequency is reduced. Therefore, a PIFA that is smaller than the short-circuit MSAs can be designed.

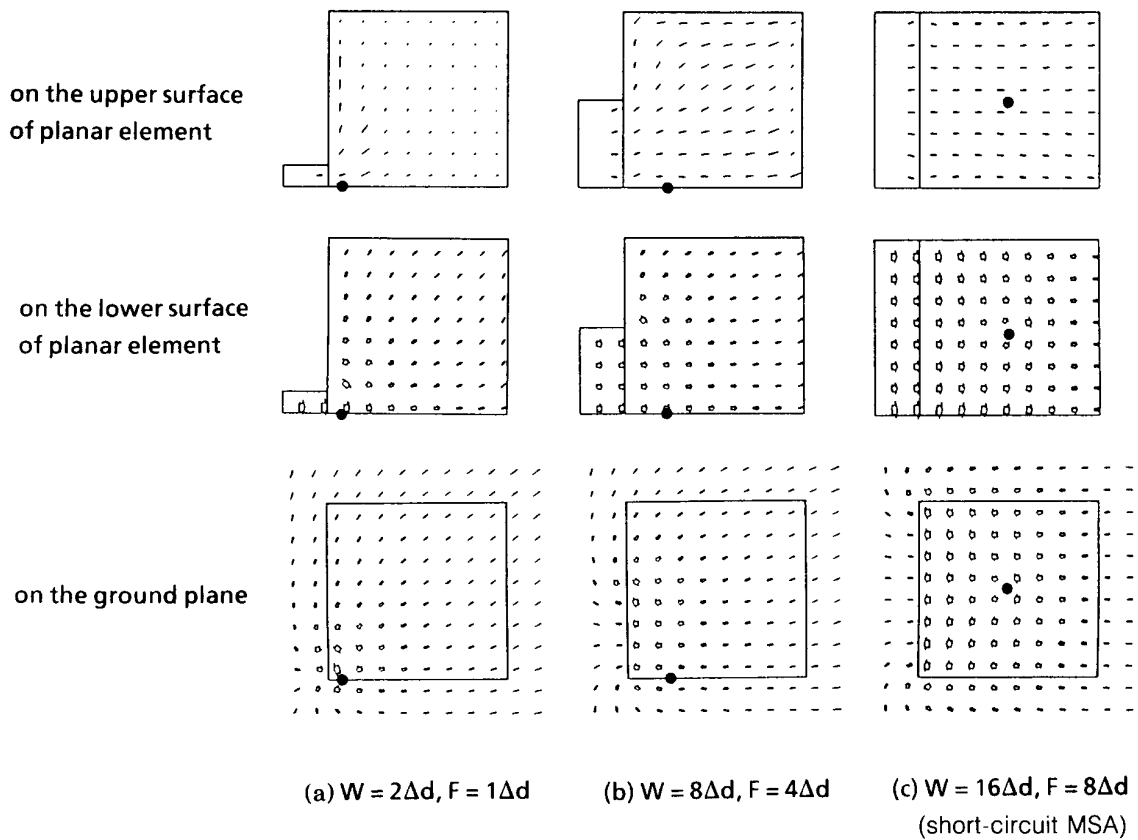


**Figure 2-15.** Surface current distribution on the PIFA of Fig. 2-12 for  $L_1=L_2$ . The black dot shows the feeding point. [8].

### 2.3.4. Resonant Frequency

As mentioned previously, the resonant frequency depends on the width of the short-circuit plate. To see this effect, simulations were performed by [8] on a PIFA for various short-circuit plate widths,  $W$ . Figure. 2-16 shows resonant frequency versus the short-circuit width  $W$  for a PIFA with the following dimensions:  $L_1=L_2=16\Delta d$ ,  $H=2\Delta d$ ,  $\Delta d=4$  mm. Note that the frequency  $f_1$  is the resonant frequency when  $W=L_1$ . As predicted, the resonant frequency  $f_r$  decreases as the width is decreased. From these results, one may quantitatively determine that the size of the PIFA can be reduced beyond that of the short-circuit MSA.

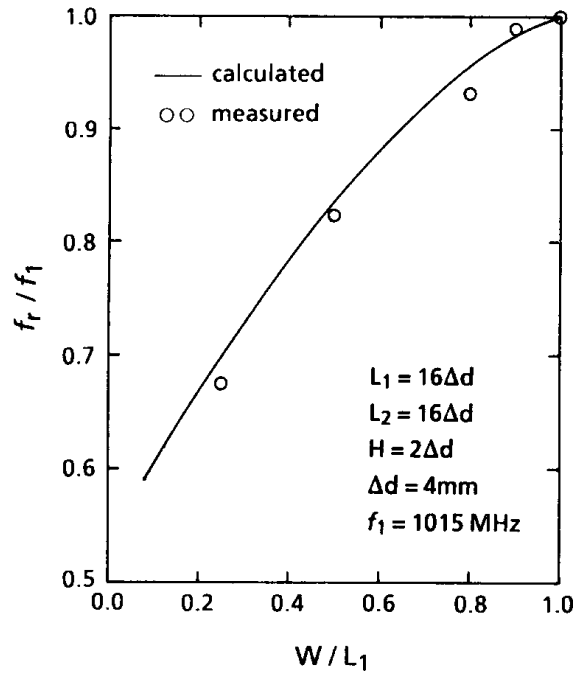


**Figure 2-16.** Normalized resonant frequency versus normalized shorting plate width  $W$  for PIFA in Fig. 2-12.  $f_1$  is the resonant frequency for PIFA with dimensions  $W=L_1$ . Data were computed using SNM [8].

The PIFA resonant frequency  $f_r$  is also influenced by the size ratio of the planar element,  $L_1/L_2$ . The ratio of resonant frequency,  $f_r$ , to the resonant frequency,  $f_1$ , is shown

in Fig. 2-17 as a function of shorting plate width for various values of top plate width  $L_1$ , while the other parameters  $L_2$  and  $H$  remain fixed,  $16\Delta d$  and  $2\Delta d$ , respectively, with  $\Delta d = 4$  mm. For this simulation, the PIFA is tuned to a resonant frequency of 1 GHz with  $W/L_1 = 1.0$ . This plot shows that as the plate width  $L_1$  increases (as measured by  $L_1/L_2$ ) the resonant frequency decreases, i.e.,  $f_r/f_1$  decreases, for a fixed  $W$ . Another noticeable behavior in the plot is that there is an inflection point in the resonant frequency curves for  $L_1/L_2$  greater than 1.0. This inflection point occurs at  $L_1 - W = L_2$  [8]. This behavior can be explained by examining the current direction in Fig. 2-18 on the surface underneath the planar element. The current flows mainly from the short-circuit plate to the opposite open-circuited edge for the case when  $L_1 - W < L_2$ . However, the direction of the current changes when  $L_1 - W > L_2$  [8]. This affects the effective length of the current flow, as shown in Fig. 2-18.

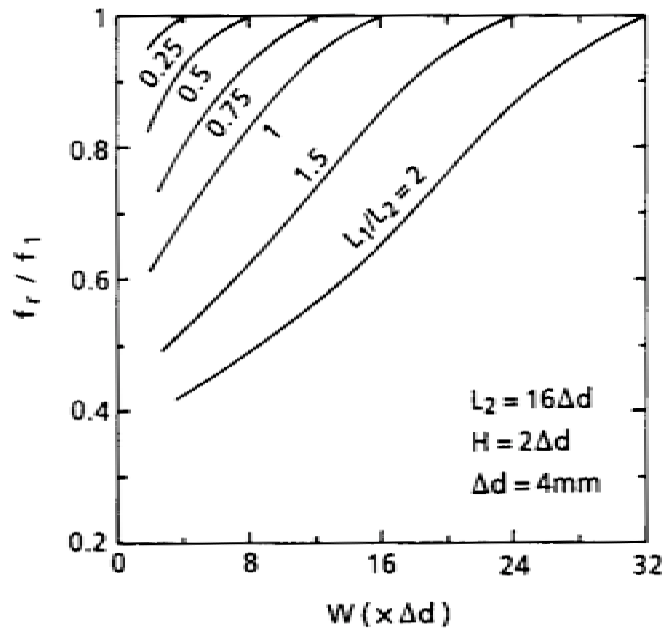


**Figure 2-17.** Normalized resonant frequency versus the width of short-circuit plate for various size ratio of the planar element. Results are calculated by [8].

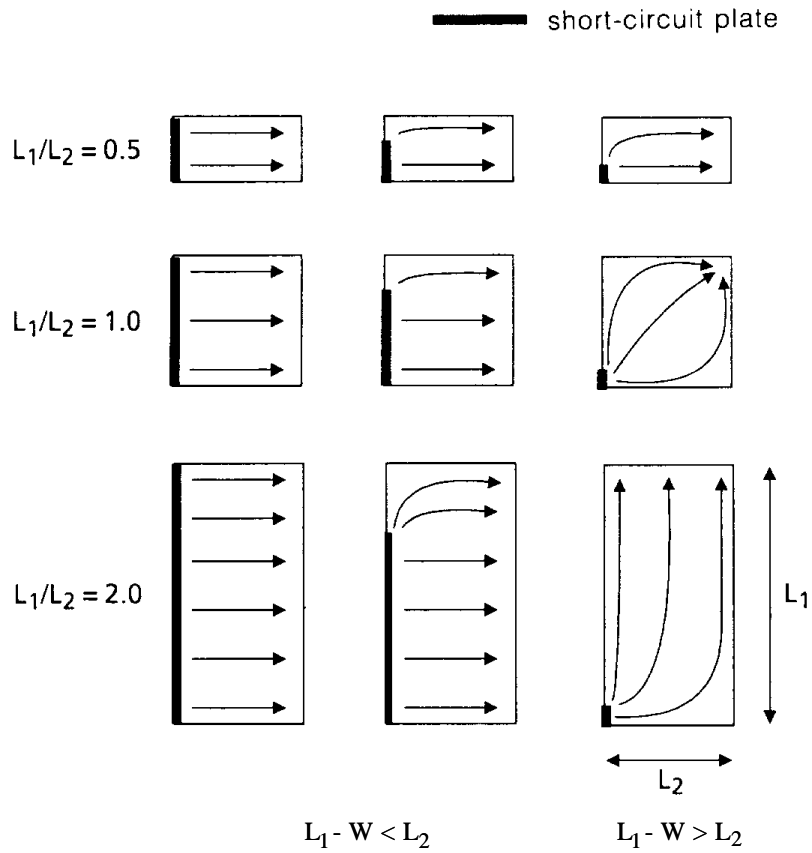


**Figure 2-18.** Variation of surface current flow underneath the planar element due to size ratio of planar element and width of short-circuit plate [8].

The resonant frequency of the PIFA is proportional to the effective length of the current distribution. There are two cases in which it is easy to formulate an expression of the resonant frequency with respect to the size of the PIFA. The first case is when the width of the short-circuit plate  $W$  is equal to the length of the planar element, say  $L_1$ . This corresponds to the case of the short-circuit MSA, which is a quarter-wavelength antenna; see Fig. 2-11(c). The effective length of the MSA is  $L_2 + H$  where  $H$  is the height of the short-circuit plate. The resonance condition then is expressed by

$$L_2 + H = \frac{\lambda_0}{4} \quad (2.2.1)$$

where  $\lambda_0$  is the wavelength. Resonant frequency associated with  $W=L_1$  calculated from (2.2.1) is

$$f_1 = \frac{c}{4(L_2 + H)} \quad (2.2.2)$$

where  $c$  is the speed of light. The other case is for  $W=0$ . A short-circuit plate with a width of zero can be physically represented by a thin short-circuit pin. The effective length of the current is then  $L_1+L_2+H$ . For this case, the resonance condition is expressed by

$$L_1 + L_2 + H = \frac{\lambda_0}{4} \quad (2.2.3)$$

The other resonant frequency that is part of the linear combination is associated with the case  $0 < W < L_1$  and is expressed as

$$f_2 = \frac{c}{4(L_1 + L_2 + H - W)} \quad (2.2.4)$$

For the case when  $0 < W/L_1 < 1$ , the resonant frequency  $f_r$  is a linear combination of the resonant frequencies associated with the limiting cases. The resonant frequency  $f_r$  is found using the experiment for  $f_1$  and  $f_2$  above in the following [8]:

$$f_r = r \cdot f_1 + (1-r) \cdot f_2 \quad \text{for } \frac{L_1}{L_2} \leq 1 \quad (2.2.5)$$

and

$$f_r = r^k \cdot f_1 + (1-r^k) \cdot f_2 \quad \text{for } \frac{L_1}{L_2} > 1 \quad (2.2.6)$$

where  $r = \frac{W}{L_1}$  and  $k = \frac{L_1}{L_2}$ . The above equations agree well with the measured results [8].

### 2.3.5. Bandwidth

The bandwidth of a PIFA depends on a few parameters, specifically the size ratio of the planar element  $L_1/L_2$ , the height of the short-circuit plate  $H$ , and the ratio  $W/L_1$ . Fig. 2-19 shows the dependency of the relative bandwidth for a  $VSWR \leq 1.5$  on relative height of the short-circuit plate  $H/\lambda_0$  for the width  $W$  of the short-circuit plate equal to  $L_1$ , corresponding to the short-circuit MSA. As illustrated in the figure, the bandwidth increases with the height of the short-circuit element and with the size ratio of the planar element  $L_1/L_2$ . The next figure, Fig. 2-20 shows the dependency of the bandwidth on the ratio  $W/L_1$  where the width of the short-circuit plate is shorter than that of the planar element  $L_1$ . Bandwidth decreases with the decrease of the short-circuit plate width. The dashed line represents the case for the short-circuit MSA.

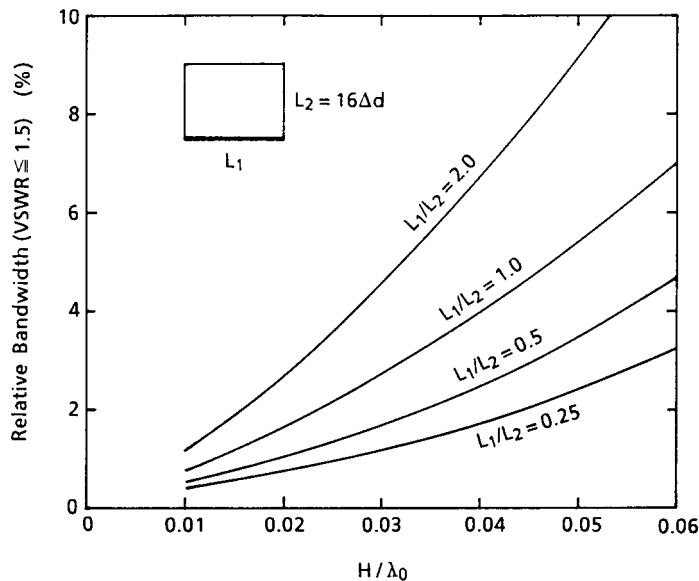


**Figure 2-19.** Computed bandwidth of the PIFA when short-circuit plate is equal to  $L_1$  (in the case of short-circuit MSA) [8].

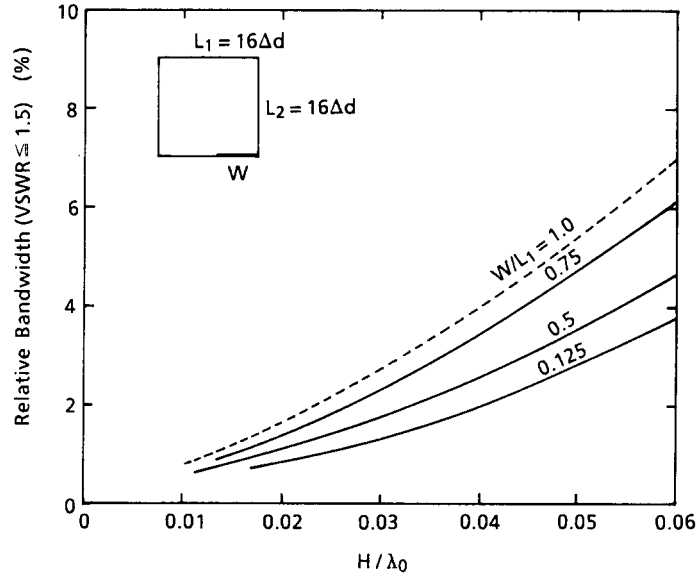


**Figure 2-20.** Computed Bandwidth of the PIFA when short-circuit plate width is narrower than  $L_1$  [8].

### 2.3.6. Design Procedure

The previous section presented the influence of the geometry parameters of the PIFA on its electrical performance based on numerical results. The resonant frequency of the antenna can be computed using equations (2.2.5) or (2.2.6).

With the help of Figs. 2-19 and 2-20, the size of the PIFA can be determined. As an example, consider the design of a PIFA for the cellular band (824-894 MHz) with a resonant frequency  $f_r=859$  MHz and a bandwidth of at least 70 MHz (8.14%). Using Fig. 2-19 for the case  $L_1/L_2 = 2.0$  with 8.2% for a  $VSWR \leq 1.5$ , one finds the height of the short-circuit element to be

$\frac{H}{\lambda_0} = 0.045$ , or  $H = 15.7$  mm for the resonant frequency  $f_r =$

859 MHz. This is the case when  $W = L_1$  and Equation (2.2.6) reduces to (2.2.2).  $L_2$  can then be computed from (2.2.2) and is equal to 71.6 mm. The other parameters are then  $W = L_1 = 143.2$  mm. In all case so far, the PIFA is assumed to be mounted on an infinite

ground plane. Figure. 2-21 shows the VSWR of the designed PIFA using the method of moments code IE3D [15]. The computed resonant frequency and impedance bandwidth are 865 MHz and 65 MHz (7.5%), respectively. This result shows that the procedure gives good results.

The PIFA design using the procedure illustrated above is not unique. One can find many cases in which the specifications are satisfied. Currently, a design procedure to optimize the size of a PIFA does not exist. A more thorough study of the parameters of the PIFA has to be performed to further characterize the antenna. Nonetheless, the general behavior of the PIFA is well understood with the results in the previous sections.

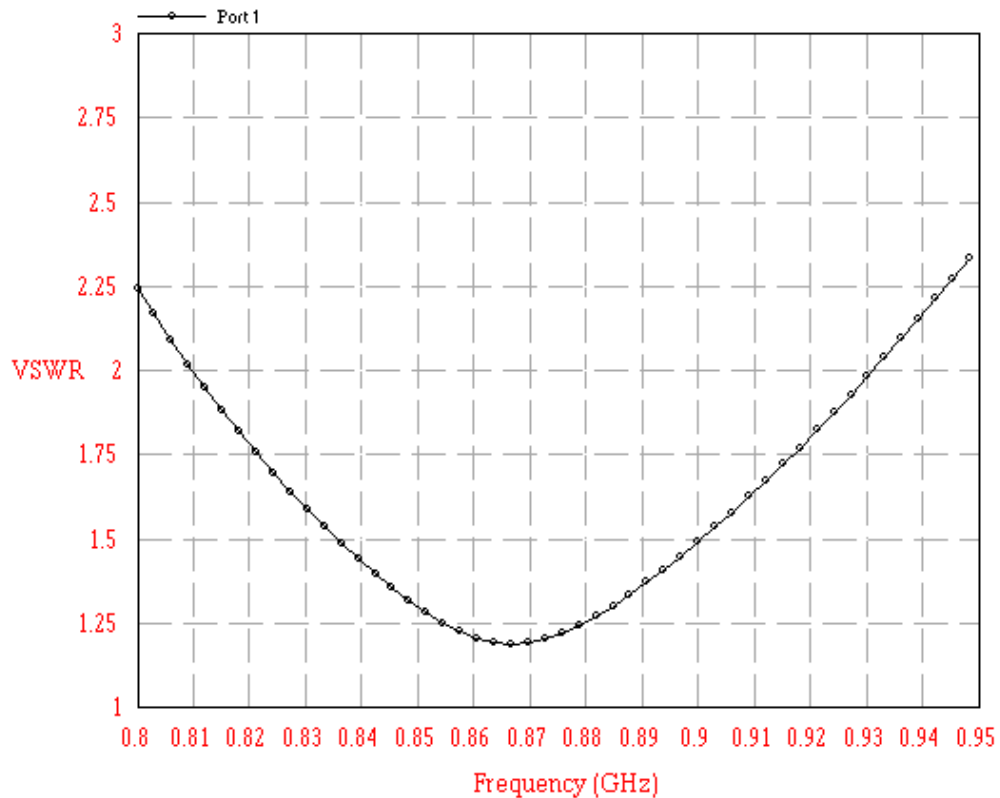


**Figure 2-21.** Computed VSWR for a PIFA operating in the Cellular band designed using the procedure mentioned in this section. It is computed using IE3D [13]. The dimensions of the PIFA are  $L_1=W=143.2$  mm,  $L_2=71.6$  mm,  $H=15.7$  mm.

### 2.3.7. Summary

The characteristics and geometry parameter influence of a PIFA on an infinite ground plane were presented in this chapter. In this analysis, the distributions of the electric fields between the planar element and the ground plane have been presented with respect to the short-circuit width. This result is useful in understanding the behavior of radiation characteristics in PIFAs. The surface current distribution was also examined. Also shown were the characteristics of the resonant frequency and bandwidth with respect to the size ratio of the planar element, short-circuit width, and antenna height.

## 2.4. References

- [1] J.R. James et al., *Microstrip Antenna Theory and Design*, Peter Peregrinus, New-York: 1981.
- [2] Y.T. Lo and S.W. Lee, *Antenna Handbook*, Van Nostrand Reinhold Company Inc., New-York: 1988.
- [3] N. Das, S.K. Chowdhury, and J.S. Chatterjee, "Circular Microstrip Antenna on Ferromagnetic Substrate," *IEEE Trans. Ant. Prop.*, vol. AP-31, no. 1, Jan. 1983, pp. 188-190.
- [4] Y. Suzuki and T. Chiba, "Designing Method on Microstrip Antennas Considering Bandwidth," *Trans. IECE of Japan*, vol. E67, Sept. 1984, pp.488-493.
- [5] Y.T. Lo, D. Solomon, "Theory and Experiment on Microstrip Antennas," *IEEE Trans. Ant. Prop.*, vol. AP-27, no. 2, March 1989, pp. 137-145.
- [6] A.G. Derneryd, "A Theoretical Investigation of the Rectangular Microstrip Antenna Element," *IEEE Trans. Ant. Prop.*, vol. AP-26, no.4, July 1978, pp. 532-535.
- [7] R.E. Munson, "Conformal Microstrip Antennas and Microstrip Phased Arrays," *IEEE Trans. Ant. Prop.*, vol. AP-22, no. 1, Jan. 1974, pp.74-78.
- [8] K. Hirisawa and M. Haneishi, *Analysis, Design, and Measurement of small and Low-Profile Antennas*, Artech House, Boston: 1992.

- [9] Y. Suzuki, "Key Point of Design and Measurement for Microstrip Antenna," Report of Tech. Group on Antennas and Propagation, *IECE of Japan*, no. AP89-S4, Nov. 1989.
- [10] R.W.P. King, C.W. Harrison, Jr., and D.H. Denton, "Transmission Line Missile Antennas," *IRE Trans. Ant. And Prop.*, vol. 8, no. 1, Jan. 1960, pp. 88-90.
- [11] T. Shibita, T. Hayashi, and T. Kimura, "Analysis of Microstrip Circuits Using Three-Dimensional Full Wave Electromagnetic Field Analysis in the Time Domain," *IEEE Trans. Microwave Theory and Technique*, vol. 36, no. 6, June 1988, pp. 1064-1070.
- [12] E. Yamashita, *Analysis Methods for Electromagnetic Wave Problem*, Artech House, Boston: 1990.
- [13] IE3D User's Manual, Zeland Software Inc., Release 5, 2000.
- [14] Y. Suzuki and T. Chiba, "Computer Analysis Method for Arbitrarily Shaped Microstrip Antenna with Multiterminals," *IEEE Trans. Ant. Prop.*, vol. AP-32, no. 6, June 1984, pp. 585-590.

# Chapter 3: Techniques for Widening the Bandwidth of Microstrip Antennas

## 3.1. Introduction

Antennas such as microstrip antennas and PIFAs have found many applications because of their low-profile and conformal geometry. Despite their many attractive features, however, narrow bandwidth often limits more widespread use.

The analysis of microstrip and planar inverted-F antennas were discussed in Chapter 2. A design procedure for each antenna type accounting for the bandwidth was illustrated. It was shown for both antenna types that bandwidth can be increased by increasing the height of the antenna. However, there are some limitations on how high the antenna can be. Current applications require the antenna volume to be small. Therefore, increasing the height of the antenna may not satisfy the size specifications for the required bandwidth. However, performance can be degraded when the height is increased. For instance, in the case of microstrip antennas, the increase in substrate thickness leads to excitation of surface waves which causes loss in radiation efficiency [1]. If a substrate is used in the microstrip antenna, one can increase the bandwidth by lowering its dielectric constant value. Figure 2-7 shows such a behavior for microstrip antennas where the unloaded  $Q$  is proportional to  $\epsilon_r$  and the bandwidth is inversely proportional to  $Q$ . However, increasing the bandwidth using this technique can cause some practicality issues such as increase in antenna cost.

A technique for improving the bandwidth of low-profile antennas that does not significantly increase the volume or degrade the performance is to use parasitic elements. Parasitic elements are designed to resonate close to the resonant frequency of the driven radiator element, leading to a desirable tuned response. The result is a wider effective

impedance bandwidth of the antenna. It is also called double-resonance phenomenon technique [2]. This chapter gives a brief analysis of antennas with double tuning showing a few configurations that have been widely used.

## 3.2. Numerical Analysis

There are numerous papers dealing with the analysis of the parasitic elements placed close to a driven antenna element. Both quasi-static and full-wave analyses have been reported. However, no simple and accurate design equations are available.

One approach to the analysis is to compute the capacitance that exists between the parasitic and the driven antenna elements. Consider the microstrip line geometry shown in Fig. 3-1. The capacitances can be expressed in terms of even and odd mode values for the two modes of propagation [3]. The distribution of the capacitances of the microstrip lines is shown in Fig. 3-2 for the two modes. The even-mode capacitance, shown in Fig. 3.2(a), can be divided into three types as

$$C_{even} = C_p + C_f + C_f' \quad (3.1)$$

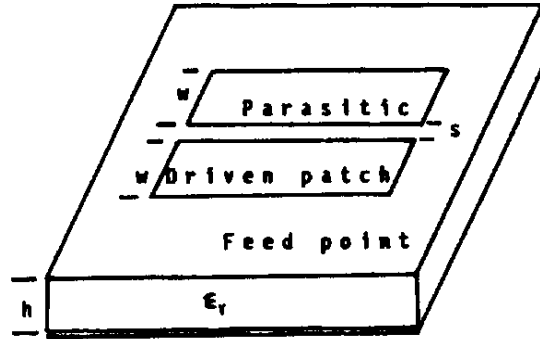
where  $C_p$  is the parallel plate capacitance between the strip and the ground plane,  $C_f$  is the fringing capacitance obtained from uncoupled microstrip line, and  $C_f'$  is the fringing capacitance due to the presence of another microstrip line. These capacitances are expressed by the following equations [3]:

$$C_p = \epsilon_0 \epsilon_r \frac{W}{H} \quad (3.2)$$

$$C_f = \frac{1}{2} \left[ \sqrt{\epsilon_{r,eff}} / cZ_0 - C_p \right] \quad (3.3)$$

$$C_f' = \frac{C_f}{1 + A \left( \frac{H}{S} \right) \tanh \left( 10 \frac{S}{H} \right)} \sqrt{\frac{\epsilon_r}{\epsilon_{r,eff}}} \quad (3.4)$$

where  $c$ ,  $\epsilon_{r,eff}$ , and  $Z_0$  are the speed of light in free space, the effective dielectric constant of the substrate, and the characteristics of impedance of the line, respectively.



Figures 3-1. Geometry of the rectangular patch antenna coupled with a parasitic element [3].

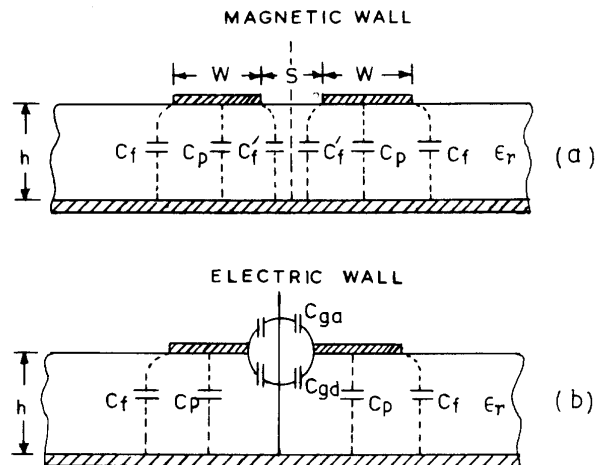


Figure 3-2. Distribution of capacitances of (a) even-mode and (b) odd-mode propagation. [3]

The expression for  $C_f'$  is obtained empirically such that the resulting value of even-mode capacitance is comparable with numerical results. The value  $A$  in the expression (3.4) for  $C_f'$  is given by [3]

$$A = \exp[-0.1 \exp(2.33 - 2.53W / H)] \quad (3.5)$$

The odd-mode capacitance, shown in Fig. 3.2(b) is expressed by [3]

$$C_{odd} = C_p + C_f + C_{gd} + C_{ga} \quad (3.6)$$

where  $C_{ga}$  and  $C_{gd}$  are the capacitances for the fringing fields across the gap in the air region and in the substrate region, respectively. They are computed from the following equations [3]:

$$C_{ga} = \varepsilon_0 \frac{K(k')}{K(k)}, \quad k = \frac{S/H}{S/H + 2W/H} \quad \text{and} \quad k' = \sqrt{1 - k^2} \quad (3.7)$$

$$C_{gd} = \frac{\varepsilon_0 \varepsilon_r}{\pi} \ln \left[ \coth \left( \frac{\pi S}{4H} \right) \right] + 0.65 C_f \left[ \frac{0.02}{S/H} \sqrt{\varepsilon_r} + 1 - \frac{1}{\varepsilon_r^2} \right] \quad (3.8)$$

where the ratio of the complete elliptic function  $K(k)$  and its complement  $K(k')$  is given

$$\frac{K(k)}{K(k')} = \begin{cases} \frac{1}{\pi} \ln \left[ 2 \frac{1 + \sqrt{k'}}{1 - \sqrt{k'}} \right] & 0 \leq k^2 \leq 0.5 \\ \frac{\pi}{\ln \left[ 2 \frac{1 + \sqrt{k}}{1 - \sqrt{k}} \right]} & 0.5 \leq k^2 \leq 1 \end{cases} \quad (3.9)$$

When the widths of the two microstrip lines differ, as shown in Fig. 3-3, the even-mode and the odd-mode capacitances (3.1) and (3.6) are modified because the asymmetry of the structure gives rise to different propagation characteristics to the lines. In this case, there are four impedances corresponding to two modes on two different lines. The following expressions are the modified version of the even- and odd-mode capacitances accounting this asymmetry [3]:

$$C_{even,i} = C_{pi} + C_{fi} + C'_{fi} \quad (3.10)$$

$$C_{odd,i} = C_{pi} + C_{fi} + C_{gd} \left| \frac{W_1+W_2}{2} \right. + C_{ga} \left| \frac{W_1+W_2}{2} \right. \quad (3.11)$$

where  $i=1, 2$  mean that the corresponding capacitance expression should be evaluated at the strip width  $W_1$  and  $W_2$ . The coupling capacitances  $C_{ga}$  and  $C_{gd}$  are evaluated using the mean value of the strip widths. Values computed from these expressions are close to the numerical results [3].

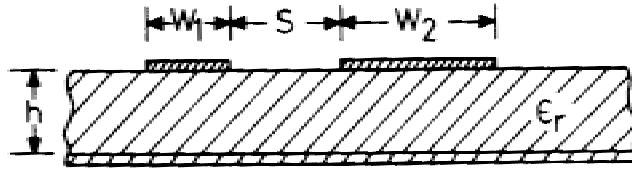


**Figure 3-3.** Configuration for asymmetric coupled microstrip lines.

Once the capacitances are known, the impedances for the even and odd modes are computed separately using the cavity model as previously discussed. The resultant input impedance of the system is given by

$$Z_{in} = Z_{in, even} + Z_{in, odd} \quad (3.12)$$

The impedance bandwidth is then found by computing the input impedance at each frequency.

Full-wave analysis can always be used to give accurate results using the integral equation technique [4]. Even though it is accurate, full-wave analysis does not give insight on the parasitic-element effect, as obtained with the capacitance-computation analysis. The next section illustrates several configurations of antennas using parasitic elements for widening the bandwidth.

### 3.3. Configurations

Probe-fed small antennas have bandwidth limits due to the inherent inductance introduced by the probe. The solution is to provide a mechanism to cancel out this probe inductance. One technique is to add parasitic elements. Indeed, the coupling between the driven structure and parasitic elements adds capacitance to the structure. The configuration of coupled parasitic element structure antennas can be classified into two categories: the parasitic element is either placed laterally or vertically to the main driven element. They are also called edge-coupled structure and capacitively fed structure, respectively.

#### 3.3.1. Edge-Coupling Structure Antennas

The antenna geometry shown in Fig. 3-4 represents a parasitic edge-coupled element microstrip antenna [5]. Various experiments were carried out in [5] to study the effect of gap-width on the performance this antenna structure. In initial experiments, theoretical impedance using the capacitance-calculation technique and experimental impedance do not match accurately. This discrepancy is attributed to the fact that this technique of computing the capacitances between the elements was derived from quasistatic calculations. Several values were changed in the expressions for the capacitances to match the experiments. Fig. 3-5 depicts the VSWR of the antenna with a thickness substrate of 0.159 cm, a dielectric constant  $\epsilon_r = 2.2$ , and  $L_1=L_2$  slightly different than  $L$ . The bandwidth of the antenna is 225 MHz (6.9%) at  $f_0 = 3.27$  GHz. To further increase the bandwidth, the parasitic elements have unequal lengths ( $L_1 \neq L_2$ ). This produces a triple-resonance phenomenon and widens the bandwidth (10% at  $f_0 = 3.29$  GHz), as illustrated in Fig. 3-6. For comparison, a single-element rectangular patch microstrip antenna is analyzed at the corresponding resonant frequency and substrate specifications. The experimental bandwidth is found to be 65 MHz, or 2%.

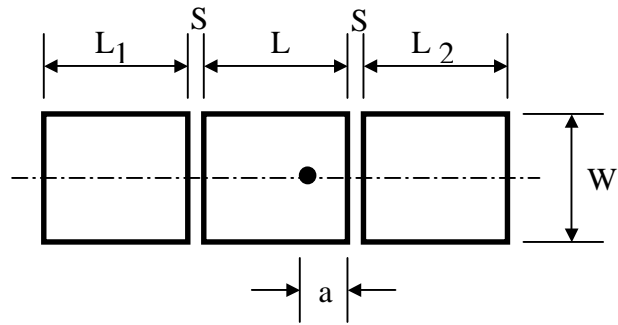


Figure 3-4. Antenna geometry of an MSA using edge-coupled parasitic elements.

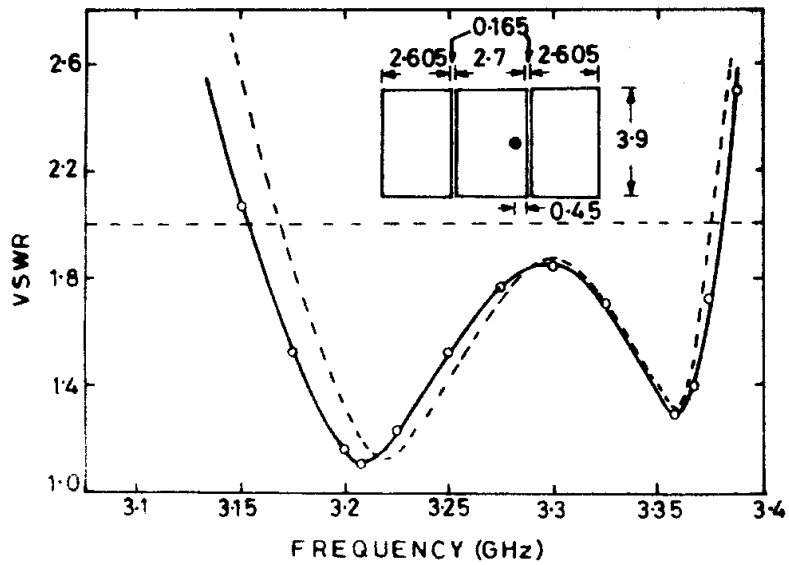
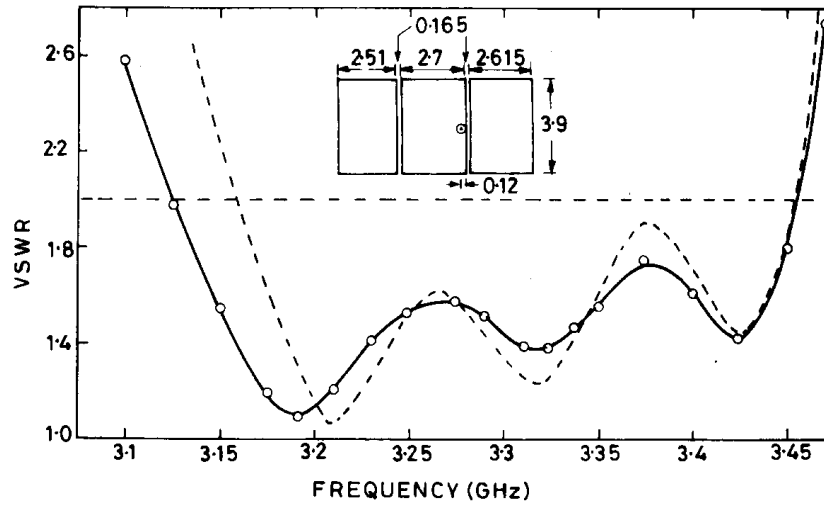


Figure 3-5. Theoretical (dashed curve) and experimental (solid curve) results for the VSWR. Theoretical values were calculated using Green's function approach and the segmentation method [10].



**Figure 3-6.** Theoretical (dashed curve) and experimental (solid curve) results for the VSWR for the MSA with unequal-length parasitic elements. Theoretical values were calculated using Green's function approach and the segmentation method [10].

### 3.3.2. Capacitively-Fed Structure Antennas

There have been numerous reports on using feeding techniques other than probe feeding in low-profile antennas. The capacitively feed technique has been a topic of recent interest. In the open literature, this technique has different names such as non-contacting feed or stacked-plate arrangement, but they all describe the same phenomenon of coupling between two elements in the structure. Such a technique is widely used with microstrip antennas (MSA). The configuration of a stacked MSA—or equivalently, capacitively fed MSA—is shown in Fig. 3-7. It consists of a ground plane, a radiating patch, and a patch located between the ground plane and the radiating patch. The middle patch is probe-fed. The advantage of this configuration over the edged-coupled structure is that the increase in volume is not significant or zero.

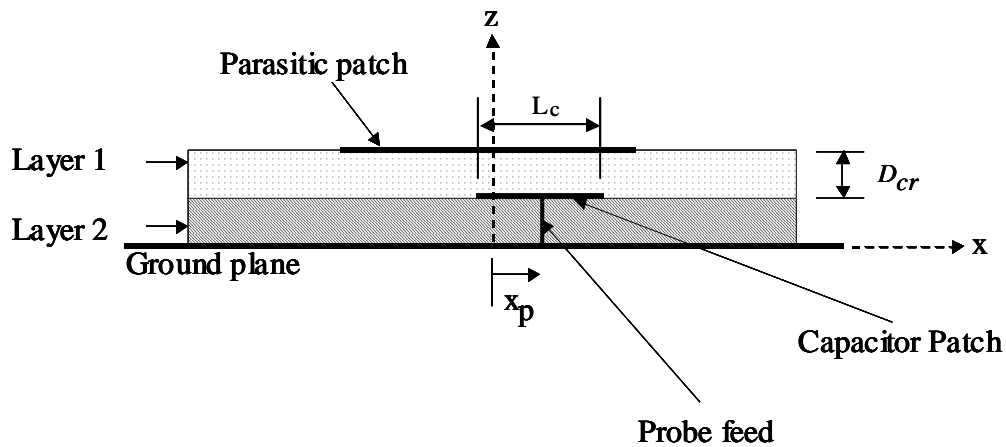


**Figure 3-7.** The capacitively fed microstrip antenna element.

A good parametric study of this antenna structure was performed in [8] using the method of moments to model the antenna. The structure has a square radiating patch with dimension 82.5 mm centered at the  $z$ -axis and 6.85 mm above a large ground plane, and a square capacitor patch located between the radiating patch and the ground plane. The antenna is probe-fed with 50-Ohm characteristic impedance, as shown in Fig. 3-7. The probe, positioned at  $(x_p, y_p) = (22 \text{ mm}, 0 \text{ mm})$ , is connected directly into the center of capacitor patch. The substrates in both layers have a dielectric constant  $\epsilon_r = 1$  (air). Figure 3-8 depicts the calculated and measured impedance and reflection coefficient of the antenna for a square capacitor patch with dimension  $L_c = 20 \text{ mm}$  and a distance  $D_{cr} = 2.15 \text{ mm}$  separating the capacitor and radiating patches. Numerical values were computed using the method of moments. Figure 3-8 shows that the measured and computed values are in good agreement. The resonant frequency is defined as the frequency at maximum resistance and the bandwidth as the band between the two frequency points where the amplitude of the reflection coefficient is  $-10 \text{ dB}$  ( $\text{VSWR} \leq 2$ ).

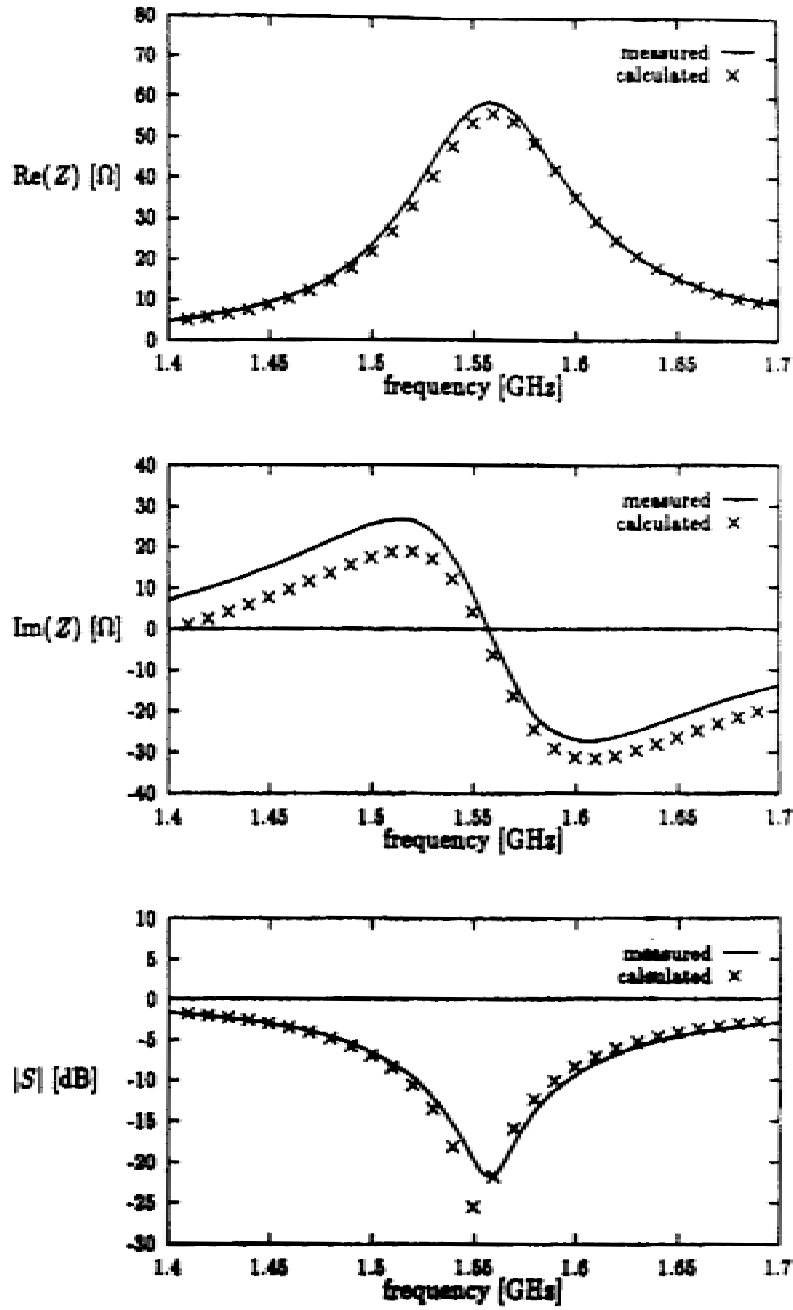


**Figure 3-8.** Impedance and reflection coefficient of a capacitively-fed microstrip antenna of Fig. 3-7 for a square capacitor patch with dimension  $L_c = 20$  mm and a distance  $D_{cr} = 2.15$  mm separating the capacitor and radiating patches [8]. Numerical values were computed using the method of moments.

Figure 3-9 shows the computed resonant frequency, resonant impedance, and bandwidth as a function of the capacitor patch size for a fixed position of the probe ( $x_p = 22$  mm) and for three distances  $D_{cr}$  between the radiating patch and the capacitor patch (1 mm, 3 mm, and 6 mm) using the method of moments. The plots show the following results: neither the size of the capacitor patch nor the distance between the radiator and capacitor patches significantly affects the resonant frequency and the bandwidth; the effect of the capacitor patch on the resonant impedance, however, is strong. The resonant resistance value drops considerably with increasing separation  $D_{cr}$ .

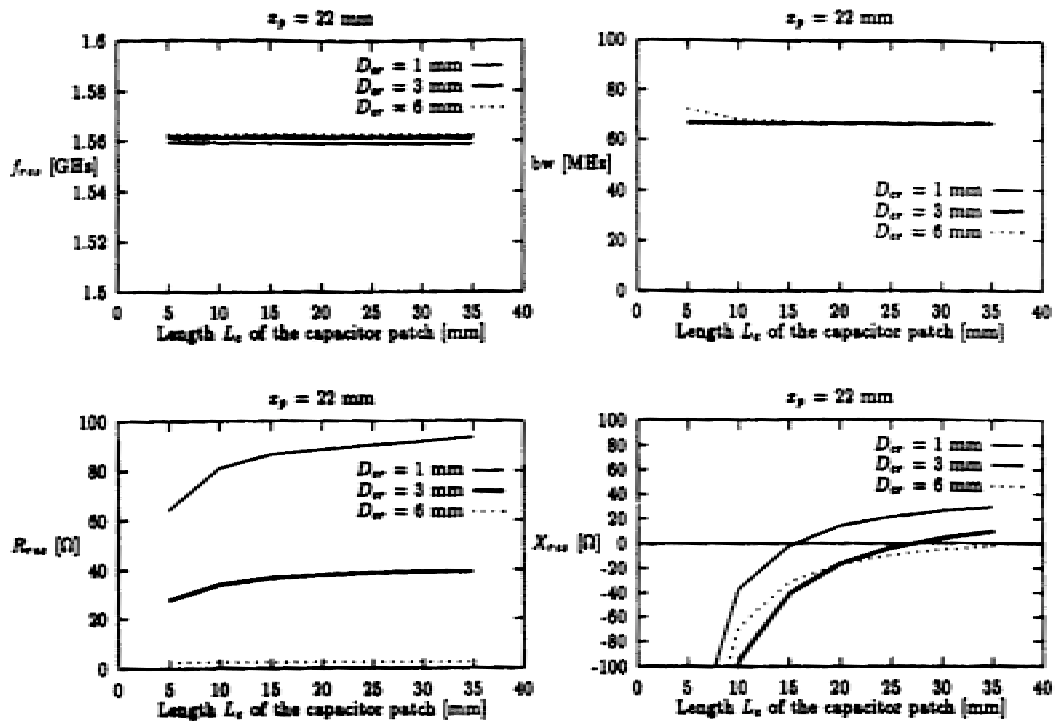
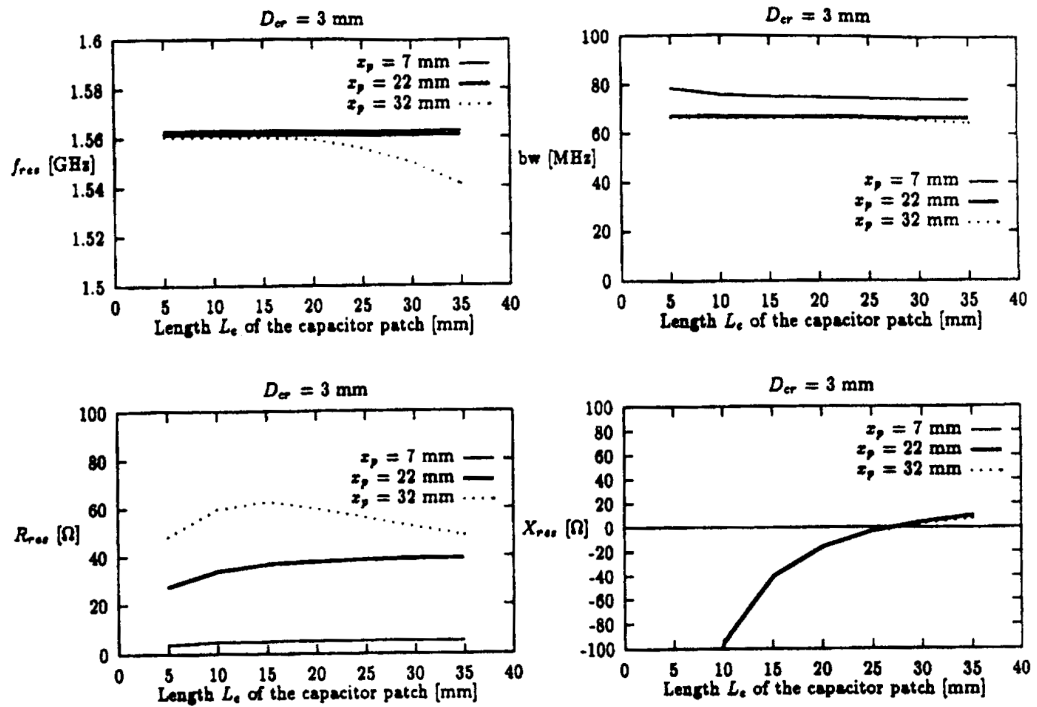


Figure 3-9. Resonant frequency, impedance, and bandwidth of a capacitively-fed microstrip antenna of Fig. 3-7 as a function of the size  $L_c$  of the capacitor patch for a fixed position of the probe  $x_p$ , and for three distances  $D_{cr}$  between the radiating and capacitor patch [8]. Numerical values were computed using the method of moments.



**Figure 3-10.** Resonant frequency, impedance, and bandwidth of a capacitively-fed microstrip antenna of Fig. 3-7 as a function of the capacitor patch size  $L_c$  for a fixed distance  $D_{cr}$  between the radiating and capacitor patches and for three position of the probe  $x_p$  [8]. Numerical values were computed using the method of moments.

In Fig. 3-10, the separation distance  $D_{cr}$  between the two patches of Fig. 3-7 remains fixed. The resonant frequency, impedance, and bandwidth are computed as a function of the capacitor patch size  $L_c$  for three positions of the probe  $x_p$  feeding in the center of the capacitor patch. From this figure, the following behavior can be concluded:

- (i) If the capacitor patch is sufficiently small, the effect of its size is negligible; it only affects the resonant frequency when the edge of the capacitor patch comes close or goes beyond the edge of the radiating patch (when  $L_c$  and  $D_{cr}$  large).
- (ii) If the probe feeding the center of the capacitor patch is located at a sufficient distance from the center of the radiating patch, the size of the capacitor patch does not affect the bandwidth of the antenna. If this distance reduced, the bandwidth increases.

- (iii) The resonant resistance increases with the size of the capacitor patch if its size is sufficiently small. Once the edge of the capacitor patch comes close or goes beyond the edge of the radiating patch, the resonant resistance starts decreasing with increasing the capacitor patch size.
- (iv) The position of the capacitor patch  $x_p$  does not affect the resonant reactance.

The behavior in (i) and (iii) can be explained by the fact that once the capacitor patch is no longer completely shielded by the radiating patch, it starts to radiate and the combination of both patches acts as a larger radiating patch, which lower the resonant frequency, as well as the resonant resistance.

Figure 3-10 depicts important results that can facilitate the design of a matched capacitively fed structure. It is seen, indeed, that for each patch separation, there exists a capacitor patch size for which the resonant reactance is zero, independent of the probe position. A design procedure for a matched capacitively fed microstrip antenna can be obtained from this property:

- 1- Design the basic microstrip antenna without the capacitor patch for the specified resonant frequency  $f_r$  and bandwidth;
- 2- Choose a patch separation  $D_{cr}$ ;
- 3- Determine the capacitor patch size for which the resonant reactance is zero;
- 4- Determine the position  $x_p$  of the probe feeding the center of the capacitor patch for which the resistance at  $f_r$  is  $50 \Omega$ .

It is important to keep in mind that the separation distance  $D_{cr}$  should not be chosen too large. Figure 3-9 showed that a large separation yields a large capacitor patch size for which the resonant reactance is zero and a small resonant resistance. A small resonant resistance may make the design impossible to match it to  $50 \Omega$ . Note also that

the last step introduces a small shift in resonant frequency. This can be corrected by modifying slightly the radiating patch size.

As far as the substrate of the two layers are concerned, it has been shown that thick, low dielectric constant laminates tend to give the largest bandwidth responses and good surface wave efficiencies [7]. It has been found that using higher dielectric constant substrate for the lower layer tends to give enhanced results. The thicker the lower layer, the greater the bandwidth. However, the thicker the lower layer, the less capacitive the impedance of the patch can become. Thus, if the lower substrate is too thick, when the parasitically coupled patch is positioned onto the configuration, the overall impedance trend will appear inductive and the impedance control and, hence, achievable bandwidth, will be limited.

The technique of capacitively feeding the microstrip antenna is a popular method for enhancing the impedance bandwidth. A structure of probe-fed stacked patches achieving a bandwidth of 25% was reported in [7]. Other variations of capacitively fed MSA can even reach a bandwidth of 30% [9]. Figure 3-11 illustrates several configurations of the structure. They are called short-circuit stacked MSAs. They are also considered as a variation of capacitively fed PIFAs.

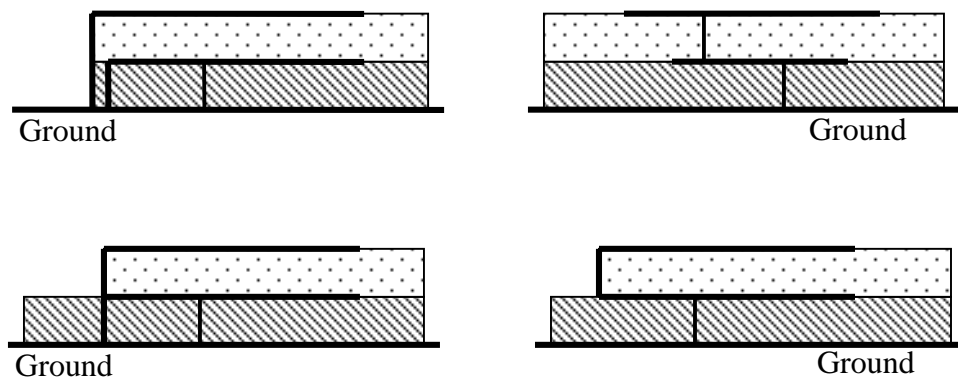


**Figure 3-11.** Variations of stacked patch antennas. They are also called short-circuit stacked MSA [11].

### 3.4. Summary

This chapter illustrated techniques of widening the bandwidth of low-profile antennas. The widely used technique consists of adding parasitic elements to the antenna structure. The technique is also called the double-resonance phenomenon technique. The analysis of this technique can be obtained using either quasi-static and full-wave integral equations method. It was pointed out that no accurate closed-form expression exists to do the analysis. The quasi-static method consists of computing the capacitances due the addition of parasitic elements. However, it only gives approximate results because of the complex computation of the capacitances. Nonetheless, this method shows some insights of how the structure behaves.

The coupled parasitic element structure can be classified into two categories: The edge-coupled configuration and the capacitively fed or stacked patch configuration. Each configuration was analyzed and the numerical results obtained gave some insights on how the structure behaves to facilitate the design procedure.

### 3.5. References

- [1] C.K. Aamandan, P. Mohanan, and K.G. Nair, "Broad-Band Gap Coupled Microstrip Antenna," *IEEE Trans. Ant. Prop.*, vol. AP-38, no. 10, Oct. 1990, p. 1581.
- [2] K. Hirisawa and M. Haneishi, *Analysis, Design, and Measurement of small and Low-Profile Antennas*, Artech House, Boston: 1992.
- [3] R. Garg, "Design Equations for Coupled Microstrip Lines," *Inst. J. Electronics*, vol. 47, no. 6, 1979, pp. 587-591.
- [4] J.R. Mosig and F.E. Gardiol, "The Effect of Parasitic Elements on Microstrip Antennas," *IEEE Ant. Prop. Soc. Int. Symp.*, Vancouver, Canada, June 1995, pp. 397-400.

- [5] G. Kumar and K.C. Gupta, "Broad-Band Microstrip Antenna Using Additional Resonators Gap-Coupled to the Radiating Edges," *IEEE Trans. Ant. Prop.*, vol. AP-32, no. 12, Dec. 1984, pp. 1375-1379.
- [6] B.L. Ooi and C.L. Lee, "Broadband Air-Filled Stacked U-Slot Shortened Patch Antenna," *Electronics Letters*, vol. 35, 1999, pp. 515-517.
- [7] R.B. Waterhouse, "Design of Probe-Fed Stacked Patches," *IEEE Trans. Ant. Prop.*, vol. AP-47, no. 12, Dec. 1999, pp. 1780-1784.
- [8] G.A.E. Vanderbosch and A.R. Van de Capelle, "Study of a Capacitively-Fed Microstrip Antenna Element," *IEEE Trans. Ant. Prop.*, vol. AP-42, no. 12, Dec. 1994, pp.1648-1652.
- [9] W.B. Waterhouse, "Broadband Stacked Shorted Patch," *Electronics Letters*, vol. 35, no. 2, Jan. 1999, pp. 98-100.
- [10] K.C. Gupta and P.C. Sharma, "Segmentation and Desegmentation Technique for Analysis of Planar Microstrip Antennas," *IEEE Ant. Prop. Soc. Int. Symp.*, Jun. 1981, pp. 19-22.
- [11] A.B. Smolders, *Microstrip Phased-Array Antennas: A Finite-Array Approach*, Thesis Report, Eindhoven University of Technology, 1994, Chapter 3.

# Chapter 4: Fundamental Limits on the Radiation $Q$ of Small Antennas

## 4.1. Introduction

Electrically small antennas are antennas with geometrical dimensions that are small compared to the wavelength of the radiated electromagnetic field. More specifically, the term “electrically small antenna” includes any antenna that fits inside a sphere of radius  $a = 1/k$  where  $k$  is the wave number associated with the electromagnetic field [1], the so-called radian sphere. The radiative properties of electrically small antennas were first investigated by Wheeler [2]. Later, using a very comprehensive theory, Chu [3] derived the minimum radiation quality factor  $Q$  of an antenna, that is enclosed inside a sphere of a given radius. In 1960, Harrington [4] extended Chu's theory to include circularly polarized antennas. Later, Collin [5] and Fante [6] derived exact expressions for the radiation based on the evanescent energy stored around an antenna. McLean [7] corrected an error in Chu's approximate expression and re-derived the exact expression using non-propagating energy. Most recently, Caswell [8] re-derived the fundamental limit on radiation  $Q$  using a time-domain approach.

This chapter reviews the work on the fundamental limit concept on the radiation  $Q$  of an antenna over the past decades. Chu, Harrington, MacLean, and Caswell's work is summarized to show the concept of the fundamental limit applied to practical small antennas.

## 4.2. Overview of Theoretical Investigations on the Fundamental Limits

Due to the importance of small antennas, there have been several theoretical investigations of antenna size and performance over the past five decades. Reducing

antenna volume generally degrades antenna performance. It is therefore important to examine the fundamental limits and parameter tradeoffs involved in size reduction. Certainly at some point performance specifications cannot be met if the allocated volume for the antenna region is reduced too much. It is well known that size reduction is obtained at the expense of bandwidth and efficiency. However, this must be quantified in order to have useful guidelines in the search for ways to produce more compact antennas.

The concept of Chu's work was to place an antenna inside a sphere of radius  $a$  that just enclosed the antenna and then to represent the fields outside the sphere as a weighted sum of spherical wave modes. Then radiation  $Q$  can be computed from [3]

$$Q = \begin{cases} \frac{2\omega W_e}{P_{rad}} & W_e > W_m \\ \frac{2\omega W_m}{P_{rad}} & W_m > W_e \end{cases} \quad (4.1)$$

where  $W_e$  and  $W_m$  are the time-average, nonpropagating, stored electric and magnetic energy, respectively,  $\omega$  denotes radian frequency, and  $P_{rad}$  denotes radiated power. Chu assumed that all of the stored energy is outside the sphere enclosing the antenna. This leads to the minimum possible radiation  $Q$  since any stored energy inside the sphere would increase the radiation  $Q$  of the antenna. However, the calculation of this radiation  $Q$  is not straightforward because the total time-average stored energy outside the sphere is infinite just as it is for any propagating wave or combination of propagating waves and nonpropagating fields [3]. Chu addressed this by deriving an RLC equivalent ladder network for each spherical waveguide mode and then radiation  $Q$  is computed from the stored energy in the inductors and capacitors of the equivalent circuit network. However, this is still a tedious computation if many modes exist. So, Chu approximated the system as an equivalent second-order series RLC network and solved the problem assuming that the antenna only excites the  $n = 1$  mode. The radiation  $Q$  expression then is

$$Q = \frac{1 + 2(ka)^2}{(ka)^3 [1 + (ka)^2]} \quad (4.2)$$

where the algebraic error cited by McLean [7] has been accounted for. Chu also showed that an antenna which excites only the  $n = 1$  mode has the lowest possible radiation  $Q$  of any linearly polarized antenna.

MacLean [7] re-examined this fundamental limit in order to achieve the highest possible accuracy because it makes little sense to speak of approximate fundamental limits. McLean then presented an exact expression for the minimum radiation  $Q$ . Like Chu, he assumed that the antenna radiates only one mode, in this case the  $n = 1$  spherical mode. The fields of this mode are equivalent to the fields radiated by a short dipole antenna. He computed the stored energy due to the total fields and then subtracts the stored energy due to the radiated fields, leaving only the non-propagating stored energy from which the radiation  $Q$  is determined. The resulting expression for  $Q$  is

$$Q = \frac{1}{(ka)^3} + \frac{1}{ka} \quad (4.3)$$

This relationship between the radiation  $Q$  and the antenna size represented by  $ka$  is plotted in Fig. 4-1. The family of curves includes the dependence of antenna radiation efficiency,  $e_r$ . The top curve is the plot of (4.3) and is for 100% radiation efficiency ( $e_r=1$ ). It shows that for small electrical sizes, say for  $ka < 1$ ,  $Q$  increases dramatically as size is reduced.

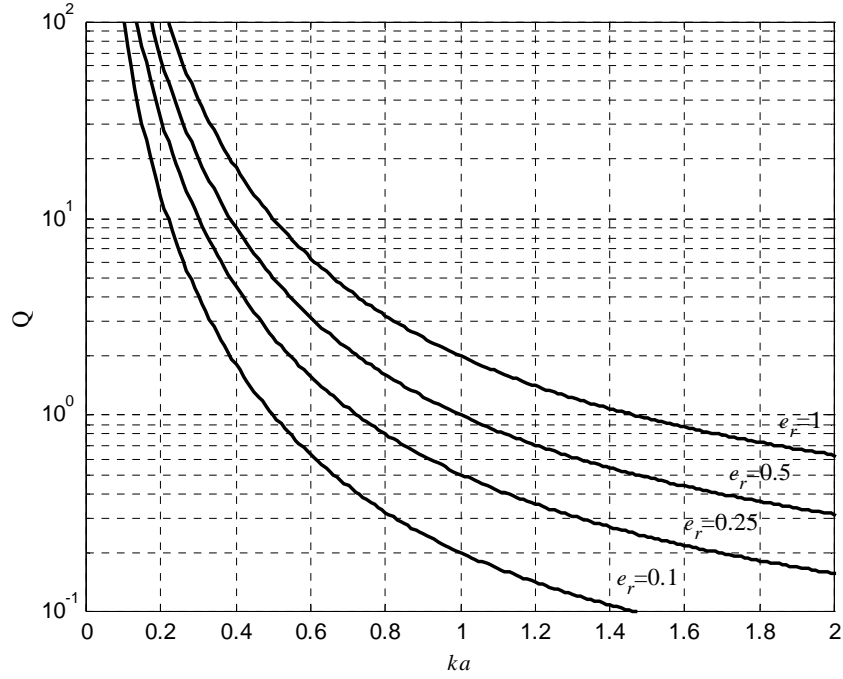


**Figure 4-1.** Fundamental limit curves of radiation  $Q$  versus  $ka$ . The top curve is a plot of (4.3) and is for efficiency,  $e_r = 1$ , or 100% .

Caswell [8] re-formulated the theory using the time-domain approach. The classical derivation of the fundamental limits assumed that the electric and magnetic stored energies are completely orthogonal. However, this is not the case for an antenna. For the time-domain derivation, the definition of  $Q$  given in (4.1) is modified as follows

$$Q = \frac{\omega \max[(W_e + W_m)]}{P_{rad}} \quad (4.4)$$

Computing the peak stored energy in the time domain assuming that the antenna radiates only one mode,  $n = 1$ , gives the final result for radiation  $Q$  [**limit 8**]:

$$Q = \frac{1}{2k^3 a^3} + \frac{1}{ka} + \sqrt{\frac{1}{4k^6 a^6} + \frac{1}{k^2 a^2}} \quad (4.5)$$

Figure 4-2 shows the minimum radiation  $Q$  of (4.3) as derived by MacLean compared to the  $Q$  in (4.5) for 100% efficiency. For small  $ka$ , both curves converge to the same value. However, as  $ka$  increases, the curves diverge. The commonly accepted size limit for small antennas is  $ka = 1$ . At the size, the ratio of the two curves is  $Q_{(4.5)}/Q_{(4.3)} = 1.31$ .

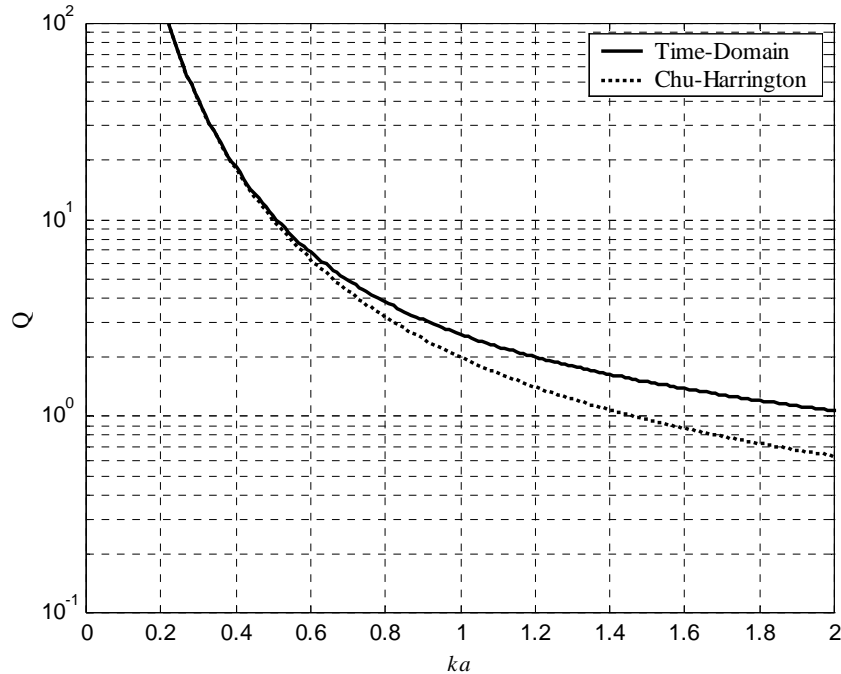


**Figure 4-2.** Comparison of the classical fundamental limit  $Q$  based on (4.3) versus the time-domain fundamental limit based on (4.5).

The family of fundamental limit curves in Fig. 4-1 can be explained as follows. A point for an antenna is located on the graph using the  $Q$  value for the antenna and its  $ka$  value at midband. The enclosing radius,  $a$ , of an antenna includes any images of the antenna in a ground plane. Realizable antennas have  $Q$  values above the curve corresponding to the efficiency of the antenna,  $e_r$ . That is, points corresponding to realizable antennas must lie above the curves. The curves are also used to find the size limit for a given bandwidth. For example, an antenna with 10% bandwidth ( $Q = 10$ ) and 100% efficiency must have  $ka > 0.5$ . This means  $a$  must be larger than  $0.08\lambda$ .

### 4.3. Comparison of Small Antennas

The fundamental limits presented in the previous section are based on theory and several assumptions are involved. It is therefore important to compare this theory to actual antennas in order to see if the fundamental limits are also useful for practical antennas. In this comparison, the time-domain fundamental limit curves based on (4.5) are used. The antennas used are found in the literature or are fabricated at the Virginia Tech Antenna Laboratory. Table 4-1 lists these antennas.

Bandwidth is an important parameter of interest for antennas and is related to the radiation quality factor  $Q$ . From a terminal standpoint the antenna can be viewed as a circuit device. Viewing the antenna as a resonant, parallel RLC circuit, fractional bandwidth is simply the inverse of  $Q$ ,

$$BW_{3dB} = 1/Q \quad (4.6)$$

$BW_{3dB}$  denotes the 3-dB bandwidth of the antenna and is defined as

$$BW_{3dB} = \frac{f_U - f_L}{f_c} \quad (4.7)$$

where  $f_U$  and  $f_L$  correspond to the upper and lower 3-dB points and  $f_c$  is the center frequency,  $f_c = (f_U + f_L)/2$ , of the frequency band of interest. The 3-dB point is where the signal is 3 dB below its peak value. Once bandwidth is determined,  $Q$  can be found from (4.6).

In practice, antenna bandwidth is often defined by  $VSWR = 2$ . Because  $Q$  is defined by the 3 dB points of the equivalent circuit model,  $Q$  is not just the inverse of the

VSWR = 2 bandwidth, as in (4.6). The relationship between Q and VSWR is determined as follows [9]:

$$Q = \frac{VSWR - 1}{BW_{VSWR} \sqrt{VSWR}} \quad (4.8)$$

For VSWR = 2, (4.7) reduces to

$$Q = \frac{1}{\sqrt{2} BW_{VSWR=2}} \quad (4.9)$$

Figure 4-3 shows the bandwidth-size performance values for the practical antennas listed in Table 4-1, along with the fundamental limit curve based on (4.5) for 100 % radiation efficiency. It is desirable for an antenna point to be as close to the desired efficiency curve as possible. A point that falls on the curve indicates that the antenna has achieved maximum bandwidth for its size. The example antennas shown in Fig. 4-3 represent a wide variety of antennas and none exceed the fundamental limits. Thus, we can conclude that the fundamental limits appear to provide realistic limits.

**Table 4-1**  
 Characteristics of antennas used to examine bandwidth-size relationships

Antenna	Radius of Enclosing Sphere ( $a$ )	Center Frequency ( $f_c$ )	Bandwidth ( $VSWR < 2$ )
$\lambda/2$ Dipole [10]	$\lambda/2$	300 MHz	36 MHz
Goubau [11]	$0.166\lambda$	300 MHz	75 MHz
IFA [12]	3.909 cm	923.5 MHz	17 MHz
DIFA [12]	3.926 cm	917 MHz	30 MHz
PIFA	3.774 cm	859 MHz	70 MHz
$\lambda/2$ Patch [1]	2.237 cm	3.03 GHz	32 MHz
Foursquare [13]	1.670 cm	6.0 GHz	2.12 GHz

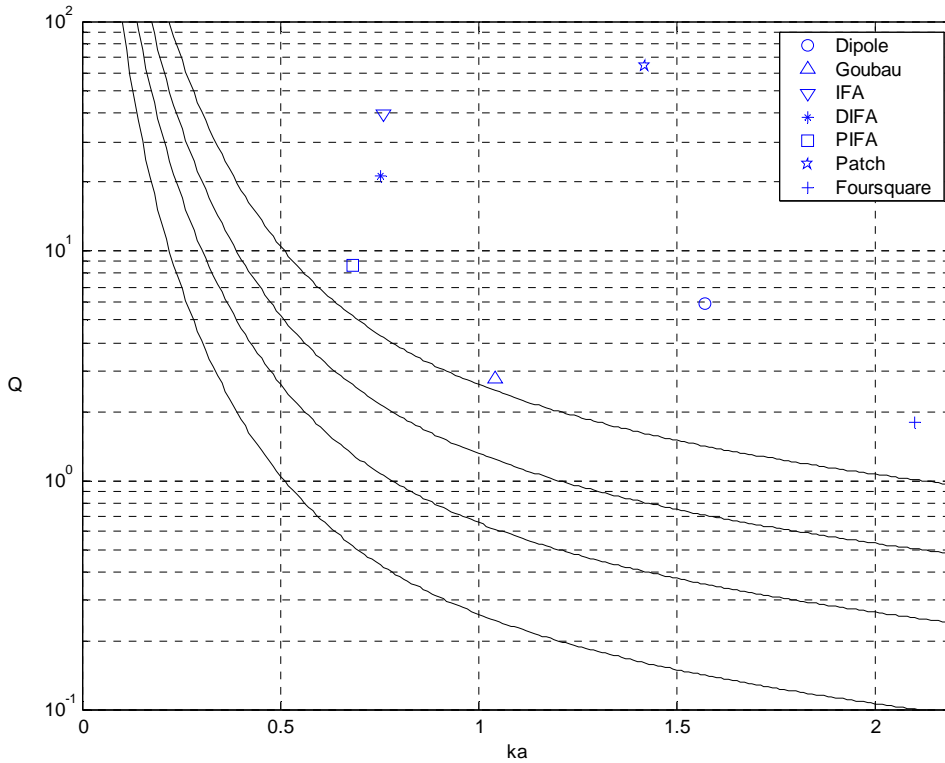


**Figure 4-3.** Comparison of several practical antenna ( $Q,ka$ ) values (see Table 4-1) to the fundamental limits curve based on the time-domain equation (4.5).

## 4.4. Summary

The classical theory of the fundamental limits on radiation  $Q$  based on Chu, Harrington, and MacLean's work and the time-domain approach from Caswell were

presented. Even though there was a small difference in two theories for large  $ka$ , the goal of this chapter to review and point out the concept of the fundamental limits on the radiation  $Q$  of small antennas. A few examples of practical antennas were illustrated on the fundamental limit curves to show that these curves provide realistic limits. Finally, the fundamental limits may be used as a guide for creating antenna specifications so that a search for unrealistic antenna can be avoided.

## 4.5. References

- [1] R.C. Hansen, "Fundamental Limitations in Antennas," *Proc. IEEE*, vol. 69, Feb. 1981, pp. 170-182.
- [2] H.A. Wheeler, "Fundamental Limitations of Small Antennas," *Proc. IRE*, vol. 35, Dec. 1947, pp. 1479-1484.
- [3] L.J. Chu, "Physical Limitations on Omni-Directional Antennas," *J. Appl. Phys.*, vol. 19, Dec. 1948, pp.1163-1175.
- [4] R.F. Harrington, "Effect of Antenna Size on Gain, Bandwidth, and Efficiency," *J. Res. Nat. Bur. Stand.*, vol64-D, Jan/Feb 1960, pp. 1-12.
- [5] R.E. Collin and S. Rothschild, "Evaluation of Antenna  $Q$ ," *IEEE Trans. Ant. Prop.*, vol. AP-12, Jan. 1964, pp.23-27.
- [6] R. Fante, "Quality Factor of General Ideal Antennas," *IEEE Trans. Ant. Prop.*, vol. AP-17, March. 1969, pp. 151-155.
- [7] J.S. Maclean, "A Re-Examination of the Fundamental Limits on the Radiation  $Q$  of Electrically Small Antennas," *IEEE Trans. Ant. Prop.*, vol. AP-44, no. 5, May 1996, pp. 672-676.
- [8] E.D. Caswell, W.A. Davis, and W.L. Stutzman, "Fundamental Limits on Antenna Size," Submitted to *IEEE Trans. Ant. Prop.*, April 2000.
- [9] K.R. Carver and J.W. Mink, "Microstrip Antenna Technology," *IEEE Trans. Ant. Prop.*, vol. AP-29, Jan. 1981, pp. 2-24.
- [10] W.L. Stutzman and G.A. Thiele, *Antenna Theory and Design*, 2<sup>nd</sup> Ed., Wiley, New-York: 1998.

- [11] R.C. Hansen, "Fundamental Limitations in Antennas," *Proc. IEEE*, vol. 69, Feb. 1981, pp. 170-182.
- [12] A.T. Gobien, *Investigation of Low-Profile Antenna Designs for Use in Hand-held Radios*, Antenna Group Report 97-4, August 1997.
- [13] C. Buxton, W.L. Stutzman, and R. Nealy, "Analysis of a New Wideband Printed Antenna Element – The Foursquare – Using FDTD Techniques," *IEEE Ant. Prop. Int. Symp.*, Atlanta, June 1998.

# Chapter 5: Ground Plane Effects on the Performance of the PIFA

## 5.1. Introduction

Studies of the effects of ground plane size on antenna performance are not new. The first investigations date back to the 1950s; see [5-10]. Most work focused on the characteristics of a monopole antenna mounted on a finite circular ground plane. Later, effects of the ground plane on other antenna types were studied, such as microstrip antennas [1-3]. Current applications require antennas to be mounted on small ground planes such as found in handheld communication devices. Models for antennas on a ground plane with infinite extent are not sufficiently accurate for such applications.

Investigations of the effects of ground plane size on planar inverted-F antennas have not been reported. Some work was performed on PIFAs mounted on a conducting box of fixed size [4]. However, none of the studies showed the antenna behavior as a function of conducting box size, or as a function of antenna position and orientation on a finite ground plane.

This chapter first discusses models available to analyze antennas on a ground plane with finite extent. Results from previous work will be shown to verify that these models are accurate. Then results from investigations on the performance of a conventional PIFA mounted on ground planes with various sizes and shapes will be discussed. Orientation and position of the antenna on a fixed-size ground plane will be analyzed as well. The purpose of this study is to illustrate the characteristics of the PIFA on a finite ground plane such as resonant frequency, bandwidth, gain, and radiation patterns. These illustrations are very useful in the design a PIFA for applications requiring a small ground plane. Specifically, the results reveal the tradeoff between PIFA geometry and ground plane size with electrical performance.

## 5.2. Theoretical Models

Several investigations have been reported for a monopole at the center of a conducting circular ground plane in free space. Experimental measurements of impedance were performed [5-7]. A few theories were used to model this problem including spheroidal functions, but the two mostly widely used techniques are the methods of moments and the geometrical theory of diffraction (GTD). They can also be combined to form a hybrid technique [6-8]. The philosophy behind this approach is to model only the antenna portion of the problem using the method of moments and then to model the finite three-dimensional body containing the antenna using the GTD method. In this way, the formal combination of these two useful computational methods result in the usual moment method impedance matrix being modified to properly account for the GTD contribution in the solution for the antenna current distribution.

For the idealized case of a ground plane of infinite extent, the antenna may be modeled by the method of images. However, for an antenna mounted on a ground plane of finite extent, the outer edge of the ground plane diffracts incident radiation in all directions and consequently currents on the ground plane and antenna differ from those for an infinite ground plane. At the outer edge of the ground plane, the currents on the top and bottom faces of the ground plane are equal in magnitude but opposite in direction because the net current must be zero at the edge. Outer edge diffraction becomes increasingly significant with decreasing size of the ground plane because of increasing magnitude of the currents on the ground plane faces at the outer edge. Edge diffraction can alter the input impedance by more than 100 percent and directive gain in the plane of the ground plane by more than 6 dB from the values for a ground plane of infinite extent [9]. The following discussion illustrates the accuracy of the models previously mentioned.

Richmond [10] developed a model of a monopole antenna mounted at the center of a circular disk using the sinusoidal-Galerkin moment method. The geometry is shown

in Fig. 5-1. Calculations using this method are then compared to the experimental measurements. Richmond assumes the wire representing the monopole to be a hollow tube and the circular disk ground plane with infinitesimal thickness rather than the thickness of the experimental device. Figure 5-2 illustrates the impedance of the monopole on a circular disk versus the disk radius. The computed values of impedance show satisfactory agreement with the measurements of Thiele and Newhouse [6]. Richmond's calculations are also compared to experimental measurements by Meier and Summers in 1949 [5], as shown in Fig. 5-3. Again, excellent agreement is apparent. Computations shown in this figure were performed using a monopole length  $h = 0.229 \lambda$ , which is slightly greater than the length  $h = 0.224 \lambda$  of the monopoles measured by Meier and Summers. The length  $h$  used in this model was adjusted to give best agreement with measured data.

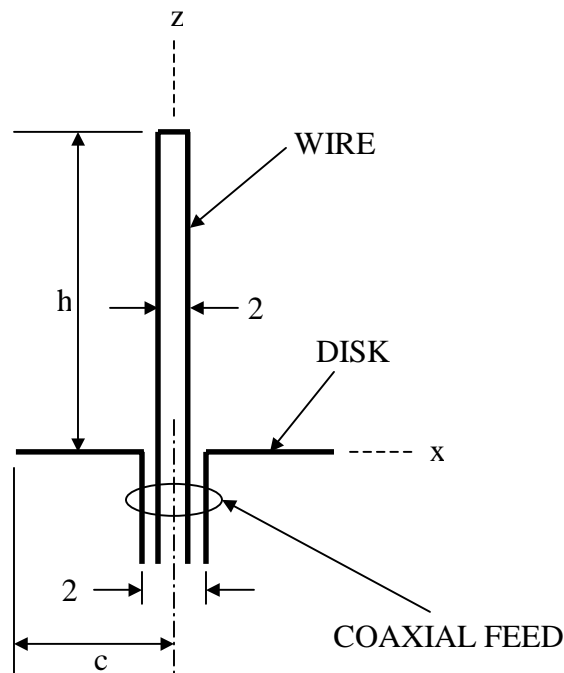


**Figure 5-1.** Cross sectional view of monopole fed via a coaxial cable through the center of a circular disk.

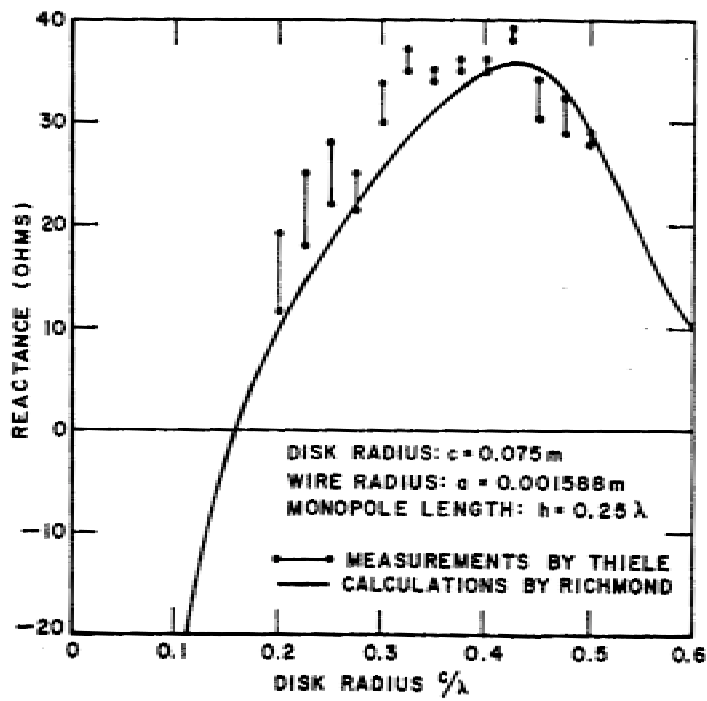
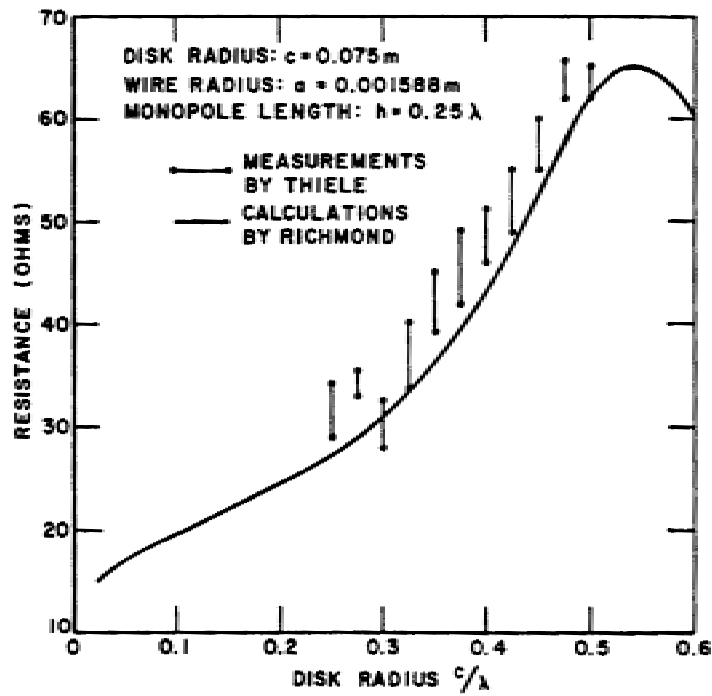


Figure 5-2. Resistance and reactance of monopole at center of circular disk in free space along with experimental measurements by Thiele and Newhouse [10].

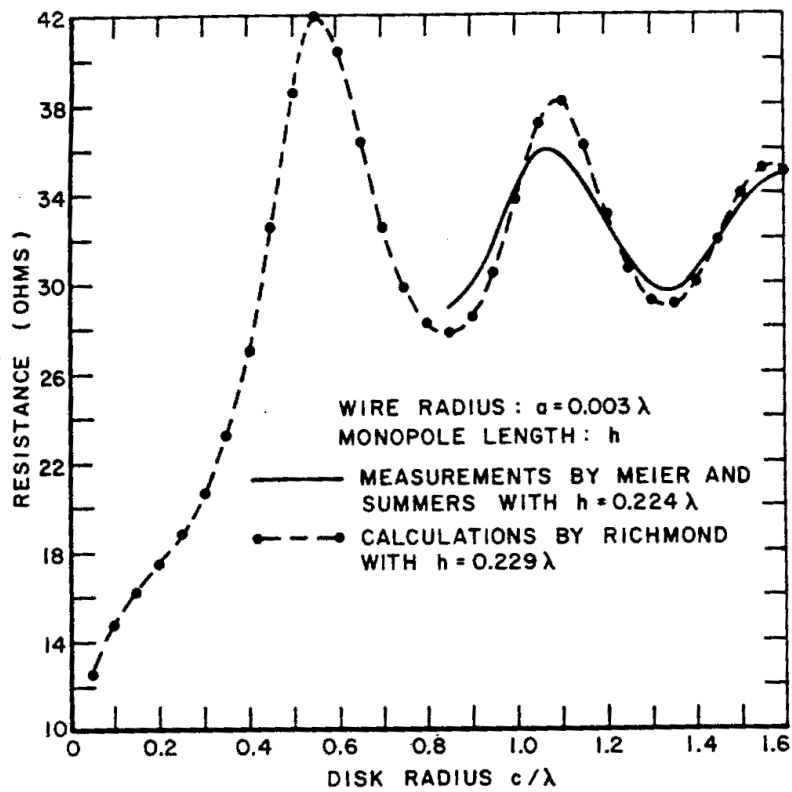


Fig. 7. Resistance of monopole at center of circular disk in free space.

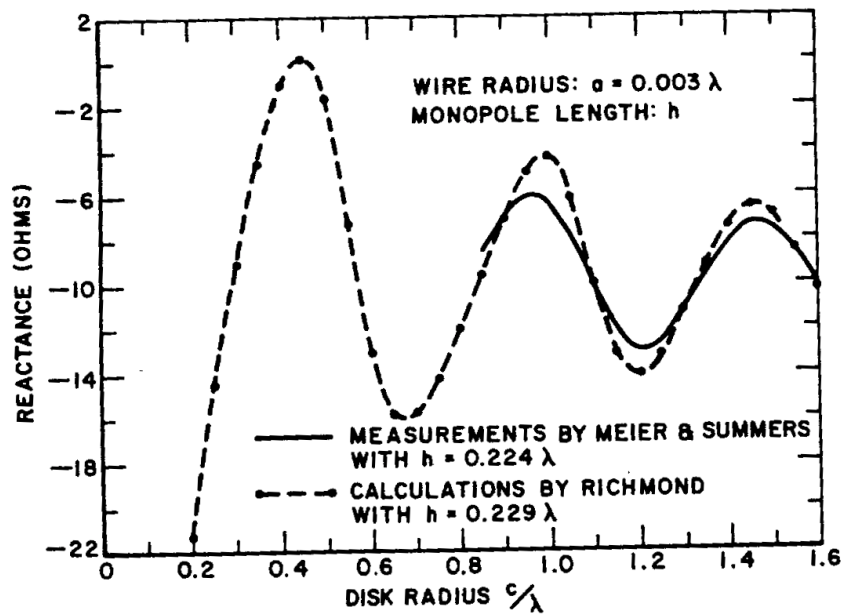
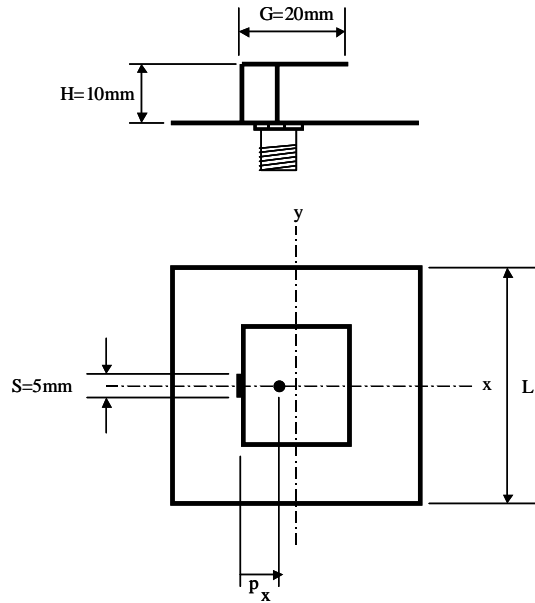


Figure 5-3. Resistance and reactance of monopole at center of circular disk in free space along with experimental measurements by Meier and Summers [10].

## 5.3. Finite Ground Plane Size Effects on the Conventional PIFA

### 5.3.1. Setup Description

This section presents results from extensive investigation using the method of moments into the effects of a finite ground plane on the performance of a PIFA. In addition, measurements were made to confirm computational results. The structure of a PIFA is shown in Fig. 5-4. It consists of a square conducting plate with dimensions 20 mm x 20 mm and a short-circuit plate with a 5-mm width and 10-mm height. These dimensions are selected to give a resonant frequency in the PCS band. They are fixed during all computations and measurements. Using the design procedure for PIFAs in section 2.3.6, the resonant frequency of the antenna is 1875 MHz for an infinite ground plane. At that frequency, the PIFA dimensions in terms of wavelength are  $G=0.125\lambda$ ,  $H=0.065\lambda$ , and  $S=0.03125\lambda$ . The PIFA is mounted at the center of a square ground plane with variable side length  $L$ . The following ground plane sizes  $L$  are used to measure the characteristics of the antenna: 20, 40, 60, 80, 100, 120, 140 mm. The metal used to construct the PIFA is brass. The conducting plate thickness used in the experiments is 0.381 mm. The PIFA is probe-fed using an SMA connector with probe radius of 0.635mm. The location of the probe is on the  $x$ -axis as shown in Fig. 5-4 and at a distance  $p_x$  from the shorting plate so that the antenna is matched to  $50 \Omega$  at resonance.



**Figure 5-4.** Geometry of the PIFA with a square conducting plate of  $G=20\text{mm}$  and a short-circuit plate whose width and height are  $S=5\text{mm}$  and  $H=10\text{mm}$ , respectively, mounted on a finite square ground plane with dimension  $L$ .

### 5.3.2. Numerical and Experimental Results

The software used to model the structure is IE3D from Zeland Software Inc. [11]. It is a method of moments electromagnetic simulator. The PIFA of Fig. 5-4 was evaluated using IE3D for each ground plane size  $L$ . The probe modeled in IE3D has a radius of  $0.635\text{mm}$  and is fed along the  $x$ -axis at the position  $p_x$  where the antenna is matched at resonance to  $50 \Omega$  at the port located on the ground plane. The SMA connector is not modeled in the structure. Resonant frequency, impedance bandwidth, location of the probe, and gain are recorded. Impedance bandwidth is defined as the frequency band between the lowest and the highest frequencies that have a 2:1 VSWR, and is calculated using

$$BW = \frac{f_u - f_l}{f_r} \times 100\% \quad (5.1)$$

where  $f_u$  and  $f_l$  are the upper and lower frequencies, respectively, that have a VSWR of 2, and  $f_r$  is the frequency with the lowest VSWR.

Impedance measurements was performed with the HP8720C Network Analyzer. The impedance was adjusted to account for the phase delay associated with the distance between the SMA connector and the location of the ground plane so that computed and measured results are at the same location. Numerical and experimental data are presented in Table 5-1. Representative results are shown in Figs. 5-5 and 5-6 for impedance characteristics of the PIFA with ground plane size of  $L = 80\text{mm}$ . From Fig. 5-6, it can be concluded that simulation yields a resonant frequency that is 2.62% below the measured value. The result shows excellent agreement between the numerical and experimental values, which gives confidence in the accuracy of the moment method computational model. Graphical representations of the data in Table 5-1 are presented in Figs. 5-7, 5-8, and 5-9 for the resonant frequency, bandwidth, and gain, respectively, with respect to the ground plane size in terms of wavelength.

**Table 5-1**  
Computed and Measured Values of the PIFA Characteristics for Various Ground plane sizes.

Square Ground plane size $L$ (mm)	Probe location $p_x$ (mm)	Resonant Frequency		Bandwidth for 2:1		Peak Gain (dBi)
		$f_r$ (MHz)		VSWR (MHz)		Computed
		Computed	Measured	Computed	Measured	
20	1.7	2343	2440	99	102	1.25
40	1.8	2013	1987	81	68	1.30
60	2.0	1956	1905	92	76	1.24
80	2.1	1943	1892	93	94	2.69
100	2.2	1928	1886	96	97	3.46
120	2.8	1950	1899	135	109	4.24
140	3.5	2015	1942	196	168	4.41
160	3.0	1991		151		4.10
180	3.0	1980		146		4.25
200	3.4	2015		182		4.95
infinite	2.9	1980		148		4.57

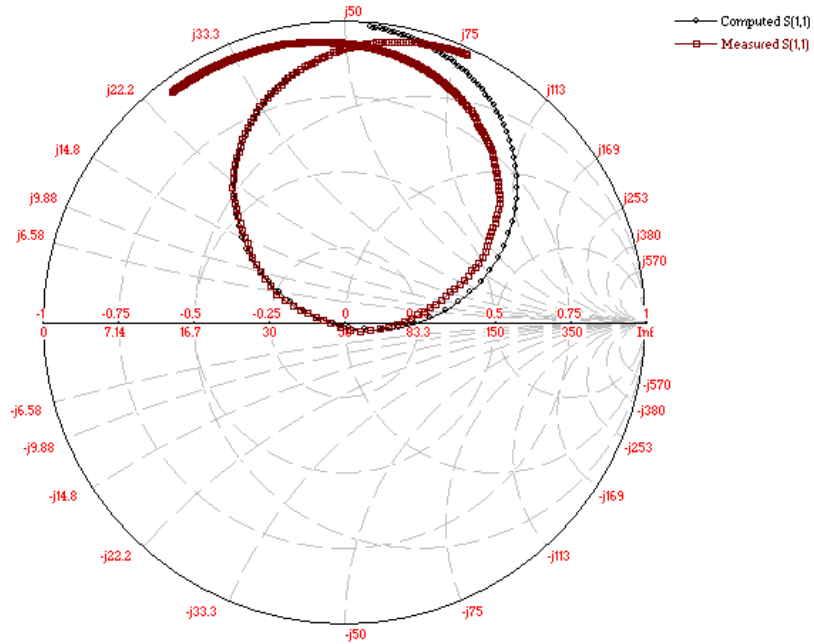


**Figure 5-5.** Smith chart displaying computed and measured impedance of a conventional PIFA shown in Fig. 5-4 mounted at the center of a square ground plane of 80-mm length and probe-fed at 2.1 mm away from the short-circuit plate.

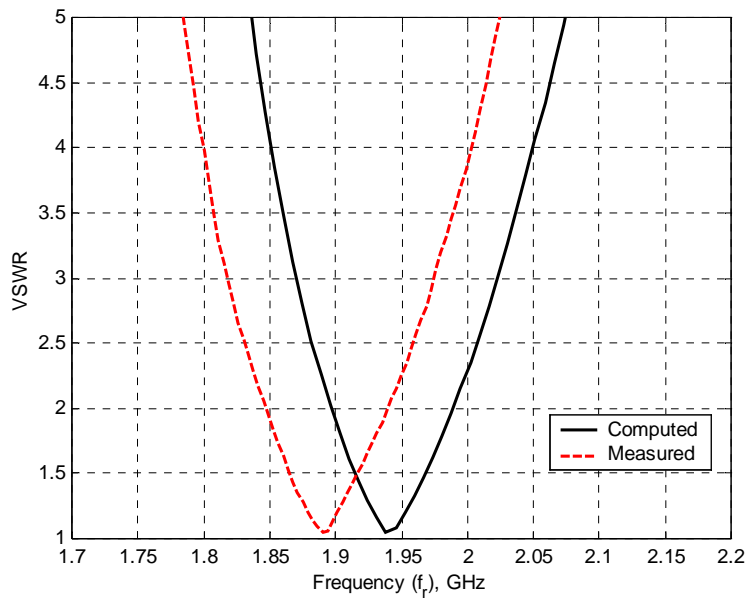


**Figure 5-6.** Computed and measured VSWR of a conventional PIFA shown in Fig. 5-4 mounted at the center of a square ground plane of 80-mm length and probe-fed at 2.1 mm away from the short-circuit plate.

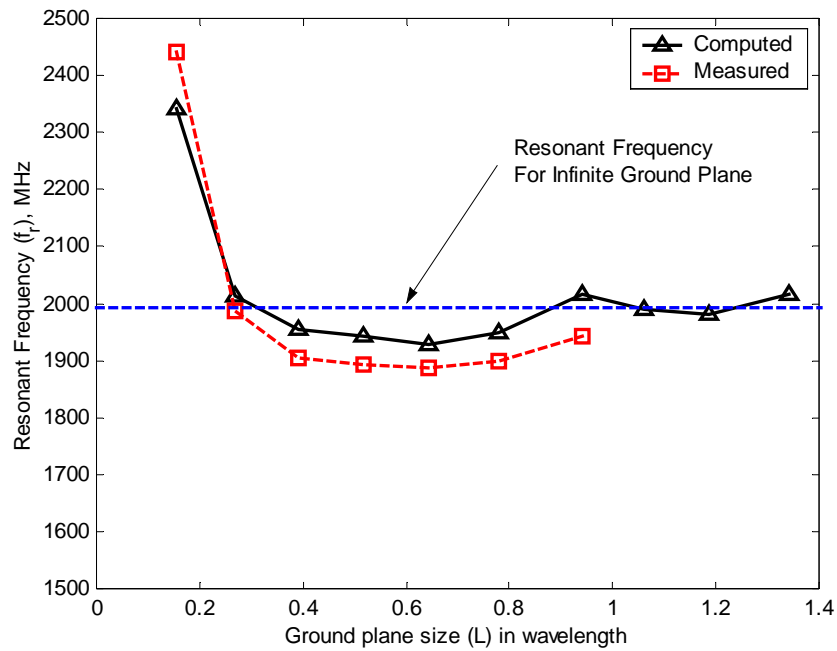


**Figure 5-7.** Computed and measured resonant frequency of a conventional PIFA for various square ground plane sizes in term of wavelength.

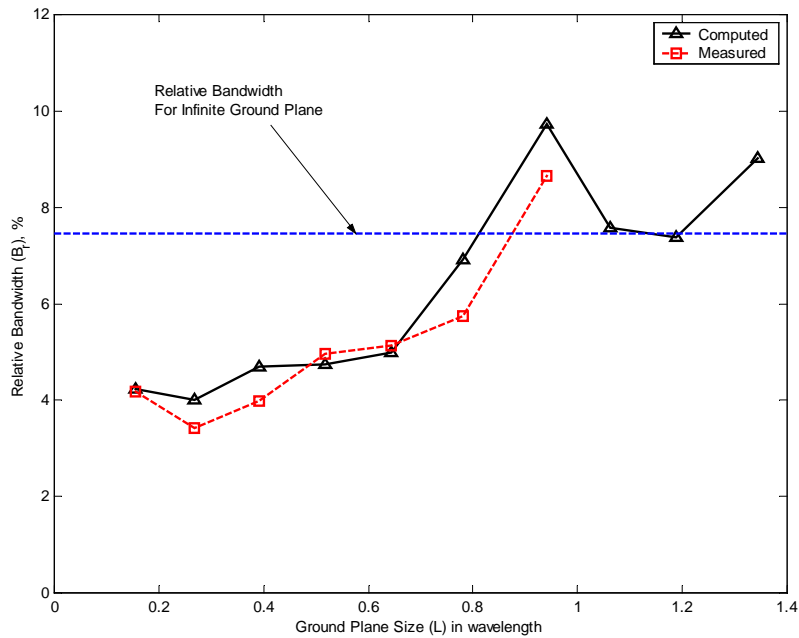


**Figure 5-8.** Computed and measured impedance bandwidth for 2:1 VSWR of a conventional PIFA for various square ground plane sizes in term of wavelength.

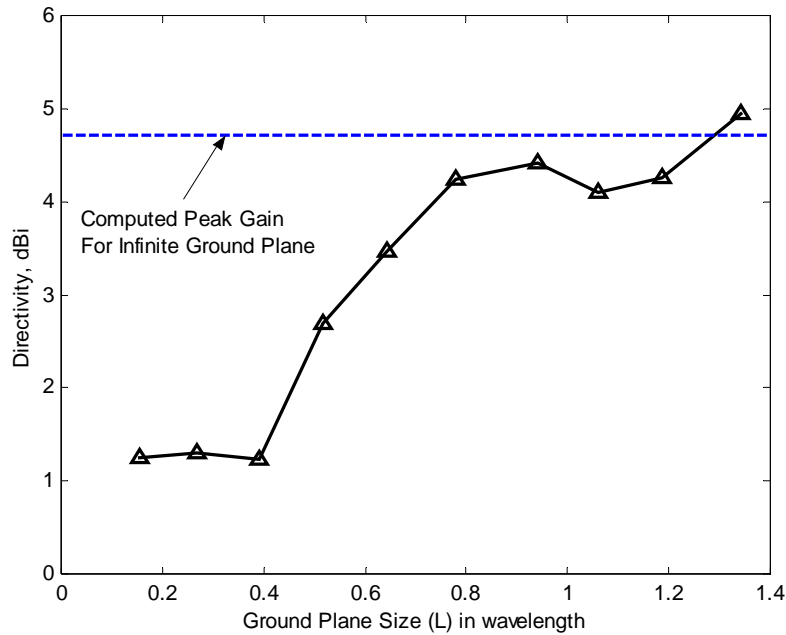


**Figure 5-9.** Computed peak gain of a conventional PIFA for various square ground plane sizes in term of wavelength.

Previous work from other authors [5-10] showed that the impedance of an antenna oscillates with ground plane size and converges toward a value as the ground plane size increases, as shown in Fig 5-3. Since resonant frequency and impedance bandwidth are related to the impedance of the antenna, they should have the same behavior; this is demonstrated in Figs. 5-7 and 5-8. In fact, the resonant frequency and bandwidth of the PIFA oscillate as the ground plane size increases and converges to the values for that the PIFA mounted on an infinite ground plane. From Fig. 5-7, the size of the PIFA ground plane has no significant influence on the resonant frequency unless the ground plane is reduced below about  $0.2\lambda$ . However, Fig. 5-8 shows that ground plane size has a strong influence on bandwidth. Popular wireless bands require about 8% bandwidth. This bandwidth is achieved by a square ground plane of at least  $L=0.8\lambda$ ; see Fig. 5-8. This relatively large ground plane size can be limiting factor in PIFA design.

The gain is affected strongly by the ground plane size as shown in Fig. 5-9. Rather than increasing uniformly with the ground plane size, the dependence is complex.

The gain is lowest when the ground plane size is comparable to the upper plate size of the PIFA. As the ground plane size increases, the peak gain increases and reaches a maximum at about  $L=0.9\lambda$ , for ground plane sizes less than one wavelength. The gain at that size is 4.45 dBi, which is close to the gain for an infinite ground plane. For most wireless handheld applications, 3-dBi gain is usually required. To achieve 3-dB gain, the ground plane size of a PIFA should be at least a half wavelength ( $L= 0.5 \lambda$ ); see Fig. 5-9.

Radiation patterns of the PIFA mounted at the center of each ground plane were computed at resonance to illustrate the radiation behavior. Patterns were also measured using the Virginia Tech indoor anechoic chamber for the PIFA mounted on the square plane of size  $L = 80 \text{ mm}$  ( $0.5 \lambda$ ). As indicated in Fig. 5-10, there is good agreement between measured patterns and IE3D simulations. This gives confidence in using IE3D to examine antenna parameter influences.

Figure 5-11 shows computed total  $E_\theta$  3-dimensional radiation patterns for each ground plane size. The figure shows that the direction of maximum radiation is significantly affected by ground plane size. As the ground plane increases in size, the back radiation ( $\theta=180^\circ$ ) becomes smaller and disappears when the ground plane size is infinite. Fig. 5-12 shows this change in direction of the PIFA maximum directivity in the x-z plane for a few ground plane sizes. For the infinite ground plane case and when the ground plane size is the same size as the PIFA upper plate, maximum directivity occurs at the horizon. For these two cases, the antenna acts like a short monopole and a short dipole, respectively, since it is known that power is radiated from the short-circuit plate element where the current is concentrated. For the other cases, the peak directivity varies from  $\theta=315^\circ$  to  $\theta=335^\circ$  for the ground plane size less than a wavelength.

An important effect of edge diffraction due to a finite ground plane is that high cross-polarization is introduced, as shown in Fig. 5-13. For the case of an infinite ground plane and when the ground plane size is the same as that of the upper plate, the PIFA polarization is purely linear in the  $\theta$ -direction, similar to a dipole, and no polarization appears in the  $\phi$ -direction. However, cross-polarization appears for other ground plane

sizes and can become significant, as illustrated in Fig 5-13. High cross-polarization can be useful for applications where the antenna is positioned randomly and its polarization may not be aligned with incoming signals. Applications such as for hand-held devices require linear polarization response in all directions for good performance.

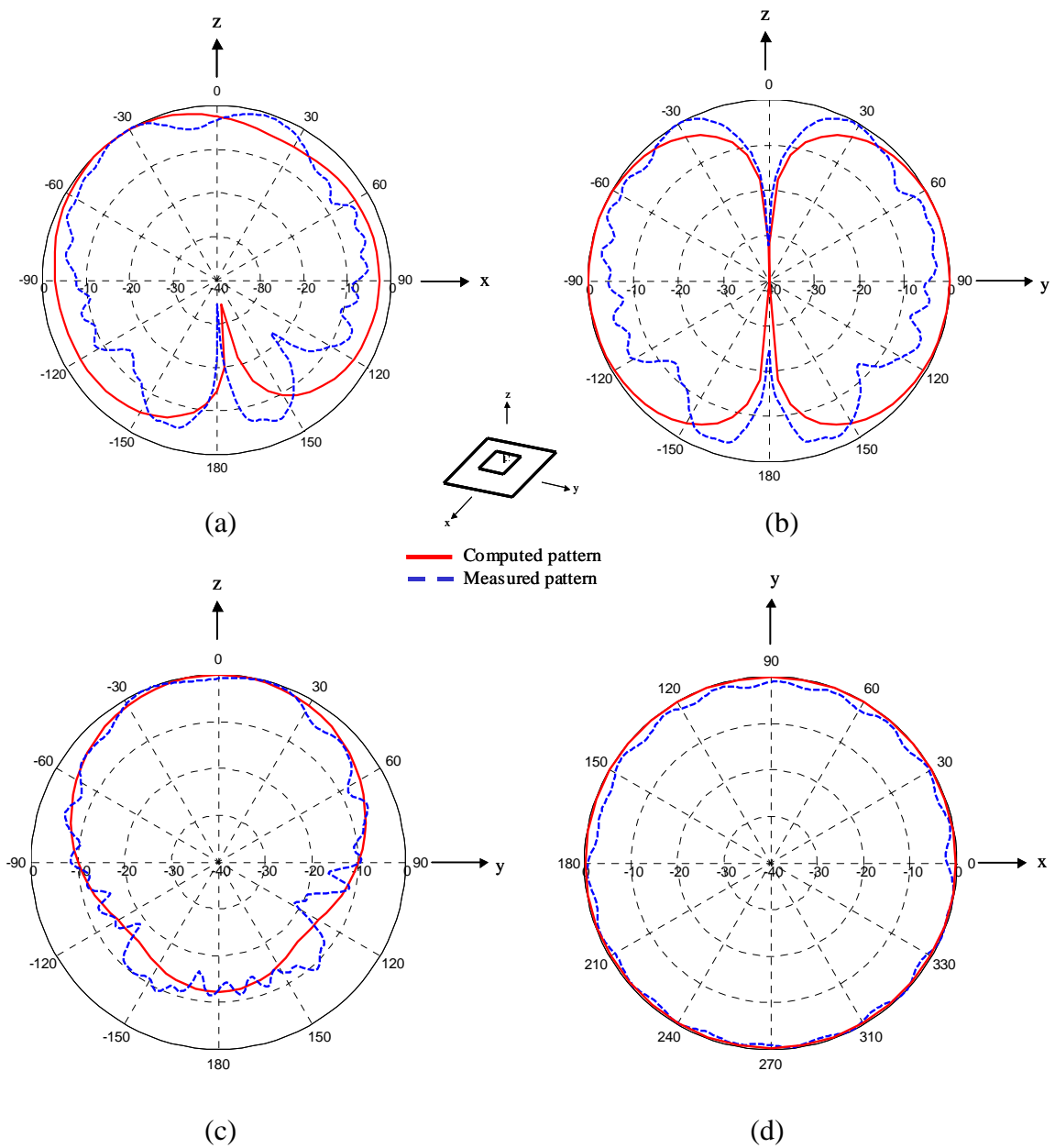


**Figure 5-10.** Computed (solid curve) and measured (dashed curve) normalized radiation patterns of the PIFA at 1943 MHz (from simulations) and 1890 MHz (from measurements) mounted on a square ground plane of size  $L = 80\text{mm}$  in the (a) elevation ( $\phi=0^\circ$ ) E-plane, (b) elevation ( $\phi=90^\circ$ ) E-plane, (c) elevation ( $\phi=90^\circ$ ) H-plane, and (d) azimuth ( $\theta=90^\circ$ ) E-plane. Refer to Fig. 5-4 for the structure geometry.

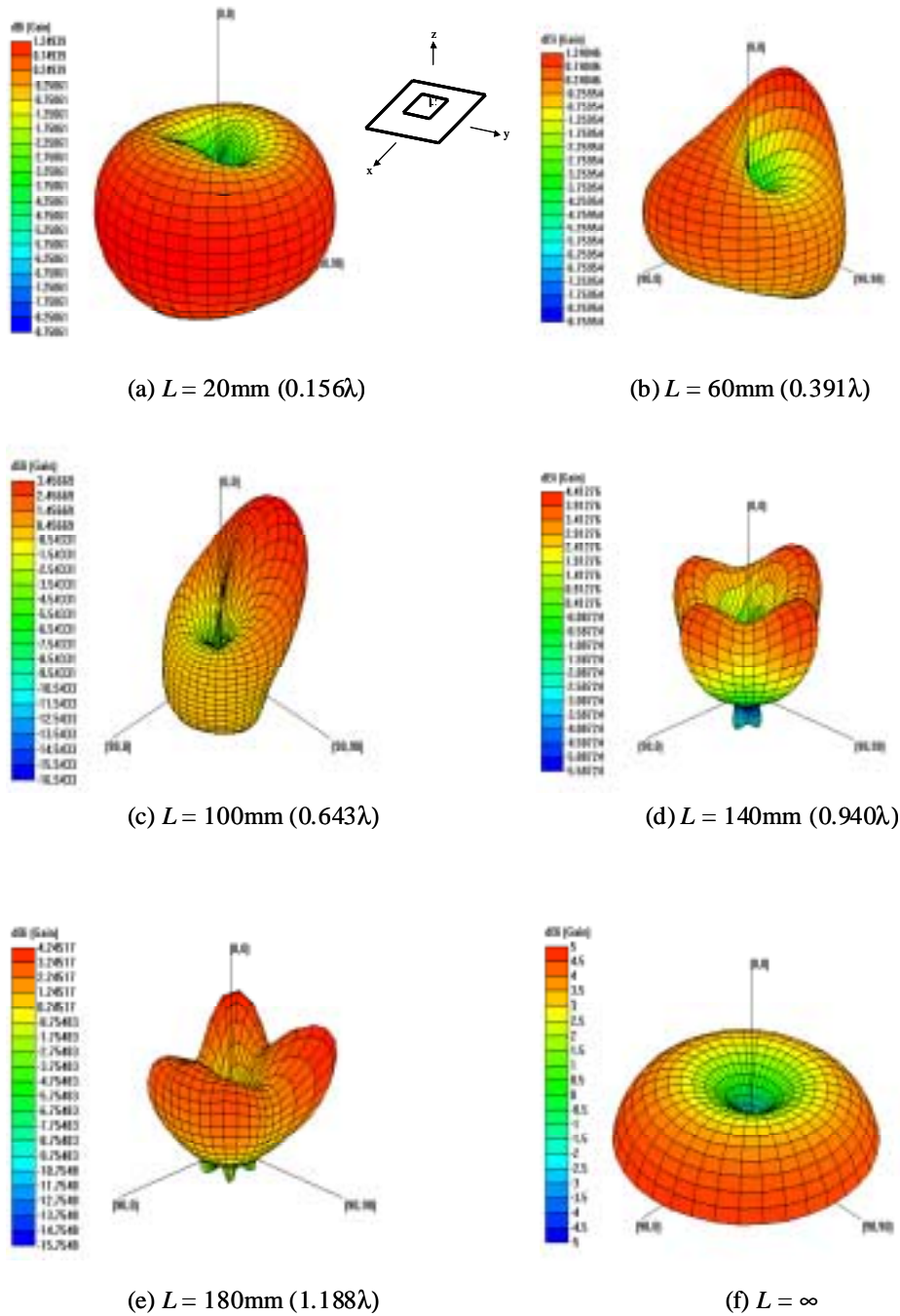


**Figure 5-11.**  $E_0$  radiation patterns of the PIFA at resonance (see Table 5-1 for resonant frequencies for each case) mounted on a square ground plane whose length is (a)  $L = 20\text{mm}$  ( $0.156\lambda$ ), (b)  $L = 60\text{mm}$  ( $0.391\lambda$ ), (c)  $L = 100\text{mm}$  ( $0.643\lambda$ ), (d)  $L = 140\text{mm}$  ( $0.940\lambda$ ), (e)  $L = 180\text{mm}$  ( $1.188\lambda$ ), (f)  $L = \infty$ . Refer to Fig. 5-4 for the structure geometry.

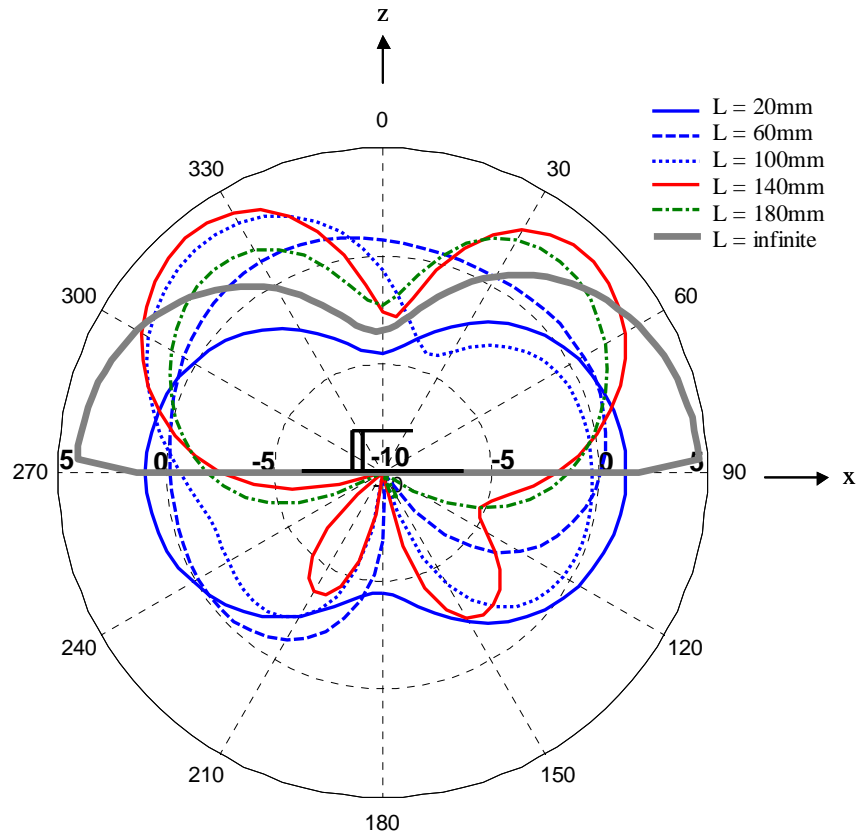


**Figure 5-12.** Computed  $E_\theta$  radiation patterns at resonance (see Table 5-1 for resonant frequencies for each case) in the  $x$ - $z$  elevation plane ( $\phi=0^\circ$ ) for ground plane size is  $L = 20\text{mm}$  ( $0.156\lambda$ ),  $L = 60\text{mm}$  ( $0.391\lambda$ ),  $L = 100\text{mm}$  ( $0.643\lambda$ ),  $L = 140\text{mm}$  ( $0.940\lambda$ ),  $L = 180\text{mm}$  ( $1.188\lambda$ ), and  $L = \infty$ . Refer to Fig. 5-4 for the structure geometry.

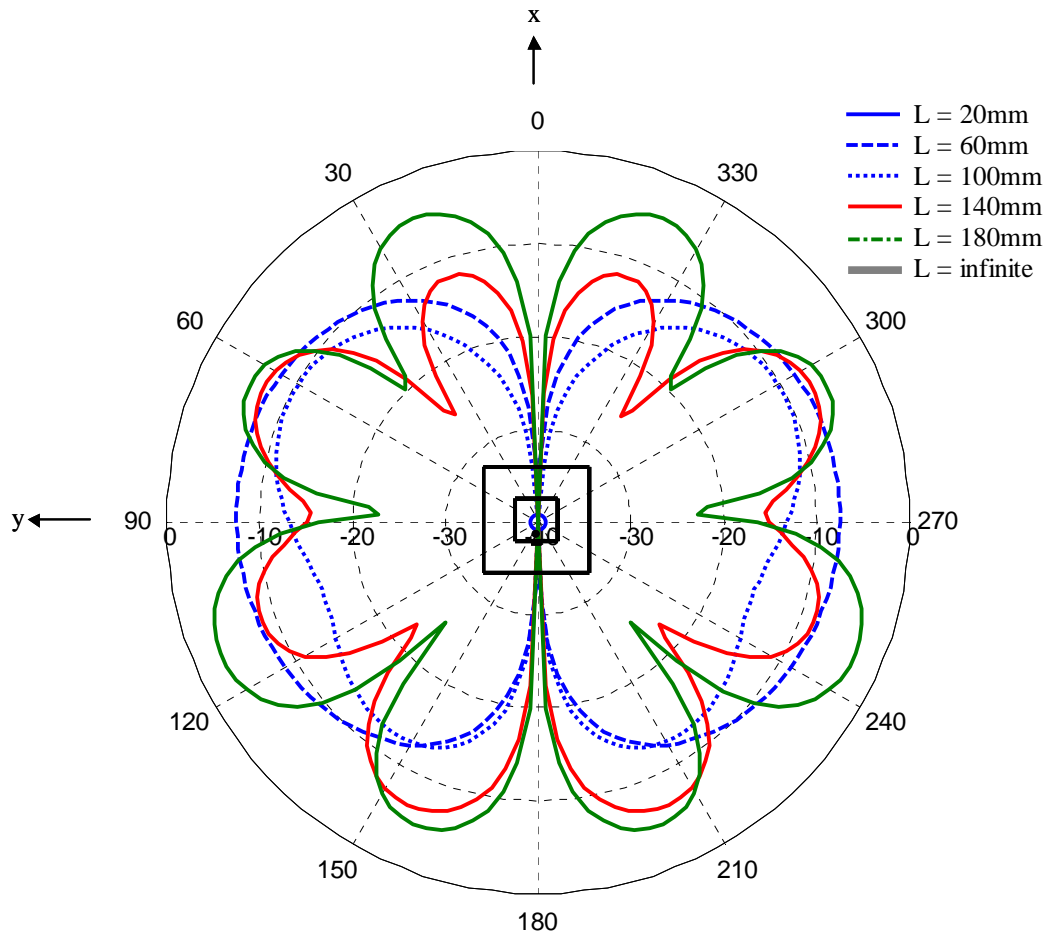


**Figure 5-13.** Computed  $E_\theta$  radiation patterns at resonance (see Table 5-1 for resonant frequencies for each case) in the x-y azimuth plane ( $\theta=90^\circ$ ) for ground plane size is  $L = 20\text{mm}$  ( $0.156\lambda$ ),  $L = 60\text{mm}$  ( $0.391\lambda$ ),  $L = 100\text{mm}$  ( $0.643\lambda$ ),  $L = 140\text{mm}$  ( $0.940\lambda$ ),  $L = 180\text{mm}$  ( $1.188\lambda$ ), and  $L = \infty$ . Refer to Fig. 5-4 for the structure geometry.

### 5.3.3. Other Configurations

The previous section discussed a PIFA mounted on a square ground plane. Two other configurations were modeled for the case when the ground plane is not square. Figure 5-14 shows the two rectangular ground plane cases:  $W = L/2$  and  $W = 2L$ .

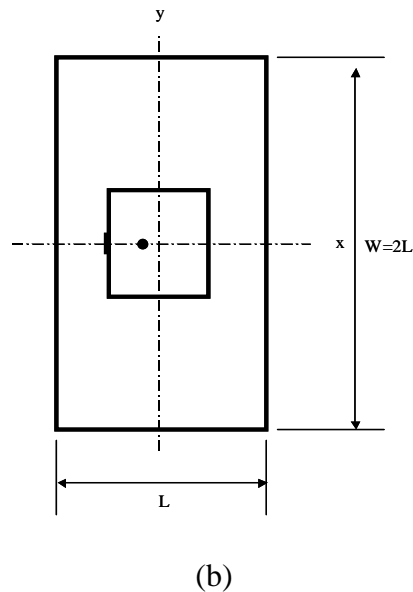
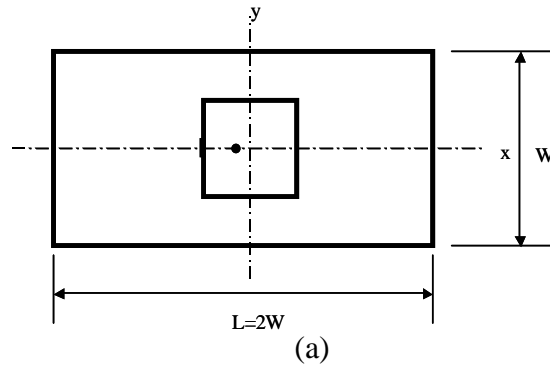


**Figure 5-14.** Configurations of the structure for rectangular ground plane: (a)  $W=L/2$  and (b)  $W=2L$ . The other geometric parameter values remain the same as in Fig. 5-4.

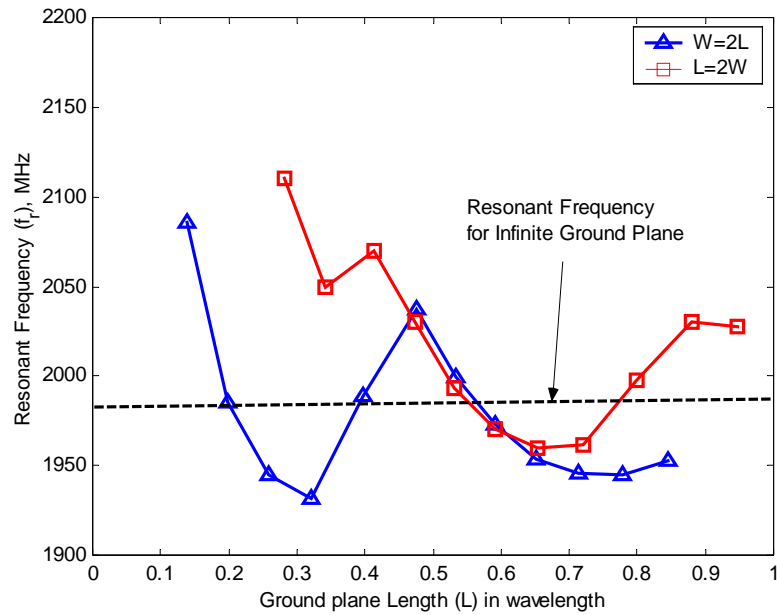


**Figure 5-15.** Resonant frequency of a conventional PIFA mounted on various rectangular ground plane sizes computed using IE3D. Refer to Fig. 5-14 for the structure geometry.

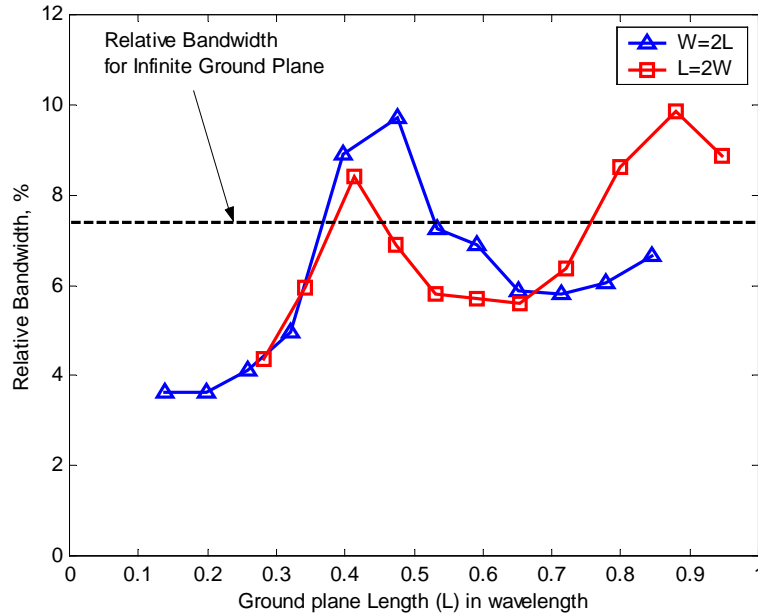


**Figure 5-16.** Relative bandwidth of a conventional PIFA mounted on various rectangular ground plane sizes computed using IE3D. Refer to Fig. 5-14 for the structure geometry.

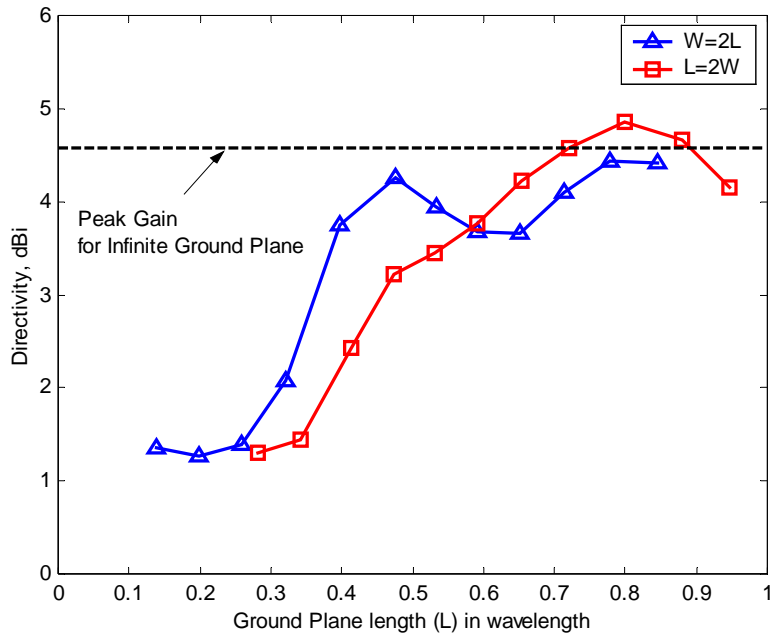


**Figure 5-17.** Peak gain of a conventional PIFA mounted on various rectangular ground plane sizes of the two configurations computed using IE3D. Refer to Fig. 5-14 for the structure geometry.

Characteristics of the two antenna configurations are plotted in Figs. 5-15, 5-16, and 5-17. They show behavior similar to that for the previously discussed square ground plane. The resonant frequency, bandwidth and gain of the antenna fluctuate around the characteristics values of the antenna mounted on infinite ground plane. Deviation from the values for the infinite ground plane size can be significant. The resonant frequency varies from 1930 MHz to 2100 MHz for a ground plane going from size as small as the upper plate of the PIFA to  $1 \lambda$ , as shown in Fig. 5-15. More importantly, the relative bandwidth and gain fluctuate significantly. Fig. 5-16 shows that the PIFA has a relative bandwidth of 3.6% for a ground plane size equal to that of the upper plate and increases to a first maximum value of about 9% that exceeds the infinite ground plane bandwidth at about  $L=0.45\lambda$ , then oscillates as the ground plane size increases. For the case of rectangular ground plane of  $L=2W$ , the bandwidth reaches another maximum at  $L=0.85\lambda$ .

Figure 5-18 illustrates radiation patterns for a few ground plane sizes in the x-z plane where maximum directivity occurs. The pattern behavior is similar to that of a PIFA on a square ground plane shown in Fig. 5-12.

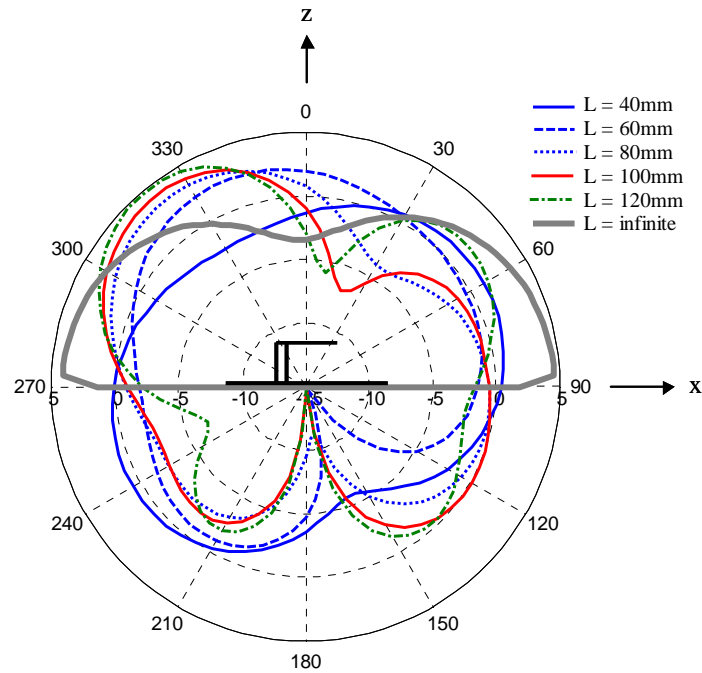


**Figure 5-18.** Computed  $E_0$  radiation patterns at resonance (see Table 5-1 for resonant frequencies for each case) in the x-z elevation plane ( $\phi=0^\circ$ ) for ground plane size is  $L = 40\text{mm}$  ( $0.156\lambda$ ),  $L = 60\text{mm}$  ( $0.391\lambda$ ),  $L = 80\text{mm}$  ( $0.643\lambda$ ),  $L = 100\text{mm}$  ( $0.940\lambda$ ),  $L = 120\text{mm}$  ( $1.188\lambda$ ), and  $L = \infty$ . Refer to Fig. 5-14a for the structure geometry.

The influence of ground plane size on directivity was also investigated. As shown in Fig. 5-17, the gain is about 3.5 dB lower than that for the infinite ground plane when the ground plane is very small, i.e.  $L \leq 0.2\lambda$ . Directivity increases as the ground plane size increases and reaches a maximum at  $L=0.8\lambda$ . Notice that the peak gain at that ground plane size is a bit above that of a PIFA on an infinite ground plane. Intuitively, one would expect that the gain of an antenna mounted on an infinite ground plane would be larger than that of an antenna on a finite ground plane because all the power is radiated above

the infinite ground plane. When the ground plane becomes finite, radiation appears below the ground plane and the directivity decreases. However, ground plane edge effects become significant for relatively small ground plane and can produce a radiation pattern that has a larger directivity in one direction, even though back radiation still exists.

The influence of ground plane size and shape on resonant frequency, bandwidth, and gain were investigated for rectangular ground plane sizes smaller than one wavelength. For a fixed PIFA size, one can select optimum characteristics or vary its resonant frequency by adjusting the size of the ground plane. For optimum performance, the rectangular ground plane should have a length  $L$  of about  $0.45\lambda$  for the case when the short-circuit plate of the PIFA is oriented parallel to the longer edge of the ground plane ( $W=2L$ ), and a length  $L$  of about  $0.85\lambda$  when the short-circuit plate is oriented parallel to the shorter edge of the ground plane ( $L=2W$ ). These sizes give large bandwidth and directivity for the same resonant frequency, about 2035 MHz. Similar characteristics were also seen in the case of a square ground plane, shown in Figs. 5-7, 5-8, and 5-9.

#### **5.4. Effects of Position and Orientation of a PIFA on a Finite Ground Plane**

The previous section discussed the effects of the ground plane size on the PIFA performance. Computations and measurements were performed for PIFAs mounted at the center of the ground plane. This section reports on investigations into the characteristics of PIFAs mounted at different locations on a ground plane and with different orientations. This investigation provides guidelines for designing a PIFA with a fixed-size ground plane for optimal performance.

### 5.4.1. PIFA Geometries

Two configurations were examined: the short-circuit plate parallel to the shorter edge of a rectangular ground plane and parallel to the longer edge, as shown in Fig. 5-19. The dimensions of the PIFA are the same as in Fig. 5-4 with the rectangular ground plane of fixed size with  $L=100$  mm and  $W=50$  mm. For each position and orientation of the antenna mounted on the ground plane, the probe-feed location ( $p_x$  or  $p_y$ ) is adjusted so that the antenna is matched to  $50 \Omega$  at resonance. Resonant frequency, impedance bandwidth, and gain are then computed using the IE3D simulation code.

### 5.4.2. Numerical Results

The configuration in Fig. 5-19a, where the short-circuit plate is parallel to the shorter edge of the ground plane, is evaluated first. As shown in this figure, the position of the PIFA is determined by the center of the shorting plate relative to the bottom left corner of the ground plane, denoted by  $C(c_x, c_y)$ . The feed location relative to the center of the shorting plate,  $C$ , is  $(p_x, p_y)$ . Computations were performed only for locations covering one-half of the ground plane because the structure is symmetric about  $y = 25$  mm. Results for the other half are obtained by symmetry. The location of the PIFA is such that none of its edges extend beyond the edges of the ground plane. Therefore,  $c_y$  can vary from 25 mm to 40 mm and  $c_x$  can vary from 0 mm to 80 mm. Performance values computed using IE3D are presented in Table 5-2. The data are also plotted in Figs. 5-20, 5-21, and 5-22 for resonant frequency, relative bandwidth, and gain, respectively, versus the position of the PIFA on the ground plane. Notice that the data for the PIFA at  $c_y = 40$  mm are not computed because the antenna cannot be matched exactly to  $50 \Omega$  at resonance at that position. Therefore, computations for these positions are omitted for consistency with other data.

Figures 5-20 to 5-22 show clearly where the PIFA can be mounted for best performance. Without changing the size of the whole structure, one can improve the characteristics of the antenna by moving its position on the ground plane. The highest

relative bandwidth and the highest directive gain at resonant frequency of 2380 MHz is obtained when the PIFA is positioned at the longer edge of the ground plane with its short-circuit plate in the proximity of the ground plane shorter edge. From the design standpoint, this is the best placement for optimal performance at that frequency.

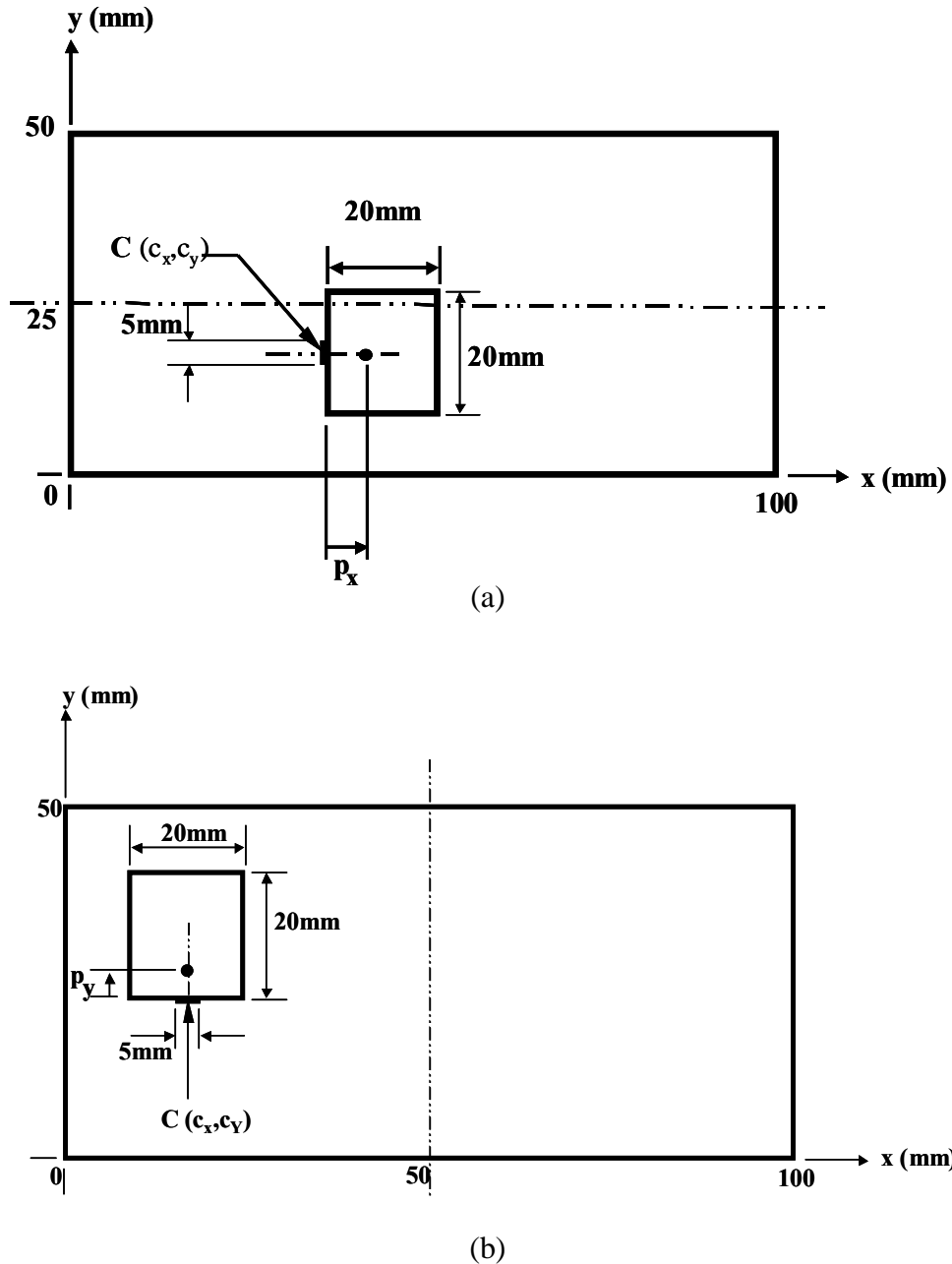


**Figure 5-19.** Geometries of the PIFA antenna configurations mounted on a  $L=100\text{mm}$  by  $W=50\text{mm}$  ground plane with the short-circuit plate oriented parallel to (a) the shorter edge and (b) the longer edge of the ground plane.

**Table 5-2**  
 Computed Data for Configuration in Fig. 5-19a Where the Short-Circuit Plate is Positioned Parallel to the Shorter Edge of the Ground Plane.

PIFA Position Cy(mm)	PIFA Position Cx (mm)	Probe Location from strap Px (mm)	Resonant frequency (MHz)	Bandwidth (MHz)	Bandwidth (%)	Gain (dBi)
35	0	5.3	2110	270	12.80	4.73
30	0	3.4	2020	175	8.66	4.73
25	0	3	1990	150	7.54	4.68
35	4	6	2220	305	13.74	4.44
30	4	3.3	2070	174	8.41	4.31
25	4	2.9	2050	151	7.37	4.25
35	8	8	2380	375	15.76	3.92
30	8	3.2	2070	167	8.07	3.69
25	8	2.8	2050	145	7.07	3.47
35	11	6	2255	288	12.77	3.35
30	11	3.1	2065	160	7.75	3.16
25	11	2.7	2045	140	6.85	2.71
35	14	4.5	2160	234	10.83	3.25
30	14	3	2060	155	7.52	2.90
25	14	2.7	2045	140	6.85	2.19
35	20	4	2115	210	9.93	3.30
30	20	3	2055	155	7.54	3.12
25	20	2.6	2030	135	6.65	2.95
35	30	3.8	2070	190	9.18	3.90
30	30	2.9	2015	140	6.95	4.01
25	30	2.6	2000	125	6.25	4.06
35	35	3.7	2045	182	8.90	4.01
30	35	2.8	1995	135	6.77	4.14
25	35	2.6	1985	124	6.25	4.20
35	45	3.2	1985	146	7.36	3.60
30	45	2.5	1955	113	5.78	3.75
25	45	2.3	1946	101	5.19	3.80
35	55	2.7	1970	127	6.45	2.56
30	55	2.1	1940	93	4.79	2.44
25	55	2	1935	85	4.39	2.40
35	65	2.4	1988	116	5.84	1.70
30	65	1.9	1964	85	4.33	1.77
25	65	1.8	1960	78	3.98	1.84
35	80	3.2	2200	200	9.09	2.54
30	80	2.7	2120	148	6.98	2.63
25	80	2.3	2100	131	6.24	2.39

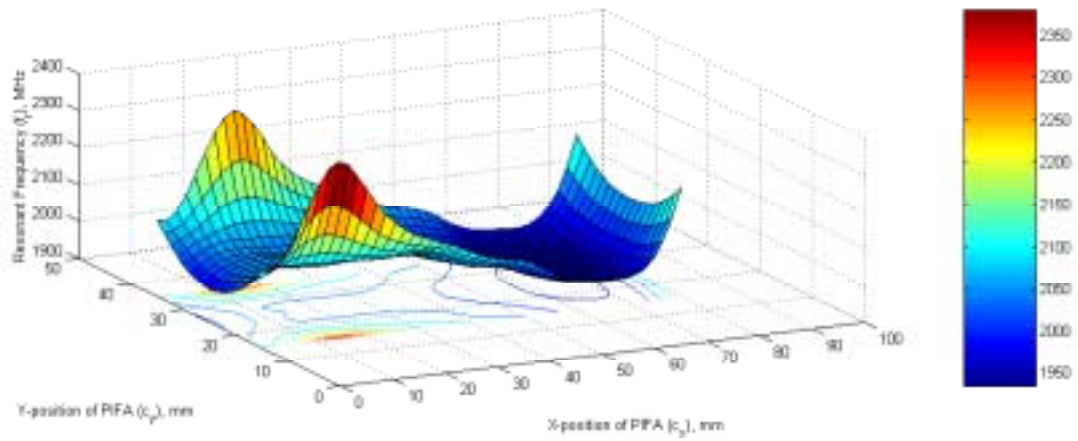


**Figure 5-20.** Computed resonant frequency versus location of the PIFA on the ground plane for the configuration shown in Fig. 5-19a where the short-circuit plate is parallel to the shorter edge of the ground plane.

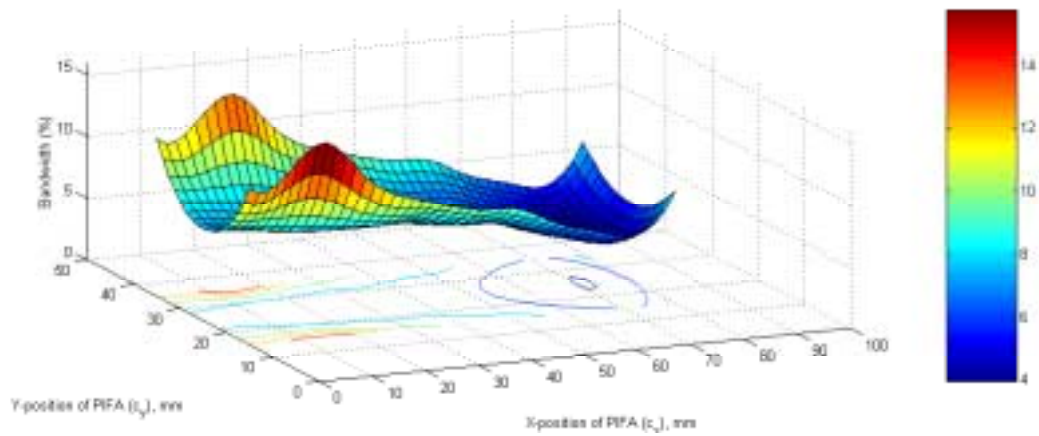


**Figure 5-21.** Computed relative bandwidth versus location of the PIFA on the ground plane for the configuration shown in Fig. 5-19a where the short-circuit plate is parallel to the shorter edge of the ground plane.

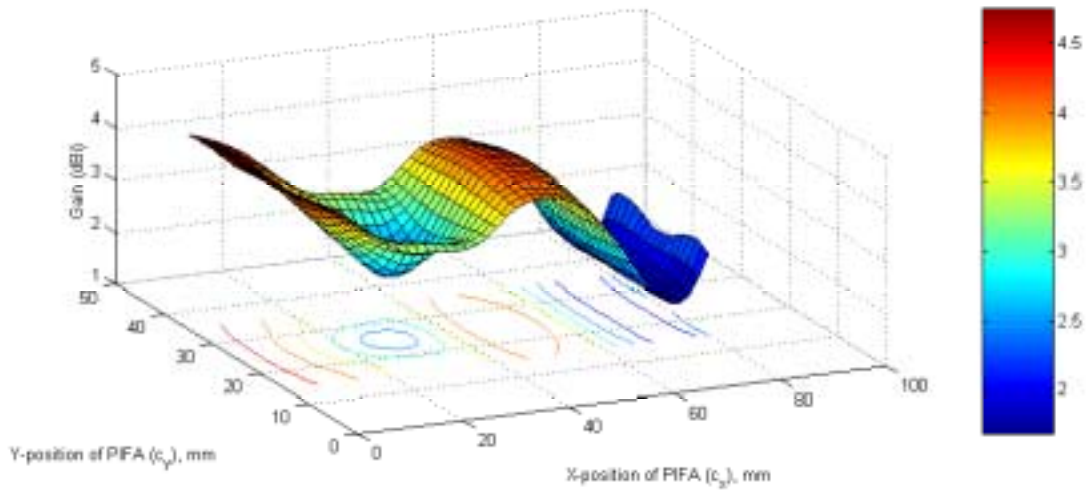


**Figure 5-22.** Computed directive gain versus location of the PIFA on the ground plane for the configuration shown in Fig. 5-19a where the short-circuit plate is parallel to the shorter edge of the ground plane.

On the other hand, designing for the lowest resonant frequency for this configuration does not give good performance, as illustrated in Fig. 5-23. For the lowest frequency of this configuration ( $c_x = 55$  mm and  $c_y = 25$  mm), the structure has a low gain and bandwidth. This demonstrates that there is tradeoff among the performance parameters and that optimal design depends on the specifications of the antenna.

The structure configuration with the short-circuit plate parallel to the longer edge as shown in Fig. 5-19b was also evaluated. Similar to the previous configuration, resonant frequency, relative bandwidth, and gain were obtained from the IE3D moment method simulator. Figures 5-24 to 5-26 illustrate the plots of frequency, bandwidth, and directive gain, respectively, versus the PIFA position on the ground plane. Again, computations were not performed for PIFA positions at  $c_x = 10$  mm because the antenna could not be matched to  $50 \Omega$  at resonance.

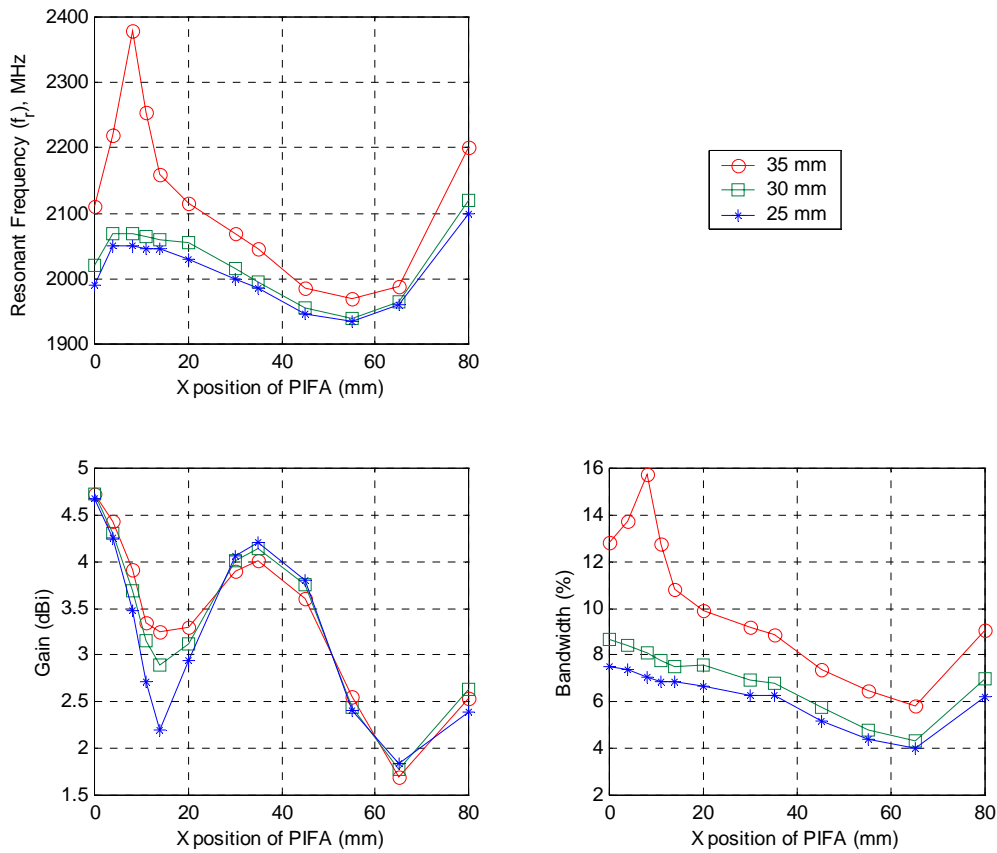


**Figure 5-23.** Resonant frequency, relative bandwidth, and directive gain of a PIFA on a ground plane for the configuration shown in Fig. 5-19a, where the short-circuit plate is parallel to the shorter edge of the ground plane, versus positions  $C_x$  of PIFA along  $C_y=25, 30,$  and  $35$  mm. Computed values were obtained using IE3D.

Figures 5-24 to 5-26 indicate that the PIFA should be placed close to the corner of the ground plane where the short-circuit plate is at the ground plane edge,  $c_x=20$  mm and  $c_y=0$  mm, for optimal gain and bandwidth performance. Figure 5-27 shows the characteristics of the same PIFA versus its position  $C_y$  for  $C_x = 20, 30, 40, 50$ mm. Comparing the results of the two orientation configurations, as shown in Figures 5-23 and 5-27, the PIFA with the short-circuit plate parallel to the shorter edge of the rectangular ground plane is preferred for obtaining higher directive gain. In fact, the maximum gain that one can get from this configuration is about 4.75 dBi while the largest gain possible with configuration of 5-19a is 3.5 dBi.

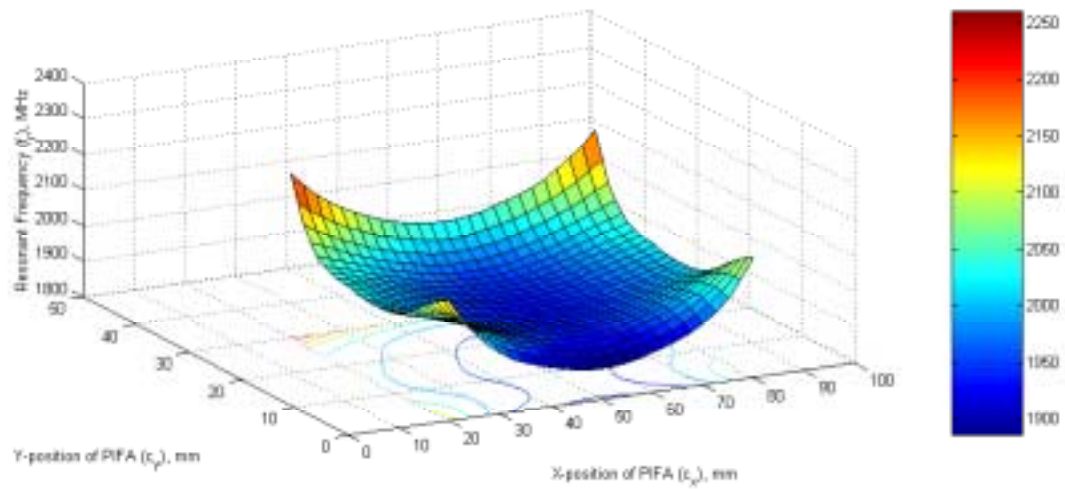


**Figure 5-24.** Computed resonant frequency versus location of the PIFA on the ground plane for the configuration shown in Fig. 5-19b where the short-circuit plate is parallel to the longer edge of the ground plane. Computed values were obtained using IE3D.

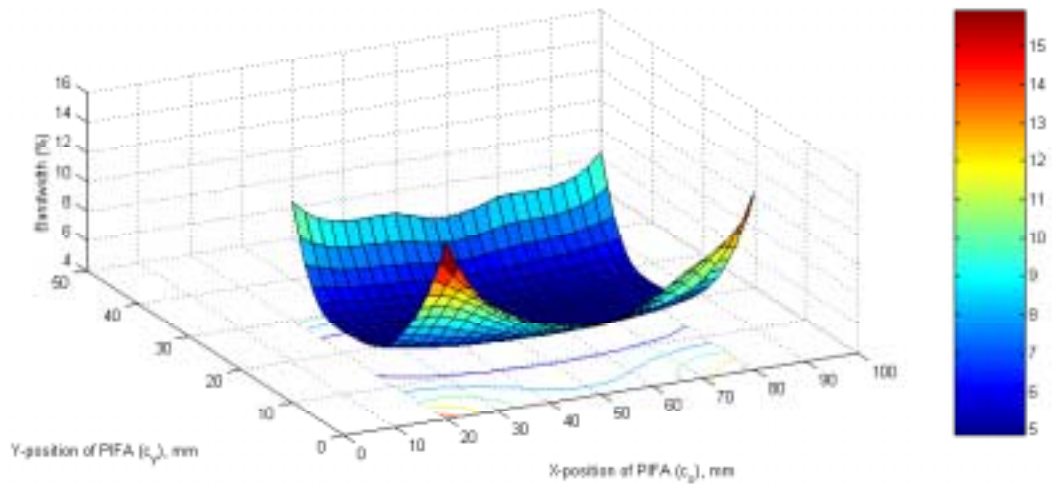


**Figure 5-25.** Computed relative bandwidth versus location of the PIFA on the ground plane for the configuration shown in Fig. 5-19b where the short-circuit plate is parallel to the longer edge of the ground plane. Computed values were obtained using IE3D.

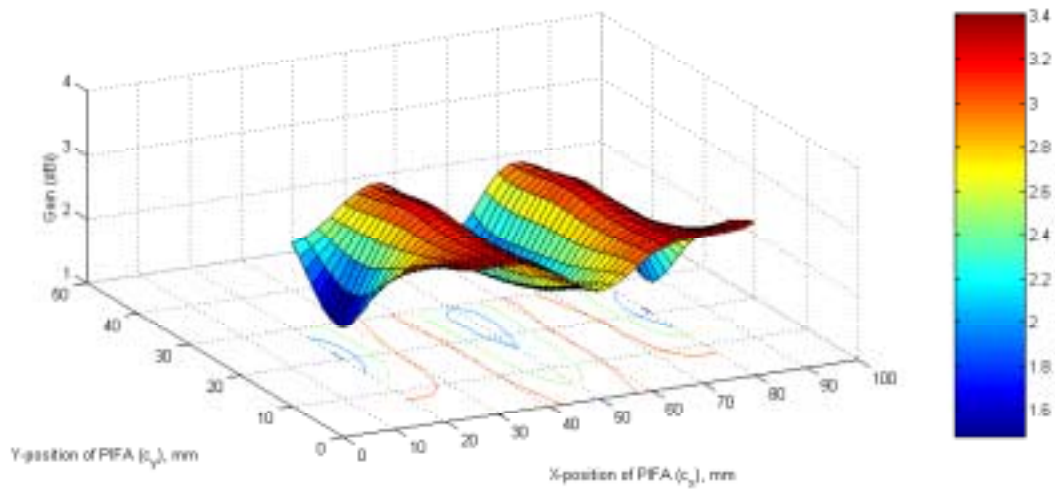


**Figure 5-26.** Computed directive gain versus location of the PIFA on the ground plane for the configuration shown in Fig. 5-19b where the short-circuit plate is parallel to the longer edge of the ground plane. Computed values were obtained using IE3D.

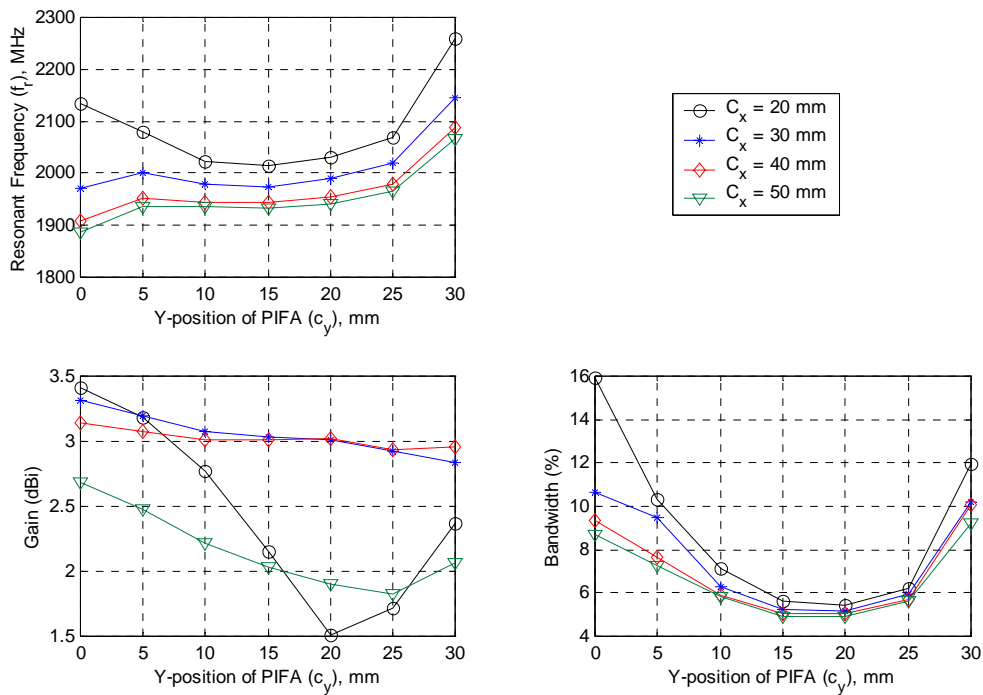


**Figure 5-27.** Resonant frequency, relative bandwidth, and directive gain of a PIFA on a ground plane for the configuration shown in Fig. 5-19b, where the short-circuit plate is parallel to the shorter edge of the ground plane, versus positions  $C_y$  of PIFA along  $C_x = 20, 30, 40,$  and  $50$  mm. Computed values were obtained using IE3D.

## 5.5. Summary

This chapter reviewed approaches used to simulate antennas on finite ground planes. Among them, the method of moments and geometrical theory of diffraction (GTD) are widely used to model antennas. Computed and experimental results for a monopole mounted on a circular ground plane were presented to show that these modeling techniques give good results.

The method of moments is then used to model the PIFA mounted on a finite ground plane. Extensive simulations using IE3D and measurements were performed to investigate the characteristics of this antenna for different ground plane sizes and shapes. Results obtained were compared to experimental measurements done in Virginia Tech antenna laboratories and showed very good agreement. The influence of the ground plane on the PIFA are summarized as follows:

- There is no significant impact of ground plane size and shape on the resonant frequency of the antenna, except for the square ground plane case when its size  $L < 0.2\lambda$
- Bandwidth is low (less than 8%) for  $L < 0.8\lambda$  (square ground plane) and for  $L < 0.4\lambda$  (rectangular ground plane)
- Gain is low for a ground plane size  $L < 0.4\lambda$
- There is a significant influence of the ground plane size on the antenna radiation patterns
- Finite ground plane size introduces high cross-polarization along the horizon.

Position and orientation of a PIFA on a fixed-size ground plane were studied as well. The key of these investigations is to help design a PIFA mounted on a ground plane of size equal or less than a wavelength with optimal performance. It was found that the PIFA should be placed close to the corner of the ground plane where the short-circuit

plate is at the ground plane edge,  $c_x=20$  mm and  $c_y=0$  mm, for optimal gain and bandwidth performance.

## 5.6. References

- [1] J. Huang, "The Finite Ground Plane Effect on the Microstrip Antenna Radiation Patterns," *IEEE Trans. Ant. Prop.*, vol. AP-31, no. 4, July 1983, pp. 649-655.
- [2] A.K. Bhattacharyya, "Effects of Ground plane and Dielectric Truncations on the efficiency of a Printed Structure," *IEEE Trans. Ant. Prop.*, vol. AP-39, no. 3, March 1991, pp. 303-308.
- [3] P. Moosavi and L. Shafai, "Directivity of Microstrip Ring Antennas and Effects of Finite Ground Plane on Radiation Parameters," *Ant. Prop. Soc. Int. Symp.*, vol. 2, 1998, pp. 672-675.
- [4] K. Hirisawa and M. Haneishi, *Analysis, Design, and Measurement of small and Low-Profile Antennas*, Artech House, Boston: 1992.
- [5] A.S. Meier and W.P. Summers, "Measured Impedance of Vertical Antennas and Effects of Finite Ground Planes," *Proc. IEEE*, vol. 37, June 1969, pp.609-616.
- [6] G.A. Thiele and T.H Newhouse, "A hybrid Technique for Combining Moment Method with the Geometrical Theory of Diffraction," *IEEE Trans. Ant. Prop.*, vol. AP-23, no. 6, June 1975, pp. 62-69.
- [7] K.H. Awadalla, T.S.M. Maclean, "Input Impedance of a Monopole Antenna at the Center of a Finite Ground Plane," *IEEE Trans. Ant. Prop.*, vol. AP-26, March 1978, pp. 244-248.
- [8] G.A. Thiele and G.K. Chan, "Application of the Hybrid Technique to the Time Domain Problems," *IEEE Trans. Ant. Prop.*, vol. AP-26, Jan. 1978, pp. 151-155.
- [9] M.M. Weiner, "Monopole Element at the Center of a Circular Ground Plane whose Radius is Comparable to a Wavelength," *IEEE Trans. Ant. Prop.*, vol. AP-35, no. 5, May 1987, pp. 488-495.
- [10] J.H. Richmond, "Monopole Antenna on Circular Disk," *IEEE Trans. Ant. Prop.*, vol. AP-32, no. 12, Dec. 1984, pp. 1282-1287.
- [11] IE3D User's Manual, Zeland Software Inc., Release 5, 2000.

# Chapter 6: A Wideband Compact PIFA

## 6.1. Introduction

In recent years, rapid expansion of the wireless communication industry has created a need for multi frequency band operation portable devices to meet the ever-increasing subscriber demand. Dual-band antennas have been realized in the past, but the great concern about these antennas is that some are designed using dual feed, which introduces some difficulties in the feed design. Other dual-band designs cover frequencies that are far apart, such as AMPS and PCS operating bands. The proposed antenna offers wide bandwidth covering frequency bands that are close together using a single non-contacting feed, in a small, low cost, and easy to manufacture.

The previous chapters covered the following topics: the types of antennas that are good candidates for low-profile structures; techniques for widening the bandwidth; and ground plane effects on the antenna performance. These topics will be used to design the proposed antenna, the wideband compact PIFA (WC-PIFA). The WC-PIFA characteristics will be evaluated using IE3D simulations and the measured data. Performance inside a box and in the proximity of a human hand will also be investigated. These results will then be used later to improve the antenna to combat the coupling effects of the hand.

## 6.2. Geometry of the WC-PIFA

The geometry of the proposed antenna is shown in Fig. 6-1. It is based on the conventional PIFA antenna but uses a capacitive feed instead of the conventional

conducting probe feed. This non-contacting feed is constructed by terminating the inner conductor of a SMA connector to a conducting plate parallel to the upper radiating plate. A small shorting plate is placed from the center of the left edge of the radiating plate to the center of the left edge of the ground plane, as shown in Fig. 6-1. The radiating plate, feed plate, and ground plane have the same width. The small conducting plate parallel to and located below the feed plate serves as the ground plane of the antenna. The new feature of this design is its small ground plane which is part of the whole antenna structure. It does not require any other conducting plane, such as a metal case, to perform properly. The basic mechanism behind this simple antenna structure relies on two closely spaced resonant frequencies to form a wider impedance bandwidth, as discussed in chapter 3.

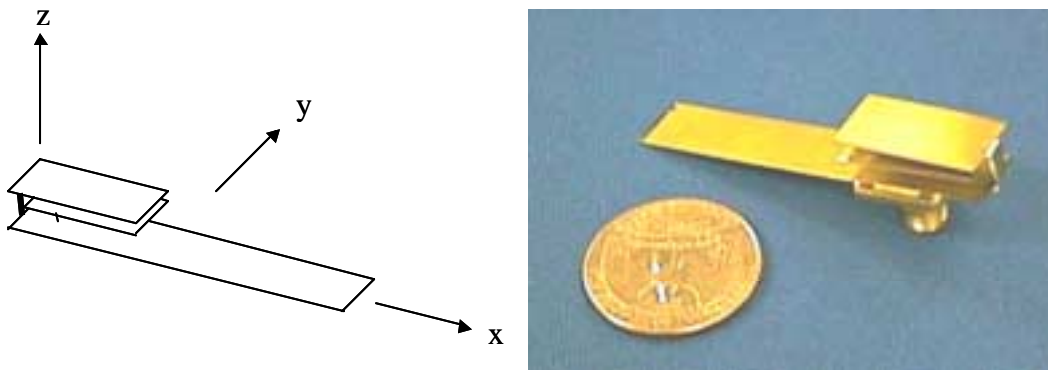
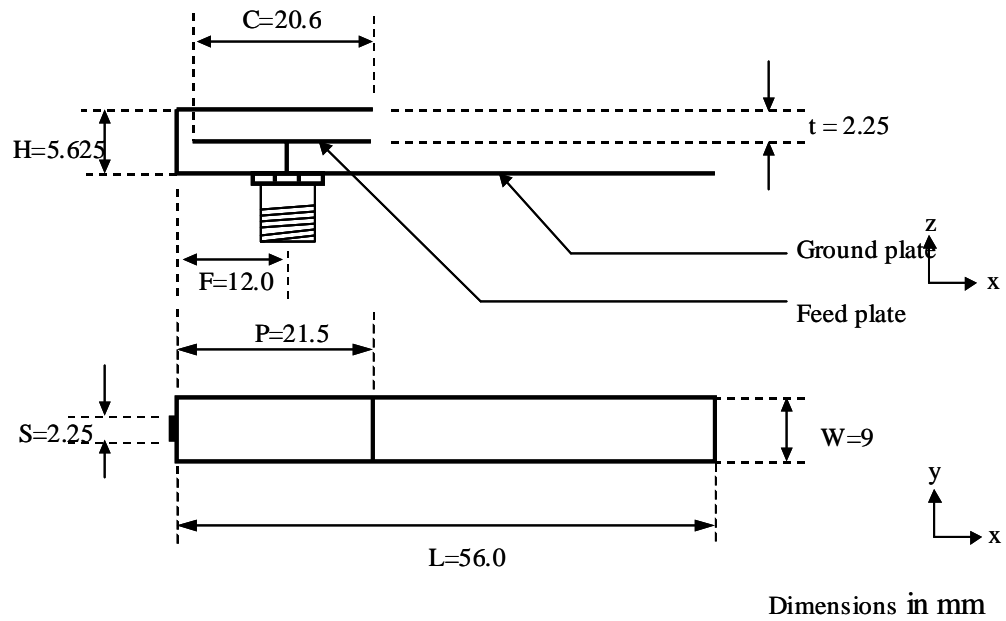


**Figure 6-1.** Geometry of the wideband compact PIFA designed for a center frequency of 2.2 GHz.

### **6.3. Numerical and Experimental Results**

Figure 6-2 shows the impedance characteristics and VSWR of the WC-PIFA. The antenna exhibits a bandwidth of 790 MHz, from 1.78 GHz to 2.57 GHz, or 36.3 % bandwidth at a center frequency of 2.175 GHz. The bandwidth and impedance matching of the WC-PIFA are mainly controlled by the width of the shorting plate, the distance between the upper and middle plate of the structure, and the location of the probe feeding the middle plate. Figures 6-3 and 6-4 show the current distribution of the WC-PIFA antenna and its far-field radiation patterns, respectively. These figures indicate that the main radiating element of the antenna is the ground plate where most of the current is flowing.

The antenna was also fabricated with the dimensions shown in Fig. 6-1. The metal used is made of brass with a thickness of 0.016 in. (0.406 mm). It was then measured in various environments to investigate the antenna performance subjected to coupling effects. The antenna was first measured in free-space environment. Impedance measurements were performed using HP8720C network analyzer. Figure 6-5 shows the measured VSWR of the WC-PIFA along with the computed values. Good agreement between predicted and measured results was obtained. This proves that the structure modeled in IE3D accurately predicts the performance of the antenna.

Next, investigations of the antenna detuning due the coupling effects of a handset and a hand were performed. The goal is to see how these effects degrade the antenna performance. Figure 6-7 shows the measured VSWR of the WC-PIFA embedded in a plastic box, made of Acrylonitrile Butadine Styrene (ABS), as shown in Fig. 6-6. The figure indicates that the antenna is suitable to be embedded in plastic cases of radio devices.

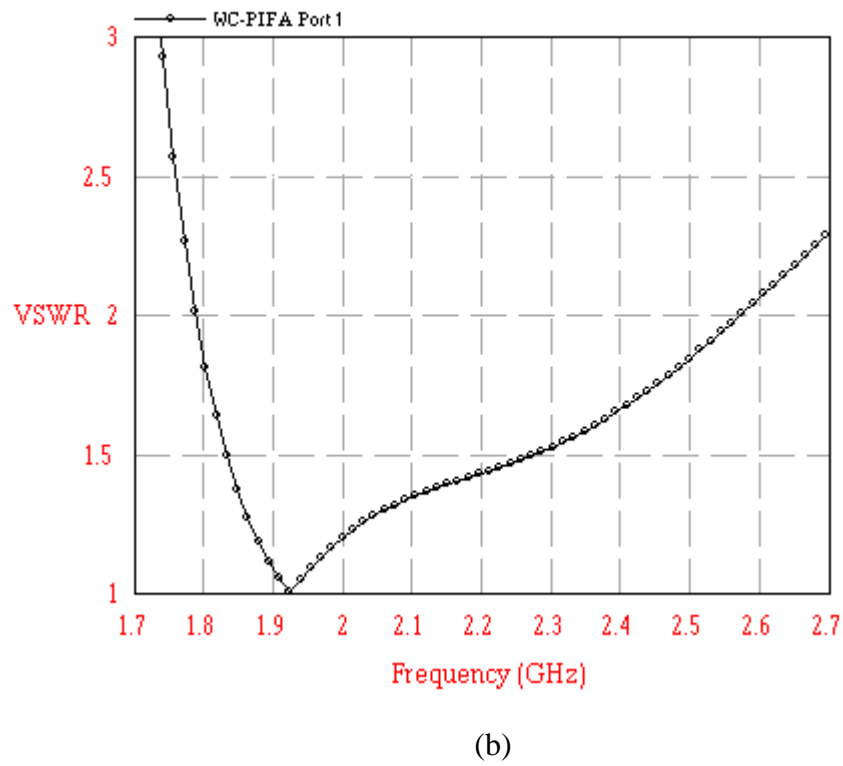
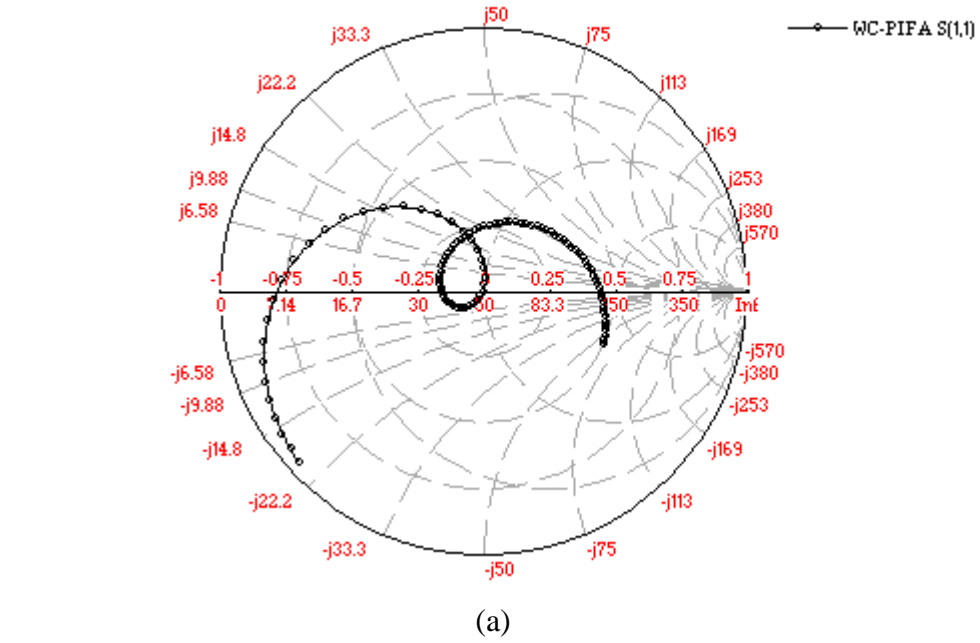


**Figure 6-2.** (a) Impedance Characteristics and (b) VSWR of the WC-PIFA in Fig. 6-1 computed using IE3D.

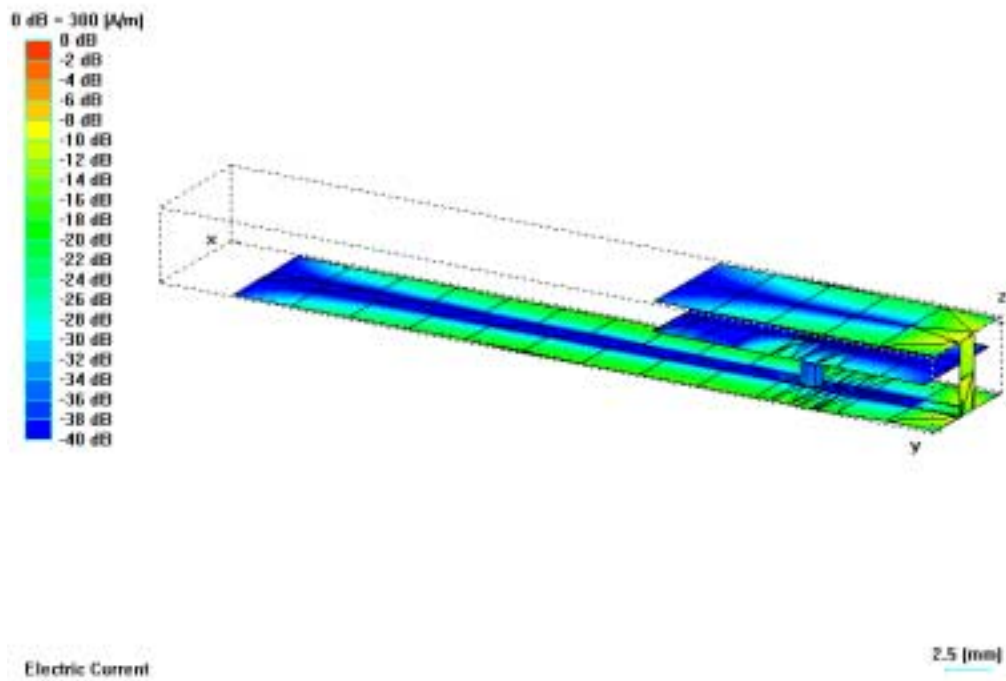
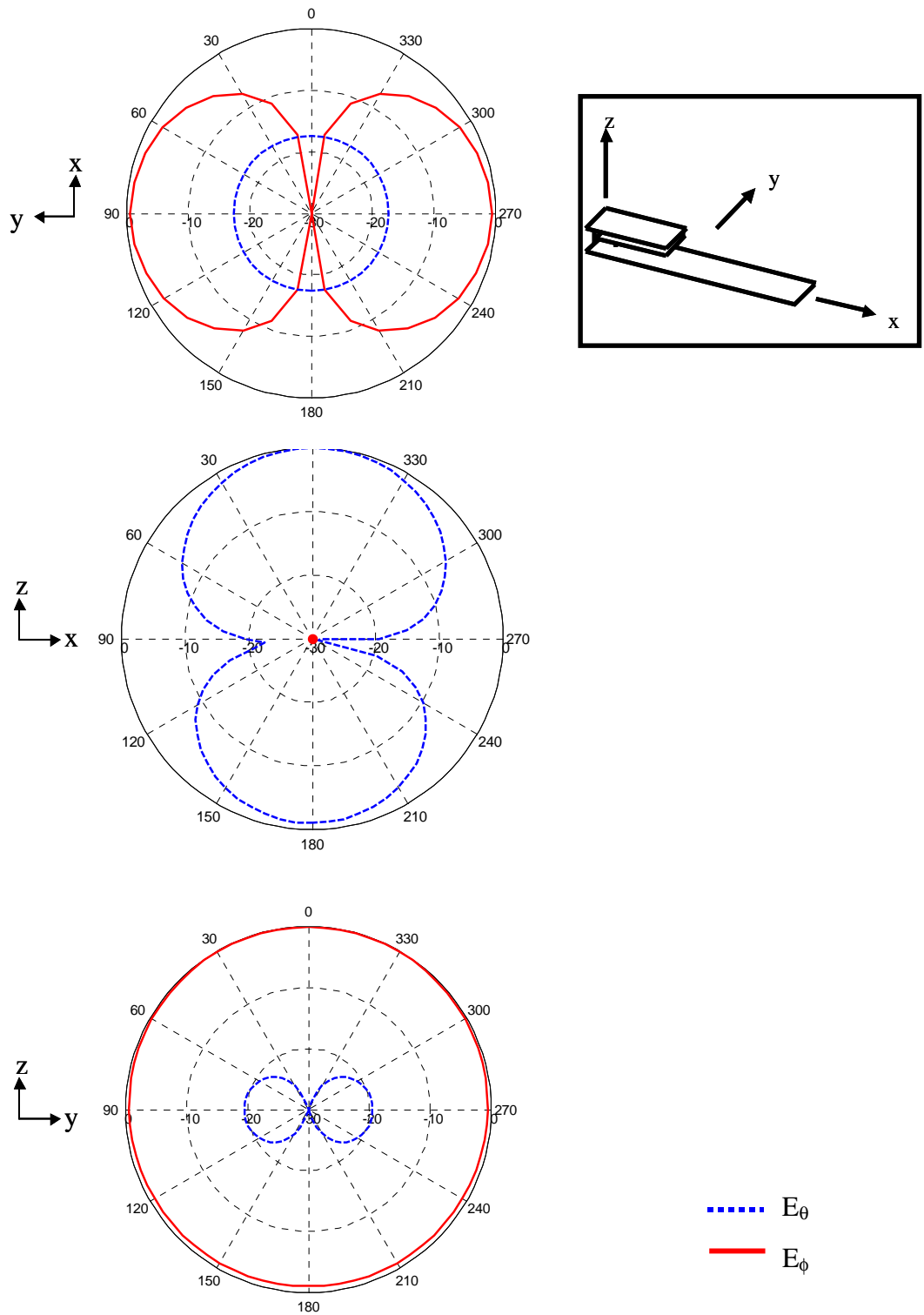
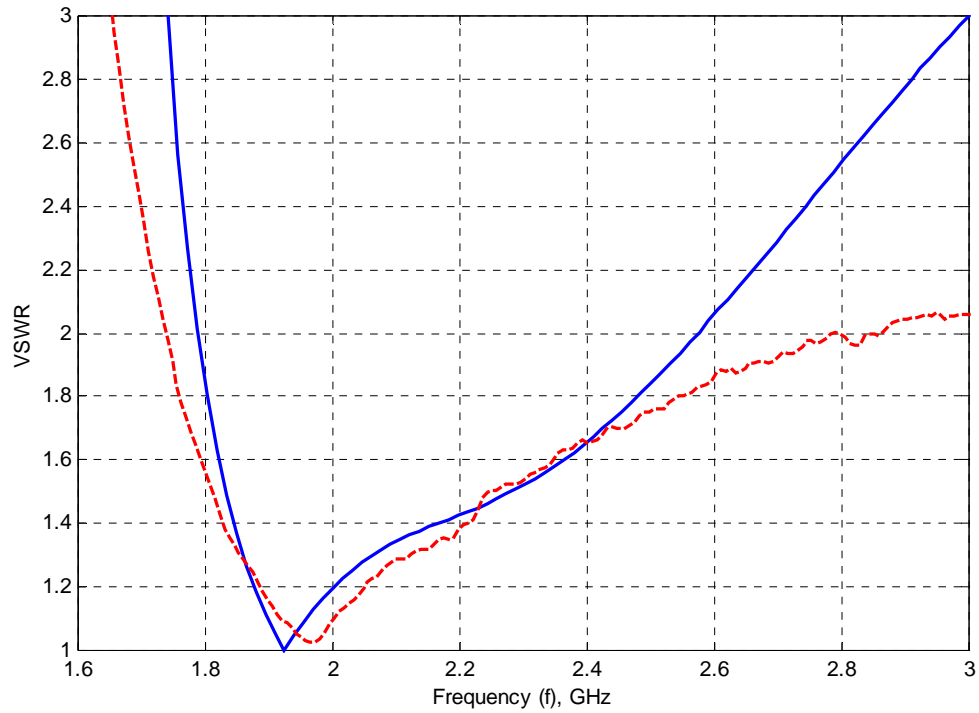


Figure 6-3. Current distribution of the WC-PIFA in Fig. 6-1 at the center Frequency 2.2 GHz computed using IE3D.



**Figure 6-4.** Normalized far-field radiation patterns of the structure of Fig. 6-1 at 2.2 GHz computed using IE3D.



**Figure 6-5.** Computed (solid curve) and measured (dashed curve) VSWR of the WC-PIFA in Fig. 6-1. Numerical values were computed using IE3D.

The plastic case does not significantly affect the antenna impedance. Although there is a shift in resonant frequency and the higher end of the frequency band has an increase in the VSWR, this level of VSWR is still acceptable. At the 2.4-GHz ISM band, the VSWR is about 2.1:1. Therefore, the WC-PIFA can be used as internal antennas at the ISM band with good performance since a 2:1 VSWR is usually considered suitable for handheld devices.

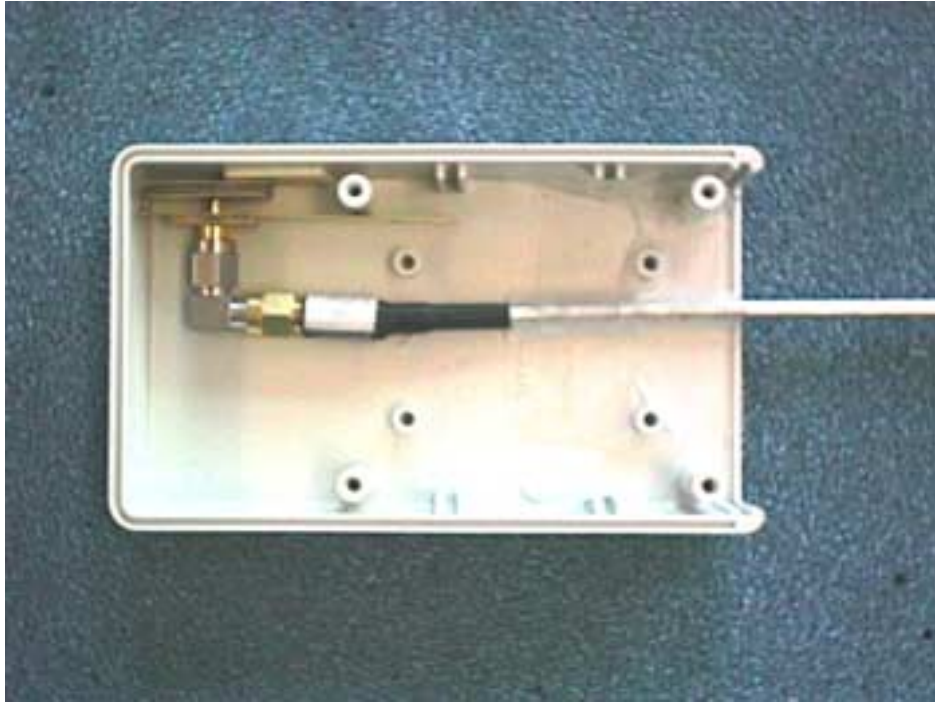


**Figure 6-6.** Measurement configuration of the WC-PIFA embedded in plastic case.

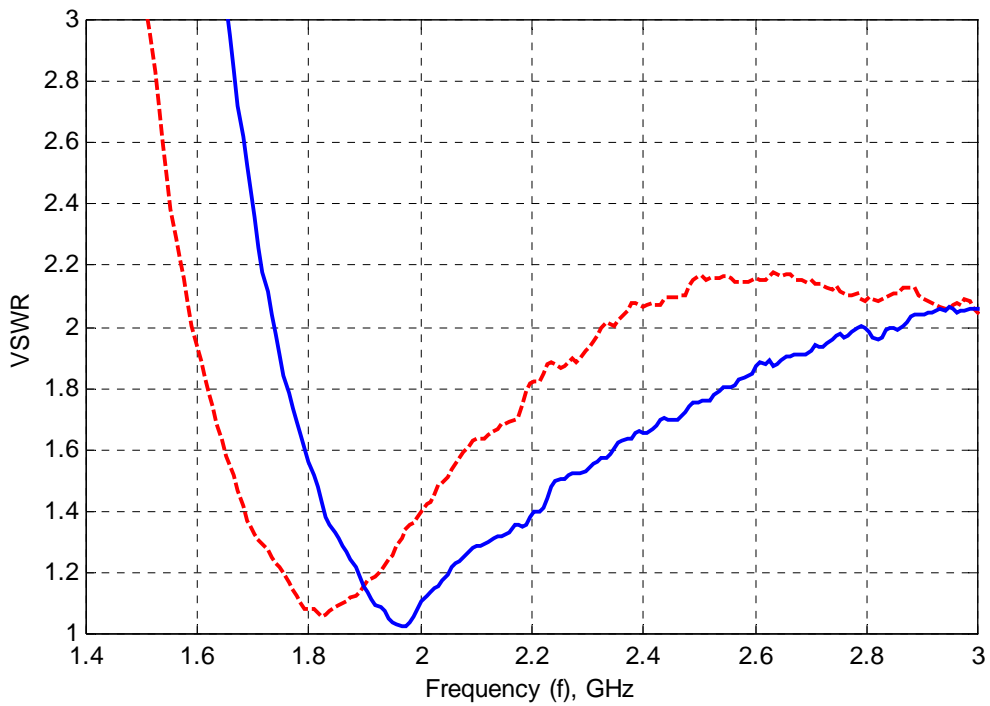


**Figure 6-7.** Measured VSWR (dashed curve) of the WC-PIFA embedded in plastic case shown in Fig. 6-6, along with measured VSWR in free-space (solid curve).

For hand-held devices such as cellphones and palm pilot, coupling effects with human body play an important factor in detuning antennas embedded in such devices. Impedance measurements were performed for the WC-PIFA embedded in plastic case in the proximity of a hand, as illustrated in Fig. 6-8. Figure 6-9 depicts this detuning effect due to the hand. The antenna impedance mismatch level is higher at the lower end of the frequency band. Hand coupling, however, does not affect the higher end of the band, as shown in Fig. 6-9. The VSWR is more than 2:1 at the frequency below 2 GHz.

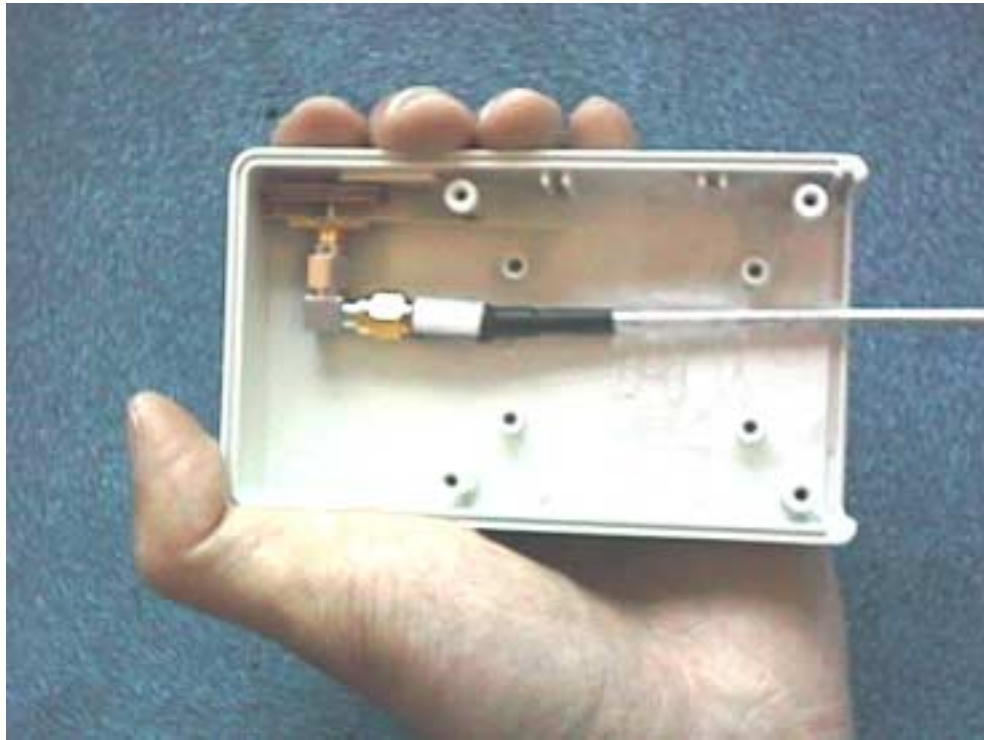


**Figure 6-8.** Measurement Configuration of the WC-PIFA embedded in a plastic cover in the proximity of a hand.

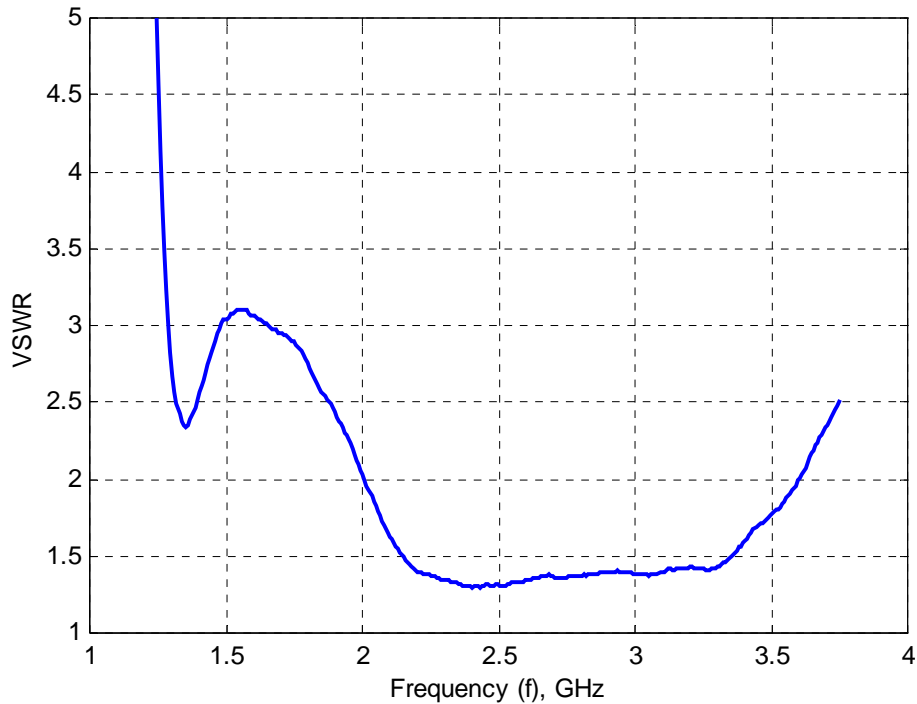


**Figure 6-9.** Measured VSWR of the WC-PIFA embedded in a plastic cover in the proximity of a hand shown in Fig. 6-8.

Preliminary work on how to combat WC-PIFA performance degradation due to hand coupling lead us to insert of a piece of dielectric material of 2.33 dielectric constant between the upper plate and the middle plate, as illustrated in Fig. 6-10. The new WC-PIFA impedance is measured in free-space environment and in proximity of a hand as previously. Dielectric loading improves impedance bandwidth, as depicted in Fig. 6-11b. Hand coupling effects lower the VSWR, increasing impedance bandwidth. The frequency band for a VSWR of 2:1 ranges from 1.38 GHz to 3.3 GHz. The VSWR of the loaded WC-PIFA in free-space environment is a bit higher than that without the substrate in frequency band of interest. It is nonetheless tolerable.

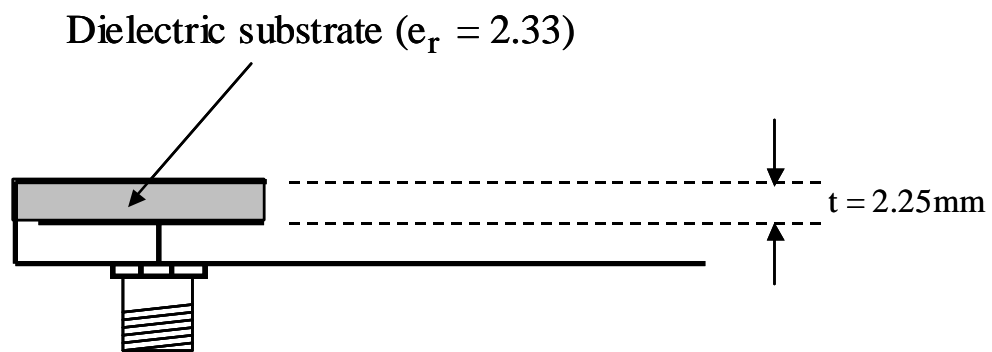
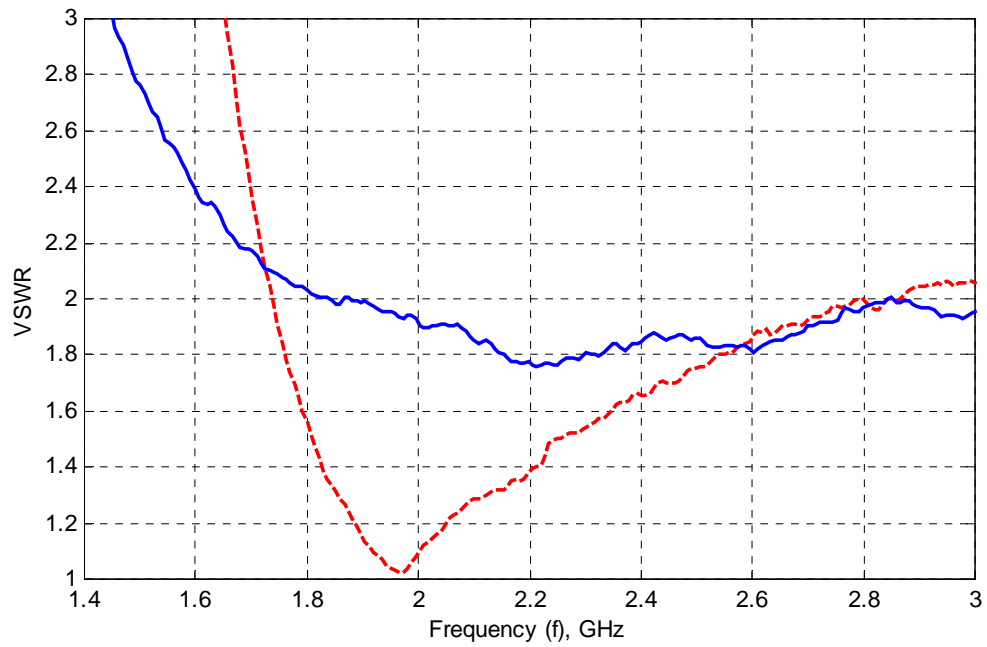
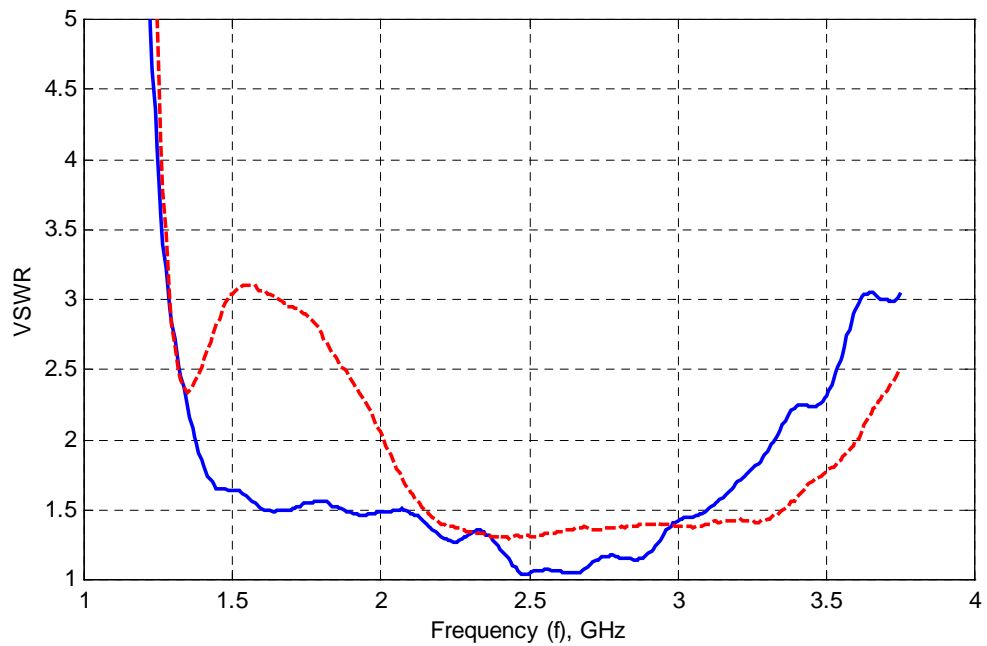


**Figure 6-10.** Configuration of the WC-PIFA with a dielectric layer inserted between the upper plate and the middle plate to combat the hand detuning effects.



(a)



(b)

**Figure 6-11.** Measured VSWR of the WC-PIFA with dielectric loading (solid curve) and without dielectric substrate (dashed curve) in (a) free-space and (b) embedded in a plastic cover in the proximity of a hand.

Chapter 4 discussed the fundamental limit on antenna size and bandwidth. It is interesting to see where the WC-PIFA is located on the fundamental limit curve. Figure 6-12 illustrates the comparison between various antennas found in the literature and the WC-PIFA; see Table 6-1. As depicted in the plot, the WC-PIFA point lies on the 100% efficiency curve. This means that the antenna reaches the fundamental limit of realizable antennas without any loss in efficiency. Compared with the other antennas shown in the figure, the WC-PIFA is the best antenna in terms of its size-bandwidth performance.

An important point should be made relative to calculation of antenna size – or radius of the sphere enclosing the antenna. The sphere radius  $a$  should enclose the antenna and its image if the antenna is on a large ground plane. However, since the size of the wideband PIFA ground plane is small, the structure of the antenna, including its ground plane, is contained in the sphere. Thus, the entire volume of the wideband PIFA is included in the enclosing volume, whereas the conventional PIFA volume excludes its large ground plane.

**Table 6-1**

Characteristics of the four antennas presented in this paper.

<b>Antenna</b>	<b>Feed</b>	<b>Ground Plane Size</b>	<b>Volume (wavelength)</b>	<b>Bandwidth (%)</b>
Patch [1]	Capacitive	Large	$63.52 \times 10^{-4} \lambda^3$	32
Conventional PIFA [2]	Probe	Large	$6.21 \times 10^{-4} \lambda^3$	5
Capacitively loaded PIFA [3]	Capacitive	Large	$3.430 \times 10^{-4} \lambda^3$	10
WC-PIFA	Capacitive	Small ( $0.4 \lambda$ )	$4.492 \times 10^{-4} \lambda^3$ (without ground plane) $11.23 \times 10^{-4} \lambda^3$ (with ground plane)	36.3

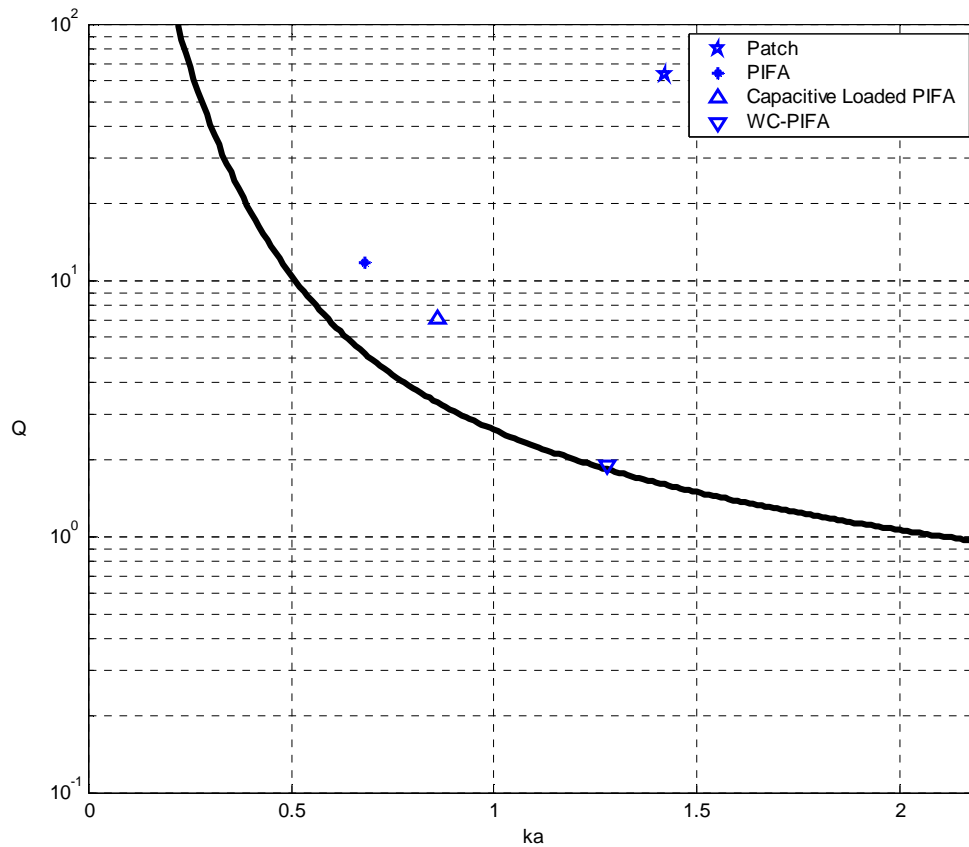


**Figure 6-12.** Fundamental limit curve together with the points corresponding to the WC-PIFA and several other antennas found in the literature.

## 6.4. Summary

This chapter introduced a novel antenna having a very wide bandwidth covering several useful frequency bands such as DCS-1800, PCS-1800/1900, IMT-2000, ISM,

WLAN. The WC-PIFA was modeled in IE3D and results were comparable to the measurements. The antenna was tested under various environment to see how well it performed. Preliminary results showed that the antenna can be embedded in plastic cases without any significant degradation in impedance matching. However, in the proximity of a hand, the performance degrades. This detuning effect due to the hand can be however suppressed by inserting a dielectric layer between the upper plate and the middle plate of the antenna. In terms of antenna size-bandwidth, the WC-PIFA is the best compared to some other small antenna because it reaches the fundamental limit of realizable antennas without any loss in efficiency.

## 6.5. References

- [1] W.L. Stutzman and G.A. Thiele, *Antenna Theory and Design*, 2<sup>nd</sup>, John Wiley, New-York: 1988.
- [2] K. Hirisawa and M. Haneishi, *Analysis, Design, and Measurement of small and Low-Profile Antennas*, Artech House, Boston: 1992.
- [3] C.R. Rowell and R.D. Murch, "A Capacitively Loaded PIFA for Compact Mobile Telephone Handsets," *IEEE Trans. Ant. Prop.*, vol. AP-45, no. 5, May 1997, pp.837-841.

# **Chapter 7: Conclusions and Recommendations**

## **7.1. Conclusions**

The purpose of this discussion was to present design issues for sized-reduced and low-profile antennas in a hand-held environment. Potential candidates for small and low-profile structures, such as microstrip antennas (MSA) and planar inverted-F antennas (PIFA), were presented in chapter 2. Theoretical models on these antennas were investigated and a design procedure was presented for each of them. Techniques for widening the antenna impedance bandwidth were discussed in chapter 3. Two widely used techniques found in the literature are the edge-coupling technique and the capacitive feed technique. Chapter 4 reviewed the fundamental limit on antenna size and bandwidth. It gives the size limit of an antenna for a given bandwidth. The fundamental limits may be used as a guide for creating antenna specifications so that a search for unrealistic antenna can be avoided. An important effect in small handheld devices is the ground plane effects, as discussed in chapter 5. Antennas on finite ground planes do not behave the same as identical antennas on an infinite ground plane because the ground plane starts to radiate as it becomes small compared to the antenna. Investigations of a PIFA on finite ground planes of various sizes and shapes were performed in chapter 5. Finally, chapter 6 presented some preliminary investigations on a new small, low-profile, and low-cost antenna that has a very wide bandwidth. The wideband compact PIFA (WC-PIFA) can be used in wireless devices that require multiple frequency bands ranging from 1.75 GHz to 2.56 GHz such as DCS-1800, PCS, IMT-2000, ISM, and Bluetooth.

## **7.2. Recommendations**

The discussion on the new wideband compact antenna, the WC-PIFA, was brief. It was intended to present preliminary work on this antenna. Further study on its

characteristics should be performed. The analytical aspect of the WC-PIFA should be investigated in order to understand its basic mechanism. Coupling due to the proximity of a human body is an important issue for antennas in handheld radio devices and should be investigated as well. These studies will help improve the WC-PIFA performance and robustness.

## Vita

Minh-Chau T. Huynh was born in Saigon, Vietnam, and grew up in Liège, Belgium. As being grown up in a multicultural milieu, he learned and speaks fluently four languages: Vietnamese, French, English, and Spanish. In 1993 Minh-Chau began studying electrical engineering at Virginia Tech with a focus in wireless communications. He completed his Bachelor's degree in 1997 and pursued his study in graduate school. He joined the Virginia Tech Antenna Group as a graduate research assistant. There he worked on small-embedded antennas for wireless mobile applications for Galtronics USA, Inc. and in 1999, he developed a new wideband compact antenna. Currently, Minh-Chau is pursuing his PhD's degree at Virginia Tech.